

Thermo-hydro-mechanical coupled material point method for modeling freezing and thawing of porous media

Jidu Yu¹  | Jidong Zhao^{1,2}  | Shiwei Zhao¹  | Weijian Liang³

¹Department of Civil and Environmental Engineering, Hong Kong University of Science and Technology, Hong Kong, China

²HKUST Shenzhen-Hong Kong Collaborative Innovation Research Institute, Shenzhen, China

³Department of Civil and Environmental Engineering, Hong Kong Polytechnic University, Hong Kong, China

Correspondence

Jidong Zhao, Department of Civil and Environmental Engineering, Hong Kong University of Science and Technology, Kowloon, Hong Kong, China.
Email: jzhao@ust.hk

Funding information

National Natural Science Foundation of China, Grant/Award Number: 11972030; Research Grants Council of Hong Kong, Grant/Award Numbers: #16207319, #16208720, #16211221, #16206322, F-HKUST601/19, #C7082-22G, #T22-606/23-R; Hetao Shenzhen-Hong Kong Science and Technology Innovation Cooperation Zone, Grant/Award Number: #HZQBKCZYB2020083

Abstract

Climate warming accelerates permafrost thawing, causing warming-driven disasters like ground collapse and retrogressive thaw slump (RTS). These phenomena, involving intricate multiphysics interactions, phase transitions, nonlinear mechanical responses, and fluid-like deformations, and pose increasing risks to geo-infrastructures in cold regions. This study develops a thermo-hydro-mechanical (THM) coupled single-point three-phase material point method (MPM) to simulate the time-dependent phase transition and large deformation behavior arising from the thawing or freezing of ice/water in porous media. The mathematical framework is established based on the multiphase mixture theory in which the ice phase is treated as a solid constituent playing the role of skeleton together with soil grains. The additional strength due to ice cementation is characterized via an ice saturation-dependent Mohr–Coulomb model. The coupled formulations are solved using a fractional-step-based semi-implicit integration algorithm, which can offer both satisfactory numerical stability and computational efficiency when dealing with nearly incompressible fluids and extremely low permeability conditions in frozen porous media. Two hydro-thermal coupling cases, that is, frozen inclusion thaw and Talik closure/opening, are first benchmarked to show the method can correctly simulate both conduction- and convection-dominated thermal regimes in frozen porous systems. The fully THM responses are further validated by simulating a 1D thaw consolidation and a 2D rock freezing example. Good agreements with experimental results are achieved, and the impact of hydro-thermal variations on the mechanical responses, including thaw settlement and frost heave, are successfully captured. Finally, the predictive capability of the multiphysics MPM framework in simulating thawing-triggered large deformation and failure is demonstrated by modeling an RTS and the settlement of a strip footing on thawing ground.

KEYWORDS

climate warming, freezing and thawing, frozen soil, large deformation, material point method, multiphysics modeling, phase transition, thermo-hydro-mechanical coupling

This is an open access article under the terms of the [Creative Commons Attribution-NonCommercial](https://creativecommons.org/licenses/by-nc/4.0/) License, which permits use, distribution and reproduction in any medium, provided the original work is properly cited and is not used for commercial purposes.

© 2024 The Author(s). *International Journal for Numerical and Analytical Methods in Geomechanics* published by John Wiley & Sons Ltd.

1 | INTRODUCTION

Permafrost and seasonally frozen ground, which underlay approximately half of the land surface in the Northern Hemisphere,¹ are experiencing abnormal freeze–thaw cycles and accelerated thawing due to global climate changes.^{2–4} As permafrost melts, large quantities of greenhouse gases are released into the atmosphere, further contributing to climate warming.^{5,6} The warming of ice-rich permafrost causes significant hydrogeomorphic changes, resulting in the formation of various thermokarst landscapes,^{2,7} including thermokarst lakes, thermal erosion gullies, retrogressive thaw slumps (RTSs), periglacial hillslope movements, and active layer detachments.^{8,9} The increased extent of warming-driven thermokarst landforms and landslides is already evident in some cold regions, for example, in northern Canada,^{10–12} Siberia,^{4,7,13} and Tsinghai–Tibet plateau,^{3,14,15} posing increasing risks to nearby civil infrastructure and communities.^{12,16,17}

Modeling the freeze–thaw phenomenon of porous media in cold regions is challenging, arising from the complexities inherent in such geomaterials that involve multiphysics interactions, phase transitions, nonlinear mechanical responses, and fluid-like failure patterns.^{13,18,19} In the theory of porous media and continuum mechanics, frozen soils are commonly modeled as a multiphase mixture composed of soil grains, crystal ices, and liquid water (and gas if present), with ice and liquid water able to transfer between each other when the thermal condition changes.²⁰ Although the occurrences of ice in porous media are diversified (e.g., pore-filling ice, cementation ice, concretion ice, ice lens, ice wedge, etc.),^{10,21,22} simplified frozen soil models for macroscale modeling usually consider the crystal ices within pores to be connected, homogeneous, and bear loads jointly with soil grains and liquid water following the effective stress principle.^{23–25} The thermodynamic equilibrium of pore ice and water within frozen soils is typically characterized by a Clausius–Clapeyron equation,^{26–28} whereas the ice variations under changing thermodynamic conditions are frequently described by a physically consistent or phenomenologically defined soil freezing characteristic curve (SFCC).^{23,27}

Various numerical approaches have been developed to simulate the freezing and thawing of porous media in cold regions.^{23,29–37} Most of these developments are based on finite difference method (FDM),^{29–31,34} finite volume method (FVM),^{32,36} and finite element method (FEM).^{23,24,33,37,38} However, if aiming to simulate the history-dependent thermo-hydro-mechanical (THM) behavior in porous media under freeze–thaw actions, the Lagrangian-based FEM is generally favored over the Eulerian-based FVM or FDM.³⁹ The simulation of relevant mechanical responses necessitates the development of a soil constitutive model applicable to not only completely frozen but also partially frozen and unfrozen soil. The commonly used frozen soil constitutive models are often adapted from conventional models that are initially developed for unfrozen soils, such as Mohr–Coulomb model,^{40,41} modified Cam–Clay model,²⁴ Barcelona Basic Model,^{23,38} among others.^{42,43} With these models, FEM can be utilized to simulate various engineering problems, ranging from the thawing-induced distress of foundations to the differential settlements in road pavements due to soil heaving and the distortion of the railroad in seasonally frost regions.^{23,24,44} Nonetheless, FEM is not without limitations. It may encounter mesh distortion issues when simulating scenarios involving substantial deformations, limiting its application in modeling thawing-induced landslides and long-distance mass movements.

In recent years, the material point method (MPM) has emerged as a popular tool for modeling multiphysics large deformation problems in porous media. Various MPM formulations and frameworks for fully or partially coupled THM problems have been developed with a wide range of applications.^{45–58} For instance, Pinyol et al.⁵⁹ developed an explicit THM-coupled MPM to investigate the thermal effect in fast landslides. Lei et al.⁵³ extended the explicit MPM to unsaturated porous media for simulating the climate-driven slope failure process involving temperature variation and rainfall infiltration. Though explicit integration is well-received because of its simplicity, it may be constrained by the small time step size and the weakly compressible fluid assumption.^{53,58} To address this issue, Kularathna et al.⁵⁴ proposed a semi-implicit two-phase MPM based on the fractional step method, in which the assumption of liquid compressibility is reduced and the constraint of permeability on time step size is eliminated. Yu et al.^{60,61} further considered a non-isothermal saturated porous media and extended the above framework for THM-coupled large deformation problems, which is demonstrated to achieve good numerical stability and computational efficiency. However, these works did not consider the ice phase and the phase transition between ice and water in porous systems. To further model the ice phase, Zhao et al.⁶² integrated thermo-mechanical coupled MPM with bond-contact DEM for multiscale modeling of freeze–thaw behavior in porous media, but without considering the hydro-thermal and hydro-mechanical coupling processes. Sun et al.¹⁹ designed a two-point multiphysics coupling MPM for modeling the frost heave in rock slope, but still using explicit integration and failing to consider the effect of phase transition in the mass balance equation and the convective heat transfer in the energy balance equation. Despite the significant advancements in multiphysics MPM so

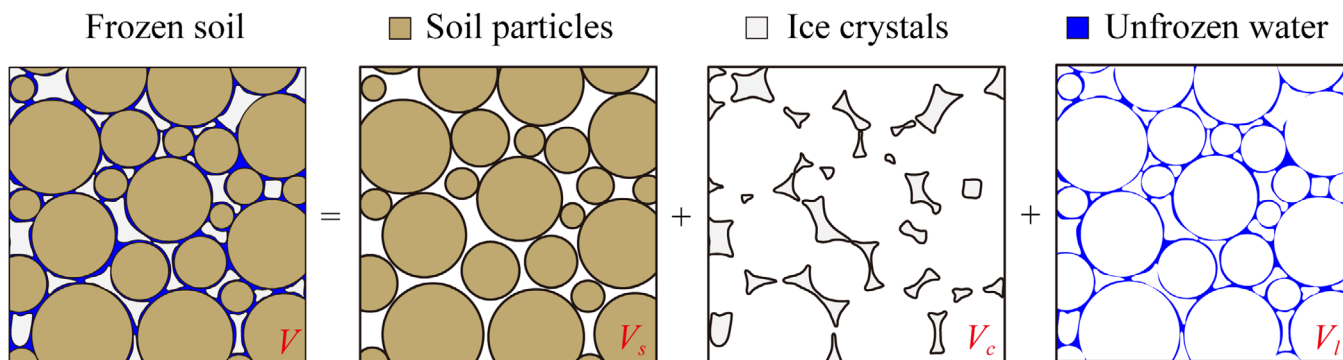


FIGURE 1 Schematic illustration of a frozen soil column as a mixture of soil particles, ice crystals, and unfrozen water.

far, a comprehensive and robust MPM framework for thermo-hydro-mechanically modeling the freeze–thaw behavior in porous media, especially for thawing-induced large deformation and failure, remains lacking.

This study aims to develop a THM-coupled MPM framework for modeling the phase transition and large deformation behavior in ice/water-saturated porous media during dynamic freezing and thawing processes. The mathematical framework will be developed based on the multiphase mixture theory and physically based conservation laws instead of using empirical or semi-empirical equations^{63,64} to describe the coupled interactions of heat transfer, pore-liquid flow, and solid deformation, for example, the phase transition-induced volume change, the latent heat effect, and the convective heat transfer. Existing FEM studies commonly adopted the quasi-static $\mathbf{u} - p - T$ formulation,^{23,38} while in this study, we will develop a four-variable $\mathbf{v}_s - \mathbf{v}_l - p - T$ formulation, which is more suitable for dynamic and large deformation problems.⁶⁵ In the considered triphasic solid–ice–liquid porous mixture, the ice phase will be treated as a solid component contributing to the skeleton's overall load-bearing capacity.^{24,66} The additional strength due to the ice bonding effect, which is widely documented in experimental studies,^{67–72} will be considered in an ice saturation-dependent Mohr–Coulomb model. The phase balance between ice and liquid will be described by a physics-based SFCC derived based on the Clausius–Clapeyron equation and the van Genuchten model.^{23,73} The porosity- and ice saturation-dependent permeability model^{23,74} will be adopted to account for the impact of phase transition and large deformation on the variation of hydraulic conductivity. To improve numerical stability and computational efficiency when dealing with nearly incompressible fluids and extremely low permeability conditions in frozen porous media, a stabilized fractional-step-based semi-implicit integration algorithm will be used to advance the solution of the system.^{54,61} The above framework will be integrated into the one-point, three-phase MPM based on an open-source CB-Geo MPM code.⁷⁵

This paper is structured as follows. Section 2 develops the mathematical equations for saturated frozen soils considering phase transition. Section 3 presents the constitutive models of frozen soil models, including the SFCC, relative hydraulic conductivity, and mechanical models. Section 4 presents the MPM implementation based on the semi-implicit splitting solution scheme. In Section 5, we conduct six numerical examples to validate and demonstrate the proposed method in simulating TH-coupling and THM-coupling problems. Finally, Section 6 provides concluding summaries.

2 | GOVERNING EQUATIONS

2.1 | Homogenization of a frozen porous medium

The THM responses of a frozen porous medium can be effectively analyzed through the use of a representative volume element (RVE) as illustrated in Figure 1. To simplify the analysis, we assume that the RVE is fully saturated with unfrozen pore water. By using the mixture theory,⁷⁶ we treat the multiphase RVE as a macroscopic mixture of solid aggregates (s), liquid (l), and crystal ice (c), which are overlapped, interacting, and statistically distributed.⁷⁷ The volume fraction of each component can be determined by

$$n_\pi = \frac{V_\pi}{V}, \quad \pi \in \{s, l, c\} \quad \text{with } n_s + n_l + n_c = 1 \text{ and } \phi = n_l + n_c, \quad (1)$$

where the subscript π denotes π phase in the triphasic mixture, V_π and V are the partial and total volume, respectively, and ϕ is the porosity. The degree of liquid/ice saturation can be defined as

$$S_l = \frac{V_l}{V_l + V_c}, \quad S_c = \frac{V_c}{V_l + V_c}, \quad (2)$$

such that $n_l = S_l \phi$ and $n_c = S_c \phi$. Accordingly, the partial mass density of each phase and the average mass density of the mixture are given by

$$\bar{\rho}_\pi = n_\pi \rho_\pi, \quad \rho_m = n_s \rho_s + n_l \rho_l + n_c \rho_c, \quad (3)$$

where ρ_π is the intrinsic density of π phase.

2.2 | Conservation of mass

The framework of single-point three-phase MPM is employed in this work. The material point is attached to the solid phase, while the liquid and ice phases move relative to the solid phase. Assuming no mass exchange between the mixture and the surrounding environment, the mass balance equations for each phase are given as follows:

$$\frac{D_s(n_\pi \rho_\pi)}{Dt} + n_\pi \rho_\pi \nabla \cdot \mathbf{v}_\pi + (\mathbf{v}_\pi - \mathbf{v}_s) \cdot \nabla (n_\pi \rho_\pi) = \dot{m}_\pi, \quad (4)$$

where $D_s(*)/Dt$ denotes the material derivative of variable $(*)$ with respect to the solid phase, \mathbf{v}_π is the velocity of π phase, and \dot{m}_π is the rate of mass transferred from π phase to other phases, with $\dot{m}_s = 0$ and $\dot{m}_l = -\dot{m}_c$. We assume the crystal ices move together with the solid phase so that they share the same velocity, that is, $\mathbf{v}_c = \mathbf{v}_s$.

The intrinsic density of each phase can be linked with the temperature and pressure via the equations of state,

$$\frac{1}{\rho_s} \frac{D_s \rho_s}{Dt} = -\beta_s \frac{D_s T}{Dt}, \quad \frac{1}{\rho_c} \frac{D_s \rho_c}{Dt} = -\beta_c \frac{D_s T}{Dt}, \quad \frac{1}{\rho_l} \frac{D_s \rho_l}{Dt} = -\beta_l \frac{D_s T}{Dt} + \frac{1}{K_l} \frac{D_s p_l}{Dt}, \quad (5)$$

where K_l is the bulk module of liquid, and β_π is the thermal expansivity. The influences of solid grains and ice compressibility are neglected.

Combining Equations (4) and (5) and considering $n_s + n_l + n_c = 1$, one can obtain the mass balance equation of the mixture as

$$-\zeta \frac{D_s n_c}{Dt} + \frac{n_l}{K_l} \frac{D_s p_l}{Dt} - \beta_m \frac{D_s T}{Dt} + (1 - \zeta n_c) \nabla \cdot \mathbf{v}_s + \nabla \cdot n_l (\mathbf{v}_l - \mathbf{v}_s) = 0, \quad (6)$$

where $\zeta = 1 - \rho_c/\rho_l$ and $\beta_m = n_s \beta_s + n_l \beta_l + (1 - \zeta) n_c \beta_c$. Here, the spatial variations of the density of liquid water are neglected, that is, $\nabla \rho_l = 0$. The terms in Equation (6) reflect the effect of phase transition, liquid compressibility, thermal expansion, the deformation of solid skeleton, and the flow of liquid on the rate of volume change, respectively. Further relating the ice fraction to temperature, we can formulate Equation (6) as

$$\frac{n_l}{K_l} \frac{D_s p_l}{Dt} + \left(\zeta \phi \frac{\partial S_l}{\partial T} - \beta_m \right) \frac{D_s T}{Dt} + \nabla \cdot n_l (\mathbf{v}_l - \mathbf{v}_s) + (1 - \zeta n_c) \nabla \cdot \mathbf{v}_s = 0. \quad (7)$$

2.3 | Conservation of momentum

The momentum balance equation for each phase reads,

$$n_\pi \rho_\pi \frac{D_s \mathbf{v}_\pi}{Dt} + \dot{m}_\pi \mathbf{v}_\pi = \nabla \cdot \boldsymbol{\sigma}_\pi + n_\pi \rho_\pi \mathbf{b} + \mathbf{f}_\pi, \quad (8)$$

where σ_π is the partial stress tensor acting on π phase, \mathbf{b} is the body force vector, \dot{m}_π is the mass exchange rate defined in Equation (4), and \mathbf{f}_π is the momentum exchange caused by interaction forces. The term $\dot{m}_\pi \mathbf{v}_\pi$ represents the momentum transfer between water and ice during phase transition, which has a negligibly small influence in the system.²³ Besides, the exchange of momenta between phases is an internal phenomenon; thus, the sum of \mathbf{f}_π of all phases is zero, that is, $\sum_\pi \mathbf{f}_\pi = 0$. Therefore, only the drag force and the buoyancy force are considered in this work, while other internal interactions, such as water–ice and water–solid surface tension, are not considered. The drag force between the liquid and the skeleton (including soil grains and ice crystals) is computed according to Darcy's law,⁴⁸

$$\mathbf{f}_l = -(\mathbf{f}_s + \mathbf{f}_c) = p_l \nabla n_l - n_l^2 \frac{\rho_l g}{k_a k_r} (\mathbf{v}_l - \mathbf{v}_s), \quad (9)$$

where g is the gravitational acceleration, k_a is the absolute hydraulic conductivity, and k_r is the relative hydraulic conductivity, dependent on the liquid saturation S_l .

For unfrozen saturated soil, the effective stress theory is widely accepted to link the mechanical response of solid and liquid phases, expressed as

$$\boldsymbol{\sigma} = \boldsymbol{\sigma}' - p\mathbf{I}, \quad (10)$$

where $\boldsymbol{\sigma}'$ is the effective stress, p is the pore pressure, and \mathbf{I} is the identity tensor. However, for frozen soil or partially frozen soil, the pore pressure is contributed by both pore ice pressure p_c and pore water pressure p_l . One simple approach is to use a linear combination of the two²³, that is,

$$p = \chi_l p_l + (1 - \chi_l) p_c, \quad (11)$$

where χ_l is the Bishop coefficient, usually taken as S_l . The pore ice pressure is linked with the pore water pressure and temperature by a thermodynamic equilibrium Clausius–Clapeyron equation. However, pore ice pressure is influenced by the phase balance of ice and water and other factors such as soil types and loading conditions. It is nontrivial to measure the pore ice pressure of soil in experiments. Hence, it is simply assumed that the pore ice is part of the solid, contributing to the skeleton with soil grains together so that the ice pressure will not be modeled separately. As a consequence, the predicted effective stress is the overall stress on both soil grains and crystal ice. The simplified model offers a clear concept for consideration of the effect of pore ice. This also facilitates the implementation of the framework by combining the momentum equations of the solid phase and the ice phase into a single one, that is,

$$(n_s \rho_s + n_c \rho_c) \frac{D_s \mathbf{v}_s}{Dt} = \nabla \cdot [\boldsymbol{\sigma}' - (n_s + n_c) p_l \mathbf{I}] + (n_s \rho_s + n_c \rho_c) \mathbf{b} + n_l^2 \frac{\rho_l g}{k_a k_r} (\mathbf{v}_l - \mathbf{v}_s). \quad (12)$$

To sum up, the momentum balance equations of the mixture and the liquid phase read,

$$(n_s \rho_s + n_c \rho_c) \frac{D_s \mathbf{v}_s}{Dt} + n_l \rho_l \frac{D_s \mathbf{v}_l}{Dt} = \nabla \cdot \boldsymbol{\sigma} + \rho_m \mathbf{b}, \quad (13)$$

$$n_l \rho_l \frac{D_s \mathbf{v}_l}{Dt} = -n_l \nabla p_l + n_l \rho_l \mathbf{b} - n_l^2 \frac{\rho_l g}{k_a k_r} (\mathbf{v}_l - \mathbf{v}_s). \quad (14)$$

2.4 | Conservation of energy

Assuming an isothermal field within an RVE, the energy conservation of the mixture can be expressed as

$$C_m \frac{D_s T}{Dt} - \rho_c L_f \frac{D_s n_c}{Dt} + n_l \rho_l c_l (\mathbf{v}_l - \mathbf{v}_s) \cdot \nabla T + \nabla \cdot \mathbf{q}_T = Q, \quad (15)$$

where $C_m = n_s \rho_s c_s + n_l \rho_l c_l + n_c \rho_c c_c$ is the matrix heat capacity, c_π is the specific heat capacity of π phase, L_f is the latent heat of fusion, Q is the heat source, and \mathbf{q}_T is the conductive heat flux. Heat conduction is calculated based on Fourier's

law

$$\mathbf{q}_T = -\kappa_m \nabla T, \quad (16)$$

where κ_m is the thermal conductivity of the mixture. In this study, we adopt an algebraic average value of all phases, that is, $\kappa_m = n_s \kappa_s + n_l \kappa_l + n_c \kappa_c$, in which κ_π is the thermal conductivity of π phase. Other estimations of κ_m , such as by geometric average, can also be adopted.^{78,79} Considering that n_c is a function of temperature, we can rewrite Equation (15) as

$$\left(C_m + \rho_c L_f \phi \frac{\partial S_l}{\partial T} \right) \frac{D_s T}{Dt} + n_l \rho_l c_l (\mathbf{v}_l - \mathbf{v}_s) \cdot \nabla T + \nabla \cdot (-\kappa_m \nabla T) = Q, \quad (17)$$

where $\tilde{C}_m = C_m + \rho_c L_f \phi \frac{\partial S_l}{\partial T}$ is the effective heat capacity. Such treatment helps to simplify the energy equation to contain only the temperature derivative, thereby facilitating the numerical implementation.

2.5 | Boundary conditions

The triphasic mixture occupies a domain denoted by Ω with the boundary of the domain denoted by $\partial\Omega$. For the presented THM problem, the boundary conditions can be split into Dirichlet (natural) boundaries: $\partial\Omega_{v\pi}$ —velocity boundary, $\partial\Omega_{pl}$ —liquid pressure boundary, $\partial\Omega_T$ —temperature boundary, and Neumann (essential) boundaries: $\partial\Omega_{t\pi}$ —traction boundary, $\partial\Omega_{ql}$ —liquid flux boundary, $\partial\Omega_{qT}$ —heat flux boundary. The boundary conditions are given as follows:

$$\mathbf{v}_\pi = \hat{\mathbf{v}}_\pi \text{ on } \partial\Omega_{v\pi}, \quad (18)$$

$$p_l = \hat{p}_l \text{ on } \partial\Omega_{pl}, \quad (19)$$

$$T = \hat{T} \text{ on } \partial\Omega_T, \quad (20)$$

$$\mathbf{n} \cdot \boldsymbol{\sigma}_\pi = \hat{\mathbf{t}}_\pi \text{ on } \partial\Omega_{t\pi}, \quad (21)$$

$$-\mathbf{n} \cdot \mathbf{q}_l = \hat{q}_l \text{ on } \partial\Omega_{ql}, \quad (22)$$

$$-\mathbf{n} \cdot \mathbf{q}_T = \hat{q}_T \text{ on } \partial\Omega_{qT}, \quad (23)$$

$$-\mathbf{n} \cdot \mathbf{q}_T = h(T_a - T) \text{ on } \partial\Omega_{qT}, \quad (24)$$

where $\mathbf{q}_l (= n_l (\mathbf{v}_l - \mathbf{v}_s))$ is the liquid flux, \mathbf{q}_T is the heat flux, \mathbf{n} is the outward unit surface normal, $\hat{\mathbf{v}}_\pi$, \hat{p}_l , \hat{T} , $\hat{\mathbf{t}}_\pi$, \hat{q}_l , and \hat{q}_T are the specified phase velocity, pore pressure, temperature, phase traction, liquid flux, and heat flux, respectively. Equation (23) represents the conductive heat flux boundary, while Equation (24) represents the convective heat flux boundary in which T_a is the ambient temperature and h is the convective heat transfer coefficient. Note that the related natural and essential boundary conditions must be compatible, that is, $\partial\Omega_{v\pi} \cap \partial\Omega_{t\pi} = \partial\Omega_{pl} \cap \partial\Omega_{ql} = \partial\Omega_T \cap \partial\Omega_{qT} = \emptyset$. The initial conditions at $t = 0$ are given as $\{\mathbf{v}_s^0, \mathbf{v}_l^0, p_l^0, T^0\}$.

3 | CONSTITUTIVE MODELS

3.1 | Soil freezing characteristic curve for partially frozen soil

When simulating freezing or thawing soils, mathematical models require an SFCC to accurately relate the degree of liquid (unfrozen water) saturation S_l to the soil's thermo-mechanical properties. A common approach is to analogize the SFCC from the soil water characteristic curve (SWCC), which is developed to describe the drying and wetting in unsaturated

unfrozen soils. This approach is inspired by the similarities between soil freezing/thawing and soil drying/wetting, as studied in many works. In this section, we introduce an SFCC inspired by the air–water–suction relation in the van Genuchten retention model.⁸⁰ By neglecting the hysteresis of soil freezing characteristic, we can link the liquid water saturation with the temperature T and the pore liquid pressure p_l ,^{23,38}

$$S_l = \left[1 + \left[- \left(1 - \frac{\rho_c}{\rho_l} \right) \frac{p_l}{p_0} - \frac{\rho_c}{p_0} L_f \ln \frac{T + 273.15}{273.15} \right]^{\frac{1}{1-\lambda}} \right]^{-\lambda}, \quad (25)$$

where ρ_c and ρ_l are the intrinsic densities of ice and liquid water, respectively, T is the temperature (in a unit of °C), L_f is the latent heat of fusion of ice, p_0 and λ are material constants. λ is an empirical constant defining the shape of the freezing characteristic curve. A larger value of λ yields a steeper freezing characteristic curve.

3.2 | Hydraulic conductivity for partially frozen and unfrozen soil

The hydraulic conductivity depends on the intrinsic permeability of the porous material, the degree of saturation, and the density and viscosity of the fluid. In frozen soil, the seepage path may be blocked by ice crystals so that the hydraulic conductivity is dependent on the degree of ice or liquid saturation. A widely used relative hydraulic conductivity model is adopted in this study, given as follows²³:

$$k_r = \sqrt{S_l} \left[1 - \left(1 - S_l^{1/m} \right)^m \right]^2, \quad (26)$$

where m is a material constant.

In case of large porosity changes in large deformation problems, the absolute hydraulic conductivity k_a should be related to the porosity, using the following Kozeny–Carman equation⁷⁴:

$$k_a = k_0 \left(\frac{1 - \phi_0^2}{\phi_0^3} \right) \left(\frac{\phi^3}{1 - \phi^2} \right), \quad (27)$$

where k_0 is the hydraulic conductivity under the reference porosity of ϕ_0 . Other SFCC and permeability models^{27,32} can also be employed in our framework without extra effort in implementation. Note that the SFCC and permeability model may significantly influence the solution of the coupling system. Hence, specified models will be used in some benchmark examples to ensure comparability with previous studies.

3.3 | Mechanical constitutive law for soil skeleton with ice crystals

A constitutive model is required to characterize the mechanical response of porous soil during freezing and thawing. For nonisothermal conditions, the constitutive relationship of porous media is expressed as

$$\dot{\boldsymbol{\sigma}}' = \mathbf{D} : (\dot{\boldsymbol{\varepsilon}}_s + \dot{\boldsymbol{\varepsilon}}_T), \quad (28)$$

where $\dot{\boldsymbol{\sigma}}'$ is the rate of effective stress, \mathbf{D} is the tangent matrix that defines the constitutive model, and $\dot{\boldsymbol{\varepsilon}}_s$ and $\dot{\boldsymbol{\varepsilon}}_T$ are the rates of mechanical strain and thermal strain, respectively, given by

$$\dot{\boldsymbol{\varepsilon}}_s = \frac{1}{2} \left[\nabla \mathbf{v}_s + (\nabla \mathbf{v}_s)^T \right], \quad \text{and} \quad \dot{\boldsymbol{\varepsilon}}_T = -\beta_s \dot{T} \mathbf{I}, \quad (29)$$

where \mathbf{v}_s is the solid velocity, β_s is the coefficient of thermal expansion of the skeleton, and \mathbf{I} is the identity tensor. Note that we adopt the strain rate, also known as the rate of deformation, as the strain measure in current work. It assumes the incremental strain in each incremental step is small. This assumption is widely accepted for explicit stress integration in the updated Lagrangian MPM. Besides, we employ an objective stress rate, the Jaumann rate, to update stress in case of large deformations. However, it should be pointed out that although the rate of deformation and Cauchy stress are

frequently used in MPM formations, the precise application of large deformation Lagrangian mechanics requires other large deformation strain and stress measures, such as the Green strain and the Piola–Kirchhoff stress.⁸¹ More detailed discussion on this issue can be found in Coomb et al.'s work.^{82,83}

Any proper elastoplastic constitutive model for frozen soil^{23,24,38,42} can be incorporated into the framework to describe the stress–strain relations. Without losing generality, a simple elastoplastic nonassociated Mohr–Coulomb softening model is adopted. The yield function F and flow potential function P defined in terms of friction angle φ , cohesion c , and dilation ψ , are given by

$$F = R_{mc}q + p \tan \varphi - c, \quad (30)$$

$$P = \sqrt{(\epsilon c \tan \psi)^2 + (R_{mw}q)^2} + p \tan \psi, \quad (31)$$

with

$$R_{mc}(\theta, \varphi) = \frac{1}{\sqrt{3} \cos \varphi} \sin \left(\theta + \frac{\pi}{3} \right) + \frac{1}{3} \cos \left(\theta + \frac{\pi}{3} \right) \tan \varphi, \quad (32)$$

$$R_{mw}(\theta, e) = \frac{4(1 - e^2) \cos^2 \theta + (2e - 1)^2}{2(1 - e^2) \cos \theta + (2e - 1) \sqrt{4(1 - e^2) \cos^2 \theta + 5e^2 - 4e}} R_{mc} \left(\frac{\pi}{3}, \varphi \right), \quad (33)$$

where p and q are the effective mean stress and the deviatoric stress, respectively, θ is the Lode's angle, ϵ is a parameter referred to as the meridional eccentricity, $e = (3 - \sin \varphi) / (3 + \sin \varphi)$ is a parameter referred to as the deviatoric eccentricity.

The strength parameters c and φ are redefined as follows to capture the evolution of yield surface with respect to soil softening and ice cementation⁸⁴:

$$\Psi = \Psi' + \Psi_s, \quad \Psi \in \{c, \varphi\}, \quad (34)$$

where Ψ' is the effective strength, and Ψ_s is the additional cohesion and friction strength due to ice cementation.

Large deformation may cause localized failure patterns in soil, leading to a decrease in the effective strength of the soil with the accumulation of plastic strain. This phenomenon can be captured by an exponential strain-softening model^{47,59}:

$$\Psi' = \Psi'_{res} + (\Psi'_p - \Psi'_{res}) \exp(-\eta_s \epsilon_p^d), \quad (35)$$

where the subscript “ p ” and “ res ” represent the “*peak*” and “*residual*” values of strength parameters, respectively, and η_s is the shape factor that controls the degree of strength reduction.

The additional cohesion and friction strength due to ice cementation can be captured by⁸⁵

$$\Psi_s = \Delta \Psi_{max} [1 - \exp(-\eta_c s_c)], \quad (36)$$

where $\Delta \Psi_{max}$ is the maximum incremental strength due to ice cementation, η_c is a shape parameter defining the effect of ice cementation on strength parameters, and s_c is the ice-saturation-dependent variable,^{23,38,42} defined as follows:

$$s_c = \left[(1 - S_c)^{-1/\lambda} - 1 \right]^{1-\lambda}, \quad (37)$$

where S_c is the degree of ice saturation, λ is a material constant defined in Equation (25). Note that both the strength and stiffness are influenced by the formation or melting of ice during soil freezing and thawing processes, which can be considered in a more sophisticated model, for example, by linking the elastic parameters with S_c or directly with temperature, compare Ref. 86.

4 | MPM IMPLEMENTATION

In poromechanics, a major difficulty for numerical solutions is that the velocity and the pressure are coupled by the incompressibility constraint.^{87–90} Such incompressibility constraint applies when the solid and fluid phases are nearly

incompressible and the permeability or time step is not large enough to induce relative flow between the solid and fluid phases.⁹¹ For the simulation of frozen porous media, the problem is more prominent since the permeability could be extremely small. In this study, we employ a fractional-step-based semi-implicit MPM to overcome the incompressibility constraint, which can offer good numerical stability while maintaining computational efficiency.

4.1 | Semi-discrete equations

In MPM, explicit time stepping is the most commonly used scheme due to its simplicity and high adaptivity for high-frequency and dynamic problems. For hydro-mechanical problems, the explicit scheme requires an assumption of weakly compressible fluid to facilitate the solution of pore pressure. The liquid compressibility inevitably introduces extra instabilities.⁵³ Moreover, the critical time step size is highly dependent on the liquid compressibility and the permeability—low compressibility and low permeability will lead to a very small time step size.^{54,92} Therefore, the explicit scheme may not be a good choice for modeling ice-rich low-permeability soils. The coupled equations can also be solved in a monolithic implicit manner. The implicit monolithic solution scheme permits using a large time step, but it must fulfill the Ladyszenskaya–Babuska–Brezzi (LBB) condition.⁹³ Otherwise, for example, when the equal-order element is used for pressure and velocity interpolation, it will generate unphysical checkerboard pressure modes.⁹¹ Stable mixed-order elements can circumvent the pressure oscillations but will significantly increase the computation time,^{89,90} and the MPM formulations have to be restructured. Besides, monolithically solving all unknowns involves handling large matrices and iterative solutions, which may lead to many other issues related to numerical convergence, computational efficiency, and code implementation.⁹⁴

In this work, we use an alternative semi-implicit splitting solution scheme based on the fractional step method. The fractional step method, also known as the projection method, was initially proposed by Chorin⁹⁵ for solving incompressible Navier–Stokes equations and later developed with different variants.^{87,96–102} It has subsequently been extended to model poremechanics in FEM^{93,103–105} and recently for MPM.^{54,61,106} The main feature of the method is that it decouples the pore-pressure field from the kinematic fields by splitting the momentum equations into a predicting part and a correcting part via intermediate velocities v_{π}^* . The decoupled equations are solved using a semi-implicit time integration in which the temperature and stress terms are solved explicitly while the pressure and drag force terms are treated implicitly. The starting point for this choice is to reduce the workload for matrix treatment and iterative solutions. The advantage of using the semi-implicit splitting solution scheme to solve the coupled problem is at least threefold.

1. The pressure and velocities are decoupled so that the unphysical pressure oscillations can be largely reduced^{93,107,108};
2. The time step size is independent of liquid compressibility and permeability, thereby offering better computational efficiency compared to pure explicit method for modeling poorly permeable frozen porous media^{54,109};
3. In each time step, one only needs to solve a sequence of decoupled equations for temperature, velocity, and pressure, making it very efficient for large-scale numerical simulations.⁸⁷

The notations used in the following equations are defined as follows: the superscripts “ k ” and “ $k + 1$ ” represent the current time step and the next time step, respectively; \mathbf{v}_{π}^{k+1} , p_l^{k+1} , and T^{k+1} denote the rate of velocities, pore pressure, and temperature, respectively, at the next time step.

Specifically, the energy equation is temporally discretized using an explicit scheme, as adopted in most MPM thermo-mechanical coupling solvers,^{110–112}

$$\left(C_m + \rho_c L_f \phi \frac{\partial S_l}{\partial T} \right) T^{k+1} + n_l \rho_l c_l (\mathbf{v}_l^k - \mathbf{v}_s^k) \cdot \nabla T^k + \nabla \cdot (-\kappa_m \nabla T^k) = Q. \quad (38)$$

The momentum balance equations are discretized using the following semi-implicit scheme:

$$\begin{cases} (n_s \rho_s + n_c \rho_c) \mathbf{v}_s^{k+1} + n_l \rho_l \mathbf{v}_l^{k+1} = \nabla \cdot (\boldsymbol{\sigma}^{k+1} - p_l^{k+1} \mathbf{I}) + \rho_m \mathbf{b}, \\ n_l \rho_l \mathbf{v}_l^{k+1} = -n_l \nabla p_l^{k+1} + n_l \rho_l \mathbf{b} - n_l^2 \frac{\rho_l g}{k_a k_r} (\mathbf{v}_l^{k+1} - \mathbf{v}_s^{k+1}). \end{cases} \quad (39)$$

The mass balance equation is discretized in the following implicit manner:

$$\left(\zeta\phi\frac{\partial S_l}{\partial T} - \beta_m\right)\dot{T}^{k+1} + \frac{n_l}{K_l}\dot{p}_l^{k+1} + \nabla \cdot n_l(\mathbf{v}_l^{k+1} - \mathbf{v}_s^{k+1}) + (1 - \zeta n_c)\nabla \cdot \mathbf{v}_s^{k+1} = 0. \quad (40)$$

Here, the stress term in the momentum balance equation is treated explicitly, while the drag force term and the pressure term are evaluated in an implicit manner. This leads to the semi-implicit time integration in which some of the advantages of the pure explicit and pure implicit schemes are realized while the drawbacks are reduced.

The rate of primary unknowns is approximated by the first-order forward difference,

$$\mathbf{v}_\pi^{k+1} = \frac{\mathbf{v}_\pi^{k+1} - \mathbf{v}_\pi^k}{\Delta t}, \quad \dot{p}_l^{k+1} = \frac{p_l^{k+1} - p_l^k}{\Delta t}, \quad \dot{T}^{k+1} = \frac{T^{k+1} - T^k}{\Delta t}, \quad (41)$$

where Δt is the time step size. To proceed with the fractional step splitting, the rate of velocities (accelerations) is split into a predicting one (\mathbf{v}_π^*) and a correcting one (\mathbf{v}_π^{**}),

$$\mathbf{v}_\pi^{k+1} = \mathbf{v}_\pi^* + \mathbf{v}_\pi^{**}, \quad \text{with } \mathbf{v}_\pi^* = \frac{\mathbf{v}_\pi^* - \mathbf{v}_\pi^k}{\Delta t} \text{ and } \mathbf{v}_\pi^{**} = \frac{\mathbf{v}_\pi^{k+1} - \mathbf{v}_\pi^*}{\Delta t}, \quad (42)$$

where \mathbf{v}_π^* is named the intermediate velocity and \mathbf{v}_π^{k+1} often termed the end-of-step velocity.

Then, based on Equation (42), the momentum equation is split into the predicting part,

$$\begin{cases} (n_s\rho_s + n_c\rho_c)\mathbf{v}_s^* + n_l\rho_l\mathbf{v}_l^* = \nabla \cdot (\boldsymbol{\sigma}^{k+1} - p_l^k\mathbf{I}) + \rho_m\mathbf{b}, \\ n_l\rho_l\mathbf{v}_l^* = -n_l\nabla p_l^k + n_l\rho_l\mathbf{b} - n_l^2\frac{\rho_l g}{k_a k_r}(\mathbf{v}_l^* - \mathbf{v}_s^*), \end{cases} \quad (43)$$

and the correcting part,

$$\begin{cases} (n_s\rho_s + n_c\rho_c)\mathbf{v}_s^{**} + n_l\rho_l\mathbf{v}_l^{**} = -(n_s + n_c)\nabla(p_l^{k+1} - p_l^k), \\ n_l\rho_l\mathbf{v}_l^{**} = -n_l\nabla(p_l^{k+1} - p_l^k) - n_l^2\frac{\rho_l g}{k_a k_r}[(\mathbf{v}_l^{k+1} - \mathbf{v}_l^*) - (\mathbf{v}_s^{k+1} - \mathbf{v}_s^*)]. \end{cases} \quad (44)$$

In the predicting step (Equation 43), the pore pressure is held constant, and only the intermediate velocities are to be solved. However, the end-of-step velocities \mathbf{v}_π^{k+1} and the incremental pore pressure $(p_l^{k+1} - p_l^k)$ are still coupled in the correcting part of the momentum equation (44) and the mass balance equation (40).

Noting that Equation (44) can be rewritten in an explicit manner of \mathbf{v}_π^{**} ,

$$\begin{cases} (n_s\rho_s + n_c\rho_c)\mathbf{v}_s^{**} = -\xi_s(n_s + n_c)\nabla(p_l^{k+1} - p_l^k), \\ n_l\rho_l\mathbf{v}_l^{**} = -\xi_l n_l\nabla(p_l^{k+1} - p_l^k), \end{cases} \quad (45)$$

with

$$\xi_s = \frac{n_l\rho_l(n_s\rho_s + n_c\rho_c) + \Delta t C_d(n_s\rho_s + n_c\rho_c)(n_s + n_c)}{n_l\rho_l(n_s\rho_s + n_c\rho_c) + \Delta t C_d\rho_m}, \quad \xi_l = \frac{n_l\rho_l(n_s\rho_s + n_c\rho_c) + \Delta t C_d n_l\rho_l}{n_l\rho_l(n_s\rho_s + n_c\rho_c) + \Delta t C_d\rho_m}, \quad (46)$$

where $C_d = n_l^2\frac{\rho_l g}{k_a k_r}$ is the drag force coefficient. According to the expression of \mathbf{v}_π^{**} in Equation (42), Equation (45) can be further rewritten in terms of \mathbf{v}_π^{k+1} ,

$$\begin{cases} \mathbf{v}_s^{k+1} = -\Delta t \xi_s \frac{n_s + n_c}{n_s\rho_s + n_c\rho_c} \nabla(p_l^{k+1} - p_l^k) + \mathbf{v}_s^*, \\ \mathbf{v}_l^{k+1} = -\Delta t \xi_l \frac{1}{\rho_l} \nabla(p_l^{k+1} - p_l^k) + \mathbf{v}_l^*. \end{cases} \quad (47)$$

Finally, by substituting Equation(47) into Equation(40), \mathbf{v}_π^{k+1} can be canceled, and the pressure Poisson equation can be obtained,

$$\Delta t \eta \nabla^2 (p_l^{k+1} - p_l^k) - \frac{n_l}{K_l} \dot{p}_l^{k+1} - \left(\zeta \phi \frac{\partial S_l}{\partial T} - \beta_m \right) \dot{T}^{k+1} - (1 - \zeta n_c) \nabla \cdot \mathbf{v}_s^* - \nabla \cdot n_l (\mathbf{v}_l^* - \mathbf{v}_s^*) = 0, \quad (48)$$

with

$$\eta = \xi_l \frac{n_l}{\rho_l} + \xi_s (n_s + n_c - \zeta n_c) \frac{n_s + n_c}{n_s \rho_s + n_c \rho_c}. \quad (49)$$

As summary, the overall solution strategy is illustrated as follows:

$$\begin{pmatrix} \mathbf{v}_s^k \\ \mathbf{v}_l^k \\ p_l^k \\ T^k \end{pmatrix} \xrightarrow{(1)} \begin{pmatrix} \mathbf{v}_s^k \\ \mathbf{v}_l^k \\ p_l^k \\ \dot{T}^{k+1} \end{pmatrix} \xrightarrow{(2)} \begin{pmatrix} \mathbf{v}_s^* \\ \mathbf{v}_l^* \\ p_l^k \\ \dot{T}^{k+1} \end{pmatrix} \xrightarrow{(3)} \begin{pmatrix} \mathbf{v}_s^* \\ \mathbf{v}_l^* \\ \Delta p_l^{k+1} \\ \dot{T}^{k+1} \end{pmatrix} \xrightarrow{(4)} \begin{pmatrix} \mathbf{v}_s^{k+1} \\ \mathbf{v}_l^{k+1} \\ \Delta p_l^{k+1} \\ \dot{T}^{k+1} \end{pmatrix}. \quad (50)$$

The temperature \dot{T}^{k+1} is first solved explicitly by Equation (38), using the current step velocities and temperature, \mathbf{v}_π^k and T^k . The resulting temperature is then used to advance the hydro-mechanical coupled equations. In step (2), the intermediate velocities, \mathbf{v}_s^* and \mathbf{v}_l^* , are calculated by solving Equation (43). Then, in step (3), the pore pressure increment Δp_l^{k+1} ($= p_l^{k+1} - p_l^k$) is solved based on the updated temperature \dot{T}^{k+1} and the intermediate velocities \mathbf{v}_π^* . Finally, the end-of-step velocities \mathbf{v}_π^{k+1} can be calculated based on updated Δp_l^{k+1} . It is worth noting that the temperature equation can either be solved in the first step with the resulting temperature serving as the input of subsequent steps or be solved in the last step to make use of the pre-updated kinematic variables.

4.2 | Weak formulations

The partitioned governing equations are transformed into weak formulations based on the standard Galerkin procedure. Considering the boundary conditions, the virtual work equations can be obtained by multiplying corresponding equations with test functions and integrating over the whole domain Ω .

By multiplying the test function δT (with zeros on $\partial\Omega_T$) and applying the integral by part and the divergence theorem, the weak form of the time discrete energy equation can be written as

$$\begin{aligned} \int_{\Omega} \delta T \cdot \left(C_m + \rho_c L_f \phi \frac{\partial S_l}{\partial T} \right) \dot{T}^{k+1} dV = & - \int_{\Omega} \delta T \cdot n_l \rho_l c_l (\mathbf{v}_l^k - \mathbf{v}_s^k) \nabla T dV + \int_{\Omega} \nabla \delta T \cdot (-\kappa_m \nabla T^k) dV \\ & - \int_{\partial\Omega} \delta T \cdot \hat{q}_T dS + \int_{\Omega} \delta T \cdot Q dV, \end{aligned} \quad (51)$$

where \hat{q}_T is the prescribed boundary heat flux defined in Equations (23) and (24). For the conforming boundary conditions where the boundary for the material domain aligns with the mesh boundary, the heat flux boundary, as well as the temperature boundary, can be directly imposed on the nodes by explicitly modifying the nodal values. In this condition, the homogeneous heat flux boundary (i.e., adiabatic boundary) is automatically satisfied. For nonconforming boundary conditions, the boundary conditions can be applied to boundary particle layers. For free-surface particles, it is also convenient to apply to the related boundary nodes with a proper surface particle/node detection technique.^{113,114}

Similarly, by introducing test functions $\delta \mathbf{v}_\pi$ (with zeros on $\partial\Omega_{v_\pi}$), the weak form for the momentum balance equation can be formulated as

Predicting part:

$$\int_{\Omega} \delta \mathbf{v}_s \cdot (n_s \rho_s + n_c \rho_c) \mathbf{v}_s^* dV + \int_{\Omega} \delta \mathbf{v}_s \cdot n_l \rho_l \mathbf{v}_l^* dV = \int_{\partial\Omega} \delta \mathbf{v}_s \cdot \hat{\mathbf{t}} dS - \int_{\Omega} \nabla \delta \mathbf{v}_s : \boldsymbol{\sigma}^k dV + \int_{\Omega} \delta \mathbf{v}_s \cdot \rho_m \mathbf{b} dV, \quad (52)$$

$$\int_{\Omega} \delta \mathbf{v}_l \cdot n_l \rho_l \mathbf{v}_l^* dV = \int_{\partial\Omega} \delta \mathbf{v}_l \cdot \hat{\mathbf{t}}_l dS - \int_{\Omega} \nabla \delta \mathbf{v}_l : (-n_l p_l^k \mathbf{I}) dV + \int_{\Omega} \delta \mathbf{v}_l \cdot n_l \rho_l \mathbf{b} dV - \int_{\Omega} \delta \mathbf{v}_l \cdot n_l^2 \frac{\rho_l g}{k_a k_r} (\mathbf{v}_l^* - \mathbf{v}_s^*) dV. \quad (53)$$

Correcting part:

$$\int_{\Omega} \delta \mathbf{v}_s \cdot (n_s \rho_s + n_c \rho_c) \mathbf{v}_s^{**} dV = - \int_{\Omega} \delta \mathbf{v}_s \cdot \xi_s (n_s + n_c) \nabla (p_l^{k+1} - p_l^k) dV, \quad (54)$$

$$\int_{\Omega} \delta \mathbf{v}_l \cdot n_l \rho_l \mathbf{v}_l^{**} dV = - \int_{\Omega} \delta \mathbf{v}_l \cdot \xi_l n_l \nabla (p_l^{k+1} - p_l^k) dV, \quad (55)$$

where $\hat{\boldsymbol{\sigma}} (= \hat{\boldsymbol{\sigma}}_s + \hat{\boldsymbol{\sigma}}_l)$ and $\hat{\boldsymbol{\sigma}}_{\pi}$ are the prescribed mixture and phase-wise boundary traction, defined in Equation (21). It is worth noting that the intermediate velocities are also assumed to satisfy the same Dirichlet boundary conditions as the end-of-step velocities, that is, $\mathbf{v}_{\pi}^* = \mathbf{v}_{\pi}^{k+1}$ on $\partial\Omega_{v\pi}$. This can be enforced by assigning the nodal intermediate accelerations \mathbf{v}_{π}^* when solving the predictors. For homogeneous velocity boundary (fixed boundary), it leads to $\mathbf{v}_{\pi}^* = \mathbf{0}$, while for inhomogeneous velocity boundary (e.g., footing penetration problem in Section 5.3.2), the nodal intermediate accelerations are estimated by $\mathbf{v}_{\pi}^* = (\mathbf{v}_{\pi}^{k+1} - \mathbf{v}_{\pi}^k) / \Delta t$.

Finally, by introducing the test function δp (with zeros on $\partial\Omega_p$), the weak form for the pressure Poisson Equation is formulated as

$$\begin{aligned} \int_{\Omega} \nabla \delta p \cdot \Delta t \eta \nabla (p_l^{k+1} - p_l^k) dV + \int_{\Omega} \delta p \cdot \frac{n_l}{K_l} p_l^{k+1} dV = \int_{\partial\Omega} \delta p \cdot \hat{q}_l^{k+1} dS - \int_{\Omega} \delta p \cdot \left(\zeta \phi \frac{\partial S_l}{\partial T} - \beta_m \right) \dot{T}^{k+1} dV \\ - \int_{\Omega} \delta p \cdot \nabla \cdot (1 - \zeta n_c) \mathbf{v}_s^* dV + \int_{\Omega} \nabla \delta p \cdot n_l (\mathbf{v}_l^* - \mathbf{v}_s^*) dV, \end{aligned} \quad (56)$$

where \hat{q}_l^{k+1} is the artificial Neumann boundary condition arising from the momentum splitting, expressed as

$$\hat{q}_l^{k+1} = \Delta t \eta \nabla (p_l^{k+1} - p_l^k) \cdot \mathbf{n} - n_l (\mathbf{v}_l^* - \mathbf{v}_s^*) \cdot \mathbf{n}. \quad (57)$$

Here, \hat{q}_l^{k+1} is similar to the liquid flux boundary, but the treatment of the boundary is not as straightforward as for the monolithic case. However, most initial-boundary-value problems proceed either from undrained (no-flow) boundaries with $n_l (\mathbf{v}_l^* - \mathbf{v}_s^*) \cdot \mathbf{n} \equiv \mathbf{0}$ and $\nabla (p_l^{k+1} - p_l^k) \cdot \mathbf{n} \equiv 0$ or fully permeable conditions (free surface) with $p_l \equiv \mathbf{0}$, such that Equation (57) simplify accordingly.⁹³ Moreover, the pressure Poisson equation requires an incremental pressure boundary condition $\Delta p_l^{k+1} = p_l^{k+1} - p_l^k$. Since pore pressure is implicitly solved, the incremental pressure boundary should be implicitly imposed on nodes where pore pressure is prescribed. For the free-surface problems, the evolution of free-surface node should also be tracked.

Although it is clear that the boundary conditions can be applied on either nodes or particles, a precise prescription of boundary conditions is not simple work in MPM, especially for nonconforming conditions. For example, if the boundary traction or heat flux is applied on the boundary particles and then mapped to related nodes, this will possibly introduce additional errors. This motivates researchers to develop more accurate boundary imposition methods, see, for example, Refs. 115–120.

4.3 | MPM spatial discretization

The material domain Ω is discretized into a finite number of disjoint subdomains Ω_p . Each subdomain is represented by a material point (interchangeable with the term “particle”). The original MPM proposed by Sulsky et al.^{39,121} suffers from the so-called crossing-cell noise. This issue stems from the interpolation function utilized in the original MPM, which is only C^0 continuous. As a result, the gradient properties become discontinuous when particles cross the cell boundary. Recent variants of MPM, such as the GIMP method¹²² and the B-spline MPM,¹²³ can significantly reduce the crossing-cell instability by using higher-order interpolation functions. In this work, the GIMP method is used to discretize the weak formulations. 1D GIMP shape functions are obtained by multiplying the grid basis function N_i and the particle characteristic function χ_p and integrating on the particle domain as follows:

$$S_{ip} = \frac{1}{V_p} \int_{\Omega_p \cap \Omega} \chi_p(x) N_i(x) dV, \quad \nabla S_{ip} = \frac{1}{V_p} \int_{\Omega_p \cap \Omega} \chi_p(x) \nabla N_i(x) dV, \quad (58)$$

where S_{ip} and ∇S_{ip} are the GIMP shape function and its gradient, and $V_p = \int_{\Omega_p} \chi_p(x) dV$ is the volume of particle p . 2D and 3D GIMP shape functions can be obtained by-products of each dimension. For simplicity but without losing generality, we adopt a linear grid basis function and a hat-shaped particle characteristic function, which offers a C^1 continuity. Absolutely, one can introduce high-order grid basis functions to generate C^2 -continuous GIMP shape functions or directly use cubic B-spline basis function, which is also C^2 continuous, as MPM shape functions. The fractional step time integration permits an equal-order interpolation for pressure and displacement so that all the variables can use a unified set of MPM shape functions while reducing the inf-sup instability. Therefore, the trial solution fields and the test functions are approximated as

$$\begin{cases} \mathbf{v}_s = \mathbf{S} \cdot \mathbf{v}_s \\ \mathbf{v}_l = \mathbf{S} \cdot \mathbf{v}_l \\ p_l = \mathbf{S} \cdot \mathbf{p}_l \\ T = \mathbf{S} \cdot \mathcal{T} \end{cases}, \quad \begin{cases} \delta \mathbf{v}_s = \mathbf{S} \cdot \delta \mathbf{v}_s \\ \delta \mathbf{v}_l = \mathbf{S} \cdot \delta \mathbf{v}_l \\ \delta p = \mathbf{S} \cdot \delta \mathbf{p}_l \\ \delta T = \mathbf{S} \cdot \delta \mathcal{T} \end{cases}, \quad (59)$$

where \mathbf{v}_π , \mathbf{p}_l , and \mathcal{T} are the nodal arrays of velocity, pore pressure, and temperature, and \mathbf{S} is the array of the shape functions.

By applying Equation (59) and canceling the test functions, the weak formulations can be discretized as follows:

- Energy balance equation:

$$\mathcal{M}_{44} \dot{\mathcal{T}}^{k+1} - \mathbf{f}_4 = 0, \quad (60)$$

- Momentum balance equations—predicting part:

$$\begin{bmatrix} \mathcal{M}_{11} & \mathcal{M}_{12} \\ 0 & \mathcal{M}_{22} \end{bmatrix} \begin{bmatrix} \dot{\mathbf{v}}_s^* \\ \dot{\mathbf{v}}_l^* \end{bmatrix} + \begin{bmatrix} 0 & 0 \\ \mathcal{K}_{21} & \mathcal{K}_{22} \end{bmatrix} \begin{bmatrix} \mathbf{v}_s^* \\ \mathbf{v}_l^* \end{bmatrix} = \begin{bmatrix} \mathbf{f}_1 \\ \mathbf{f}_2 \end{bmatrix}, \quad (61)$$

- Pressure Poisson equation:

$$\mathcal{M}_{33} \dot{\mathbf{p}}_l^{k+1} + \mathcal{M}_{34} \dot{\mathcal{T}}^{k+1} + \mathcal{K}_{31} \mathbf{v}_s^* + \mathcal{K}_{32} \mathbf{v}_l^* + \mathcal{K}_{33} (\mathbf{p}_l^{k+1} - \mathbf{p}_l^k) - \mathbf{f}_3 = 0, \quad (62)$$

- Momentum balance equations—correcting part:

$$\begin{bmatrix} \mathcal{M}_{11} & 0 \\ 0 & \mathcal{M}_{22} \end{bmatrix} \begin{bmatrix} \dot{\mathbf{v}}_s^{**} \\ \dot{\mathbf{v}}_l^{**} \end{bmatrix} = - \begin{bmatrix} \mathcal{K}_{13} (\mathbf{p}_l^{k+1} - \mathbf{p}_l^k) \\ \mathcal{K}_{23} (\mathbf{p}_l^{k+1} - \mathbf{p}_l^k) \end{bmatrix}, \quad (63)$$

where \mathcal{M}_{11} , \mathcal{M}_{22} , \mathcal{M}_{33} , \mathcal{M}_{34} , and \mathcal{M}_{44} are generalized mass matrices; \mathcal{K}_{13} , \mathcal{K}_{23} , \mathcal{K}_{21} , \mathcal{K}_{22} , \mathcal{K}_{31} , \mathcal{K}_{32} , and \mathcal{K}_{33} are generalized stiffness matrices; and \mathbf{f}_1 , \mathbf{f}_2 , \mathbf{f}_3 , and \mathbf{f}_4 are nodal arrays of force vectors. These matrices and vectors are given in Appendix A.

4.4 | Solution algorithm

For the implementation of multiphysics and multiphase MPM, ensuring numerical stability is of great importance. Apart from the crossing-cell noise and the inf-sup instability mentioned in previous sections, there are also many other sources of instability in MPM, such as the ringing instability due to particle-grid mapping,¹²⁴ the checkerboard stress oscillation due to volumetric or shear locking,¹²⁵ and the boundary instability arising from the arbitrary nature of material domain relative to the mesh boundary.^{117,118} A vast number of new methods have been proposed to tackle these issues, such as α PIC method,¹²⁶ XPIC method,^{127–129} $\bar{\mathbf{B}}$ method,⁴⁸ $\bar{\mathbf{F}}$ method,^{83,130} ghost stabilization technique,¹¹⁷ and so forth.

In the current THM-coupled MPM, it has been observed that the particle temperature interpolated from nodal incremental temperature, known as the FLIP temperature, also suffers local oscillation near the temperature boundary or

where the temperature field is highly discontinuous. This is also attributed to the use of low-order shape functions used for temperature interpolation. Although this oscillation has little influence on the global temperature solution, it can lead to local abnormality for other temperature-dependent variables, such as the degree of liquid saturation. It has also been found that the extrapolated nodal temperature, termed here as the PIC temperature, is smoother, but it suffers from unphysical numerical conduction over time. The phenomenon is also found by Nairn and Guilkey.¹¹⁰ An effective method to address this issue is by using the FLIP temperature to advance the solution of the governing equations while using the PIC temperature as input for other variables. The two temperatures can be calculated as follows^{62,112}:

$$\left(T_p^{k+1}\right)_{\text{FLIP}} = T_p^k + \Delta t \sum_i \dot{T}_i^{k+1} S_{ip}, \quad (64)$$

$$\left(T_p^{k+1}\right)_{\text{PIC}} = \sum_i T_i^{k+1} S_{ip}. \quad (65)$$

Although the employment of the fractional step method can largely reduce the pressure oscillation arising from the low-order interpolations, the issue may persist when a considerably large timestep is used.^{87,97} To further reduce the influence of inf-sup instability, we follow the treatment proposed by White and Borja⁸⁸ and Zhao and Choo.^{52,91} The stabilization method, termed the polynomial pressure projection method, adds a penalty term to the mass balance equation, thereby ensuring the whole system satisfies a weak inf-sup condition. In this method, the additional term is added to the Pressure Poisson equation as follows:

$$\mathcal{M}_{33} \dot{\boldsymbol{r}}_l^{k+1} + \mathcal{M}_{34} \dot{\mathcal{T}}^{k+1} + \mathcal{K}_{31} \boldsymbol{v}_s^* + \mathcal{K}_{32} \boldsymbol{v}_l^* + \mathcal{K}_{33} (\boldsymbol{r}_l^{k+1} - \boldsymbol{r}_l^k) + \mathcal{H}_{stab} (\boldsymbol{r}_l^{k+1} - \boldsymbol{r}_l^k) - \boldsymbol{f}_3 = 0, \quad (66)$$

where \mathcal{H}_{stab} is the stabilization matrix, written as

$$\mathcal{H}_{stab} = \int_{\Omega} \frac{\tau}{2G} (\boldsymbol{S}^T - \prod \boldsymbol{S}^T) (\boldsymbol{s} - \prod \boldsymbol{s}) dV, \quad (67)$$

where \boldsymbol{S} is the array of shape functions, $\prod \boldsymbol{S}$ is defined as the cell-averaged shape function, G is the shear modulus of the solid material, and τ is a stabilization parameter. The default value of τ is 1. It is important to note that a large value of τ can improve the stabilization effect but may induce extra pore pressure dissipation, especially in the presence of extremely sharp gradients, as stated by White and Borja themselves.⁸⁸ Therefore, the proper choice of a stabilization parameter is important for successful stabilization. More details on the selection of the stabilization parameter can be found in Refs. 52, 131. Moreover, adding a small compressibility for fluid in matrix \mathcal{M}_{33} can also improve the stability of the system. Other stabilization methods, such as adding some artificial compressibility for the mixture, may be equally effective. The readers may refer to Ref. 93 for details about artificial compressibility.

The solution procedure of the proposed MPM for multiphysics modeling of the freeze–thaw of porous media is presented in Algorithm 1.

5 | NUMERICAL EXAMPLES

In this section, we will evaluate the performance of the proposed framework through several numerical examples. First, we will verify the thermo-hydraulic (TH) coupling during freezing and thawing by comparing our results with those of two benchmark examples. Subsequently, we will validate the THM coupling through two experimental examples. Finally, we will present two THM-coupled large deformation problems to demonstrate the capability of the proposed framework in simulating thawing-related failures. The mechanical and thermal properties of ice and water used in the following examples are presented in Table 1. Note that the parameters used for different examples may vary slightly to maintain consistency with the referenced case.

5.1 | Verification of TH-coupled MPM

5.1.1 | Frozen inclusion thaw

The first example, known as the “frozen inclusion thaw,” was designed by Grenier et al.³⁶ to validate their codes for modeling thermal hydrologic processes in porous systems undergoing freezing and thawing. It has been benchmarked

ALGORITHM 1 MPM algorithm for multiphysics modeling of freezing and thawing porous media.

- 1: **if** $t = 0$ **then**
- 2: Initialize material points.
- 3: Assign material point properties: $V_p^0, \rho_{\pi p}^0, n_{\pi p}^0, T_p^0, S_{lp}^0, n_{sp}^0, \sigma_p^0, p_{lp}^0, \mathbf{v}_{\pi p}^0, k_p^0$.
- 4: **end if**
- 5: **while** $t \leq t_{end}$ **do**
- 6: Initialize background mesh.
- 7: Map particle information to nodes and compute nodal velocities and temperature:

$$\mathbf{v}_{si}^k = \sum_p (m_{sp}^k + m_{cp}^k) \mathbf{v}_{sp}^k S_{ip} / \sum_p (m_{sp}^k + m_{cp}^k) S_{ip},$$

$$\mathbf{v}_{li}^k = \sum_p m_{lp}^k \mathbf{v}_{lp}^k S_{ip} / \sum_p m_{lp}^k S_{ip},$$

$$T_i^k = \sum_p V_p^k C_{mp}^k T_p^k S_{ip} / \sum_p V_p^k C_{mp}^k S_{ip}.$$
- 8: Compute particle strain: $\Delta \boldsymbol{\varepsilon}_p^{k+1} = \frac{1}{2} \Delta t [\sum_i \mathbf{v}_{si}^k \nabla S_{ip} + (\sum_i \mathbf{v}_{li}^k \nabla S_{ip})^T] - \beta_s \Delta T_p^k \mathbf{I}$.
- 9: Update particle volume: $V_p^{k+1} = V_p^k [1 + tr(\Delta \boldsymbol{\varepsilon}_p^k)]$.
- 10: Update particle porosity: $n_{lp}^{k+1} = 1 - n_{sp}^k / [1 + tr(\Delta \boldsymbol{\varepsilon}_p^k)]$.
- 11: Update particle density: $\rho_{\pi p}^{k+1} = \rho_{\pi p}^k / (1 + \beta_s \Delta T_p^k)$.
- 12: Update particle liquid saturation S_{lp}^{k+1} and permeability $k_{rp}^{k+1}, k_{ap}^{k+1}$: Equations (25)–(27).
- 13: Update particle volume fraction: $n_{\pi p}^{k+1} = V_p^{k+1} S_{lp}^{k+1}$.
- 14: Compute effective stress: $\boldsymbol{\sigma}_p^{k+1} = \boldsymbol{\sigma}_p^k + \mathbf{D} : \Delta \boldsymbol{\varepsilon}_p^{k+1} + \boldsymbol{\sigma}'_p \cdot \Delta \boldsymbol{\omega}_{sp}^{k+1} - \Delta \boldsymbol{\omega}_{sp}^{k+1} \cdot \boldsymbol{\sigma}'_p$.
- 15: Assemble nodal matrix and arrays: Equations (A1)–(A14), (66)–(67).
- 16: Compute nodal temperature rate T_j^{k+1} : Equation (60).
- 17: Compute nodal intermediate velocities $\mathbf{v}_{\pi j}^*$: Equation (61).
- 18: Compute nodal incremental pore pressure Δp_j^{k+1} : Equation (62).
- 19: Compute end-of-step nodal velocities $\mathbf{v}_{\pi j}^{k+1}$: Equation (63).
- 20: Update particle velocities, pore pressure, and temperature:

$$\psi_p^{k+1} = \psi_p^k + \sum_i \Delta \psi_i^{k+1} S_{ip}, \quad \psi = \mathbf{v}_{\pi}, p_i, T$$
- 21: Update particle position: $\Delta \mathbf{x}_p^{k+1} = \Delta t (\mathbf{v}_{sp}^k + \frac{1}{2} \sum_i \Delta \mathbf{v}_{si}^{k+1} S_{ip})$.
- 22: $t = t + \Delta t$.
- 23: **end while**

TABLE 1 Mechanical and thermal properties of ice and liquid water.

Parameter	Description	Value	Unit
ρ_l	Intrinsic density of liquid (at 0°C)	1000	kg/m ³
ρ_c	Intrinsic density of ice (at 0°C)	920 ^[1,2] , 917 ^[3–6]	kg/m ³
K_l	Liquid compressibility	1×10^{-8} ^[1,2] , 1×10^{-9} ^[3–6]	1/Pa
c_l	Specific heat capacity of liquid	4182 ^[1,2] , 4200 ^[3–6]	J/(kg · °C)
c_c	Specific heat capacity of ice	2060	J/(kg · °C)
β_l	Thermal expansivity of liquid	2.1×10^{-4}	1/°C
β_c	Thermal expansivity of ice	1.53×10^{-4}	1/°C
κ_l	Thermal conductivity of liquid	0.6	W/(m · °C)
κ_c	Thermal conductivity of ice	2.14 ^[1,2] , 2.2 ^[3–6]	W/(m · °C)
L_f	Latent heat of fusion	3.34×10^5	J/kg

Note: Subscripts [1]–[6] indicate the value used for numerical examples in Sections 5.1.1–5.3.2, respectively.

through an intercomparison of simulation results from 13 different codes. The example simulates the melting of an initially frozen inclusion located within a saturated porous medium that is subjected to warm water flow. Following Grenier et al.,³⁶ we neglect the density-driven convection, porosity change, and mechanical response caused by either thermal expansion or phase transition, and adopt the same SFCC and hydraulic conductivity models in their work, as shown in Appendix B.1.

Figure 2 illustrates the model setup of the problem. The modeling domain is a rectangular area with dimensions of 3 m × 1 m. An initially frozen inclusion with a square shape and dimensions of 0.33 m is located along the central axis

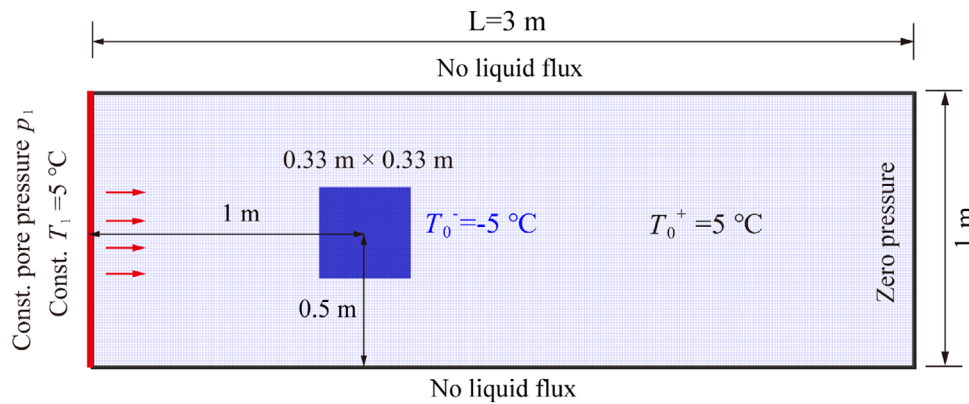


FIGURE 2 Model setup for the simulation of frozen inclusion thaw.

TABLE 2 Summary of cases in the frozen inclusion thaw and Talik closure/opening examples.

ID	ex1: frozen inclusion thaw			ex2: Talik closure/opening		
	∇h	p_1 [Pa]	T_1 [°C]	∇h	p_1 [Pa]	T_1 [°C]
Case 1	0%	0	5	0%	0	5
Case 2	3%	882.9	5	3%	882.9	5
Case 3	9%	2648.7	5	9%	2648.7	5

of the domain, with its center 1 m away from the left boundary. The initial temperature of the frozen inclusion (T_0^-) is -5°C , while the surrounding temperature (T_0^+) is 5°C . The left surface is exposed to a constant temperature of 5°C and a constant pore pressure p_1 , while the right surface is a zero-pressure boundary. Three cases with different p_1 are conducted: (1) Case 1: 0 Pa, (2) Case 2: 882.9 Pa, and (3) Case 3: 2648.7 Pa, corresponding to the 0, 3, and 9% pressure head gradient ($\nabla h = h/L$) cases in Grenier et al.'s study,³⁶ as shown in Table 2. Here, $h = p_1/\rho_l g$ is the pressure head, L is the length from the upgradient side to the downgradient side, equaling 3 m, and g is the gravitational acceleration (9.81 m/s^2). Case 1 represents a pure heat conduction problem, whereas the other two cases involve convective heat transfer triggered by the liquid flow. Since no mechanical response is expected in this example, we impose zero velocity on the solid phase. Additionally, the liquid fluxes at the top and bottom surfaces are set to zero to ensure no flow through the two boundaries.

The soil properties used are given as follows³⁶: $\phi = 0.37$, $k_0 = 1.3 \times 10^{-10} \text{ m/s}$, $\rho_s = 2650 \text{ kg/m}^3$, $c_s = 835 \text{ J/(kg} \cdot ^\circ\text{C)}$, and $\kappa_s = 9 \text{ W/(m} \cdot ^\circ\text{C)}$. A convergence study is first conducted to investigate the influence of mesh size and the number of particles per cell (ppc) on the numerical results. Quadrilateral cell with uniform size is adopted in all cases. Detailed information on the test cases is presented in Section B.2. Figure B1 shows that using a finer background mesh can help improve the accuracy of the results while increasing the particle number per cell does not work effectively. Although using a finer mesh can help achieve closer results to the actual solutions, this may dramatically increase the computational cost. Hence, a mesh size of 0.01 mm and four ppc are adopted as the default setting for the reset simulations, considering a trade-off between accuracy and efficiency.

Figure 3 shows the temperature and pressure head contour ($\nabla h = 3\%$) at $t = 22,860 \text{ s}$ for Case 2. The chosen time is before the threshold time at which the frozen inclusion completely melts and around which extremely nonlinear spatial distributions of temperature are observed (see Figure 3D). At the associated time, the frozen inclusion becomes rounder in shape and warmer compared to its initial temperature. Figure 3B,D shows that our simulated temperature is almost identical to the results using the FVM code Cast3M.³⁶ Figure 3A,C shows that the head fields in the unfrozen region are consistent for both results, while minor discrepancies are observed within the frozen region which may arise from the low permeability of the frozen inclusion. Since most of the water is frozen, there is nearly no liquid flow and, thus, no convective heat transfer in this region. Therefore, the discrepancy shows no evident influence on the temperature evolution.

Figure 4 shows the temperature plume on the horizontal axis for Case 1 ($\nabla h = 0\%$) and Case 3 ($\nabla h = 9\%$) in this study in comparison with the reference study. In Case 1, the temperature distribution starts symmetrically but later becomes asymmetric due to geometric asymmetry. In contrast, the temperature distribution in Case 3 turns asymmetric immediately once the fluid fields have formed and carried warmer water downstream. The close similarity between our results and

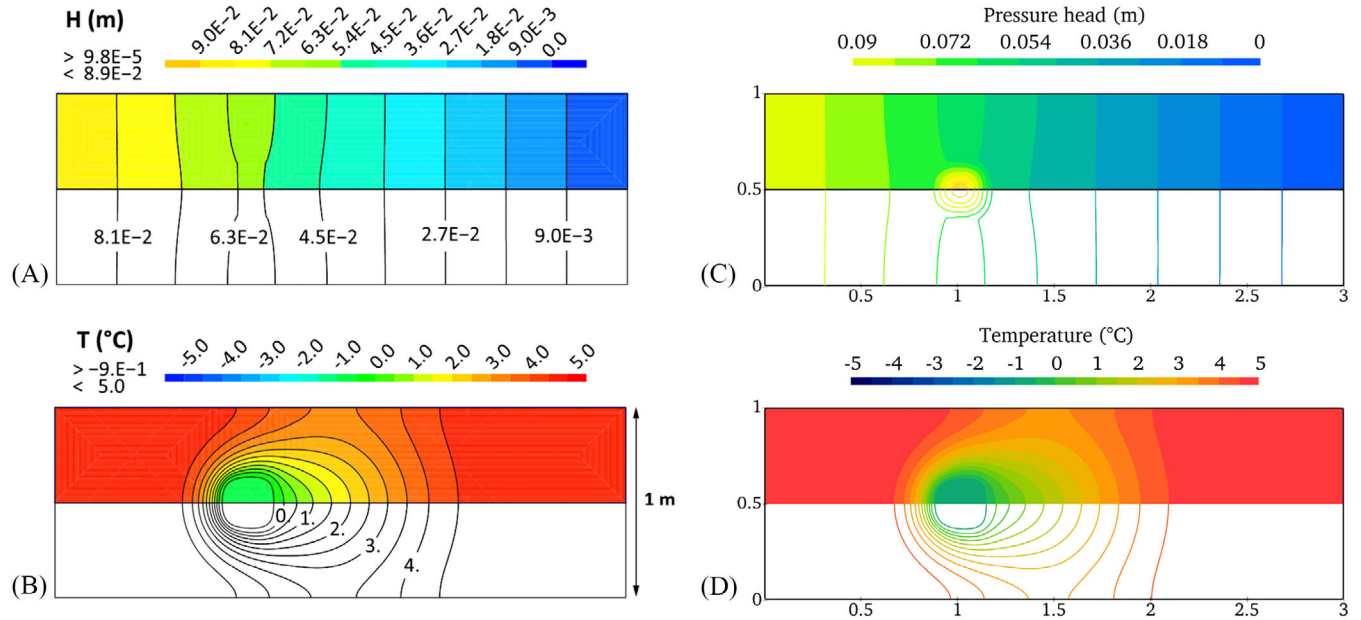


FIGURE 3 Contours of pressure and temperature from the literature³⁶ (left column) and this work (right column) in Case 2 ($\nabla h = 3\%$) at $t = 22,860$ s.

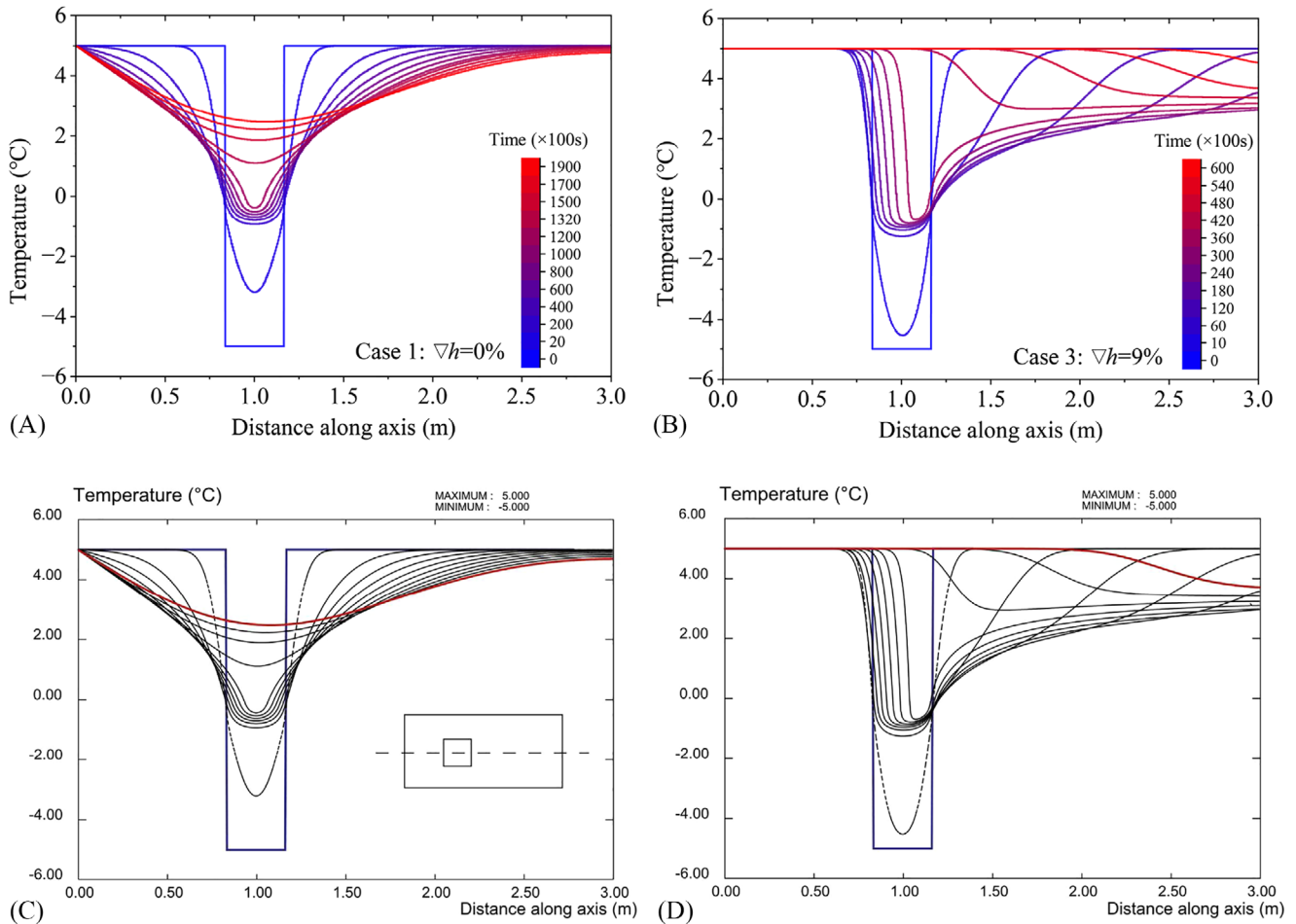


FIGURE 4 Contours of pressure and temperature from this work (top row) and the literature³⁶ (bottom row) in Case 2 ($\nabla h = 3\%$) at $t = 22,860$ s.

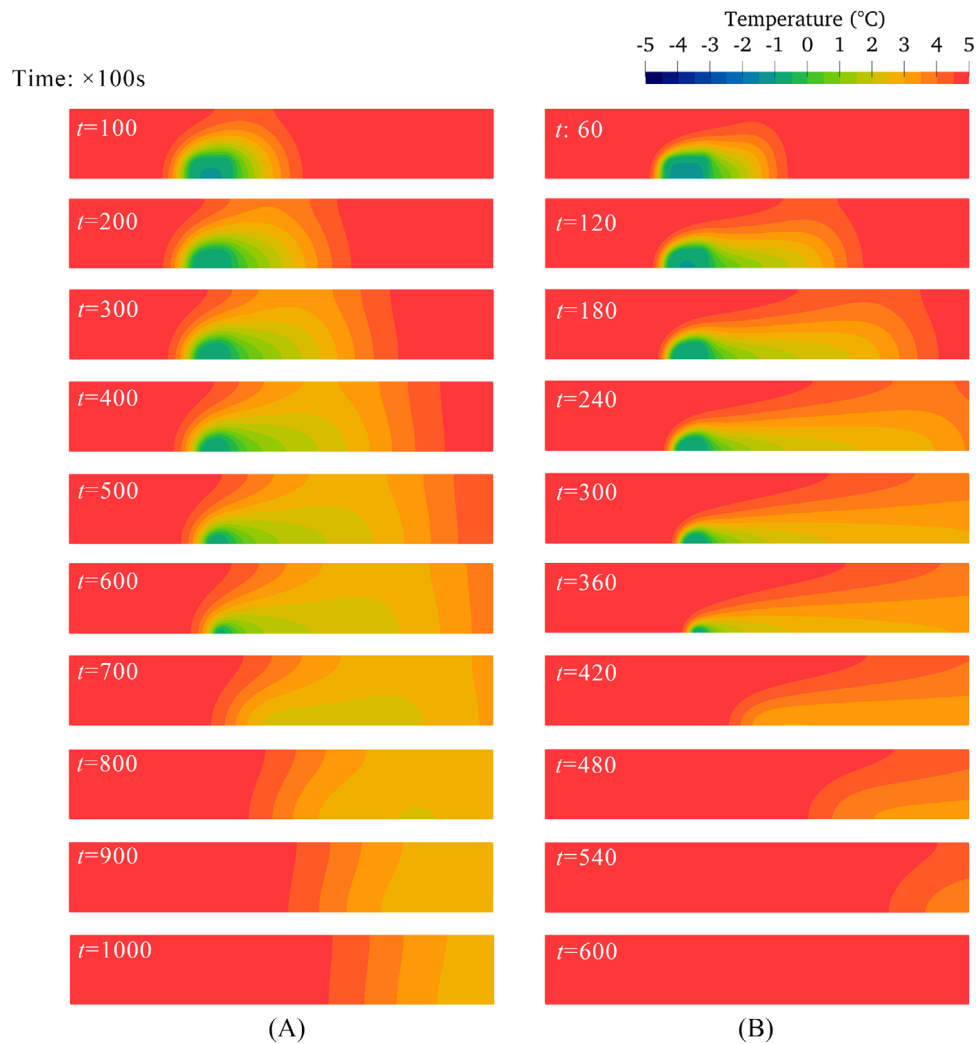


FIGURE 5 Contours of temperature in (A) Case 2 ($\nabla h = 3\%$) and (B) Case 3 ($\nabla h = 9\%$).

the reference study validates our numerical methods. Notably, the frozen region in Case 3 melts much faster than that in Case 1. The former approaches a nearly uniform temperature at 5°C after 60,000 s, while the minimum temperature in the latter case remains below 3°C after 190,000 s. This indicates that liquid flow may significantly influence the temperature evolution and the phase balance in frozen porous media. Figure 5 further illustrates contours at different time frames for cases with 3 and 9% head gradients. The high-gradient case exhibits faster heat transfers and longer temperature plumes, highlighting the considerable effect of liquid flow and heat convection in frozen groundwater systems.

5.1.2 | Talik closure/opening

The second example presents a different boundary value problem by imposing both rising and decreasing temperature boundaries simultaneously. This example, referred to as “Talik closure/opening,” has a layer of soil or sediment in permafrost that remains unfrozen, usually serving as underground seepage channels. It is designed to study the closure or opening of Talik during permafrost freezing and thawing.³⁶ The model setup of the problem is illustrated in Figure 6. Two semi-circular frozen regions with an initial negative temperature (T_0^-) of -5°C are located symmetrically in the bottom and upper half of a 1-m^2 domain, with the middle area initially unfrozen at a temperature (T_0^+) of 5°C . The left boundary is prescribed with a constant positive temperature of 5°C , while the bottom and upper boundary are prescribed with a constant negative temperature of -5°C . Similarly, three cases with $\nabla h = 0\%$ (Case 1), 3% (Case 2), and 9% (Case 3) are conducted, as shown in Table 2. The corresponding boundary pressure p_1 are 0, 294.3, and 882.9 Pa, respectively. The material properties are identical to the previous example.

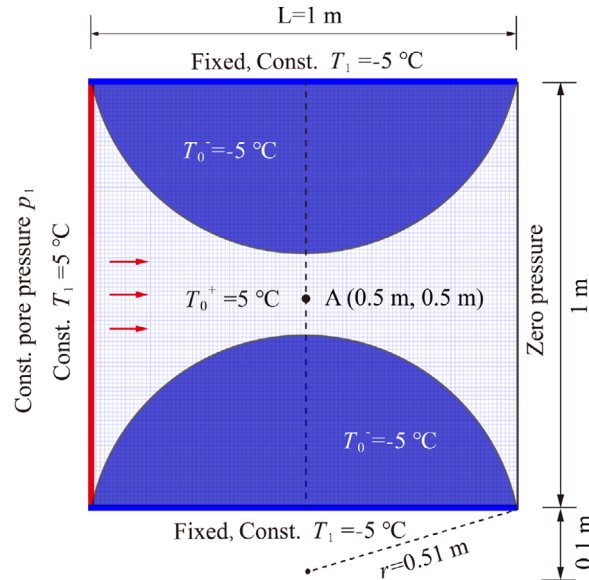


FIGURE 6 Model setup for the Talik closure/opening problem.

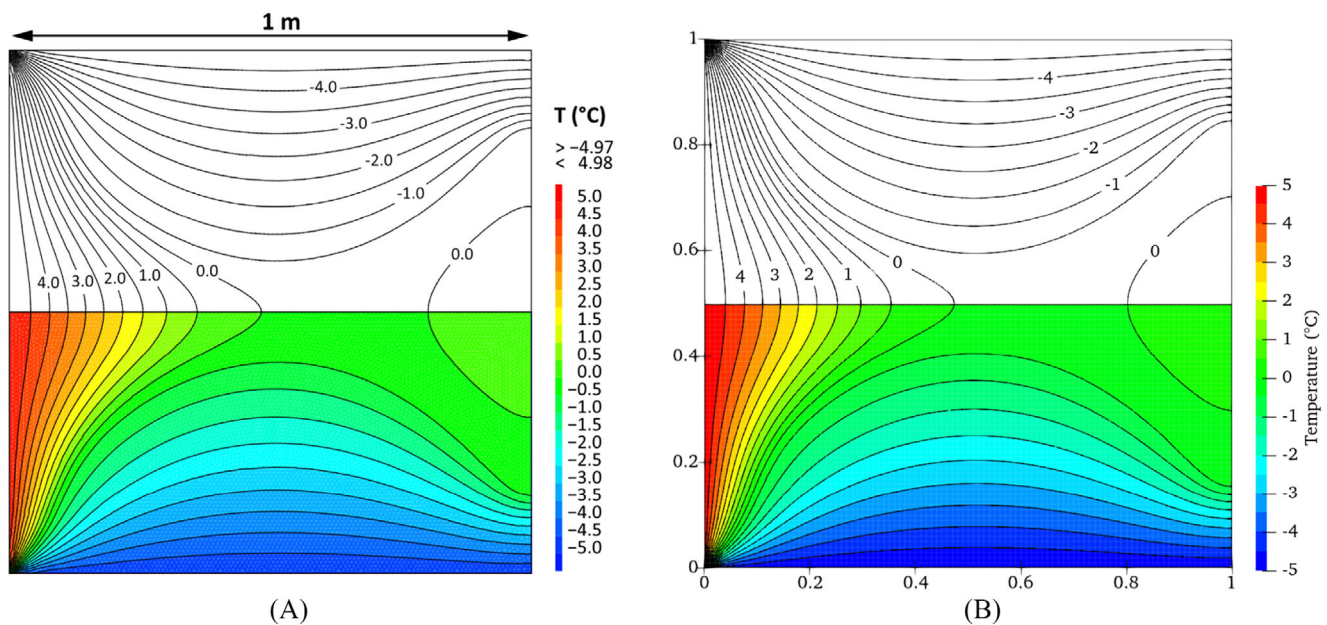


FIGURE 7 Contours for temperature field in Case 2 ($\nabla h = 3\%$) at $t = 19,900$ s. The left subfigure (A) shows the simulation results obtained in Ref. 36 using the FVM code Cast3M, while the right subfigure (B) shows the solution obtained in this study using coupled MPM.

Figure 7 presents a comparison of the temperature contour of Case 2 at $t = 19,900$ s between our prediction and the reference study. The contour lines for MPM in Figure 7B are almost identical to those in Figure 7A, suggesting the accuracy of the presented method in capturing the thermal-hydraulic responses in complex freeze–thaw systems. Figure 8 further shows a quantitative comparison of the temperature along the vertical axis in both studies. For both Cases 1 and 3, our simulated temperature has identical evolution patterns and comparable magnitudes with the referenced results. It is also observed from Figure 7 that the minimum temperature at the center of the domain is below 0°C , indicating the Talik has been closing at the associated time. This phenomenon implies that the seepage channel can be obstructed by the formation of ice under relatively low gradient flow conditions. More contour results for all three cases at different time instants are shown in Figure 9. For Case 1, which represents a scenario of pure heat conduction, the temperature within the Talik rapidly drops below the freezing point, resulting in the merging of the two frozen semicircular regions. The

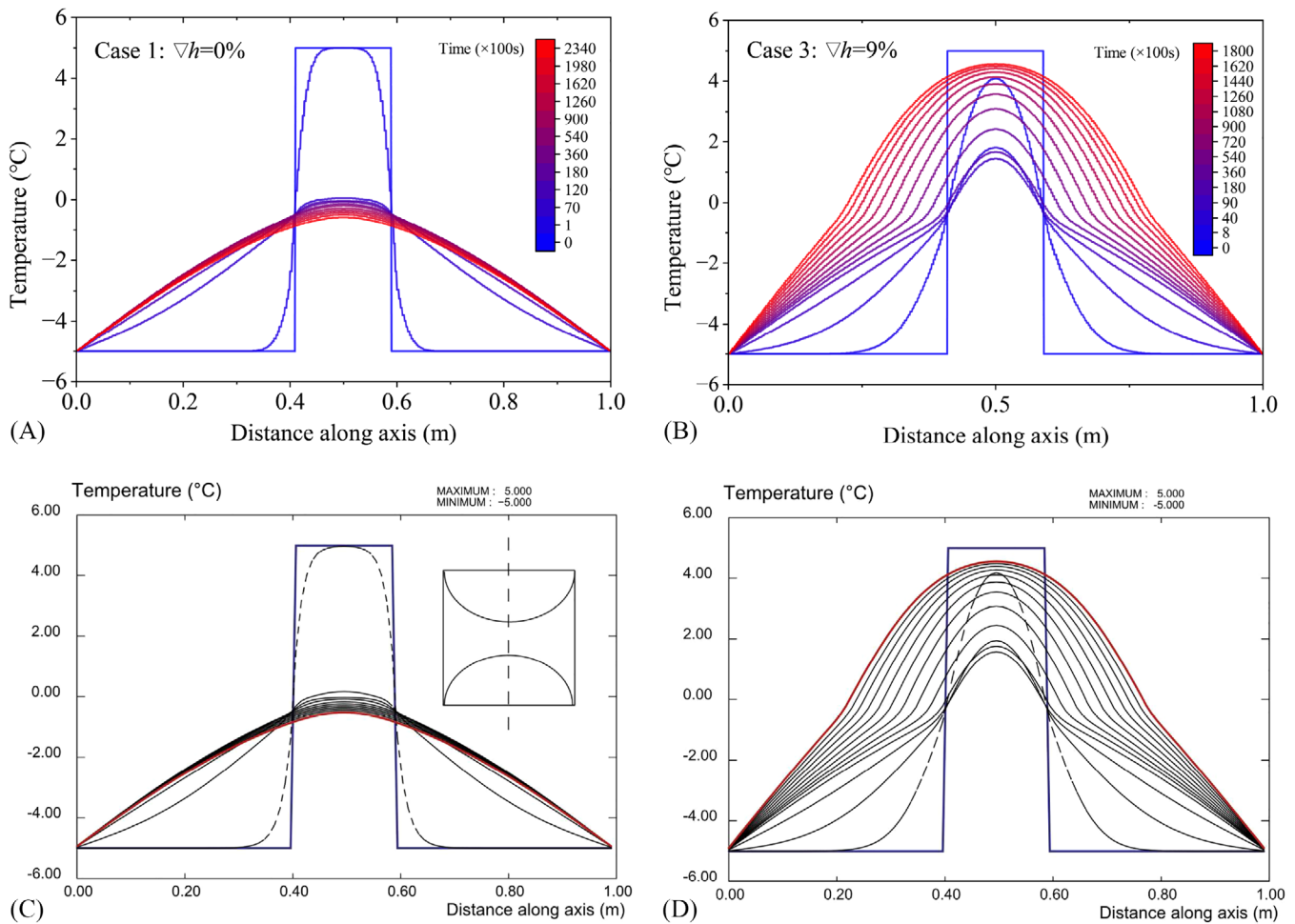


FIGURE 8 Temperature along the vertical central axis for this study (top row) and Ref. 36 (bottom row). The left two subfigures (A) and (C) correspond to Case 1 ($\nabla h = 0\%$), and the right two (B) and (D) correspond to Case 3 ($\nabla h = 9\%$).

closure of the Talik is attributed to the conductive heat loss caused by the frozen temperature boundaries. In contrast, for Case 3, the cooling effect due to conductive heat loss in the Talik is progressively hindered by the warmer flow from the left heating boundary. Consequently, convective heat transfer eventually becomes dominant, leading to the widening of the Talik zone. The closure or opening of the Talik is greatly influenced by the intensity of the convective heat transfer, which is controlled by the flow rate. In this case, the pressure head gradient of 3% provides an insufficient flow rate to resist the connection of frozen regions, as previously analyzed. This example showcases the important role of heat convection and its combined effects with heat conduction in shaping the morphology of permafrost.

5.1.3 | Code performance

To further evaluate the code performance, additional global indexes for the two examples are investigated and compared with the results in Ref. 36

- (1) For the frozen inclusion thaw example, two indexes, the global minimum temperature (T_{min}) and the total volume of liquid within the domain (V_l^{total}), are examined. The evolution of these two performance measures is shown in Figure 10. Consistent trends and magnitude are observed between our MPM results and the results from other codes.* Notably, the typical stepwise feature of these curves is replicated. Based on T_{min} , we can divide the entire frozen inclusion thaw process into three stages. (I) When $T_{min} < -1^\circ\text{C}$, the inner areas of the frozen inclusion become warmer

* Results from other codes can be found on the INTERFROST PROJECT website: <https://wiki.lsce.ipsl.fr/interfrost/doku.php>.

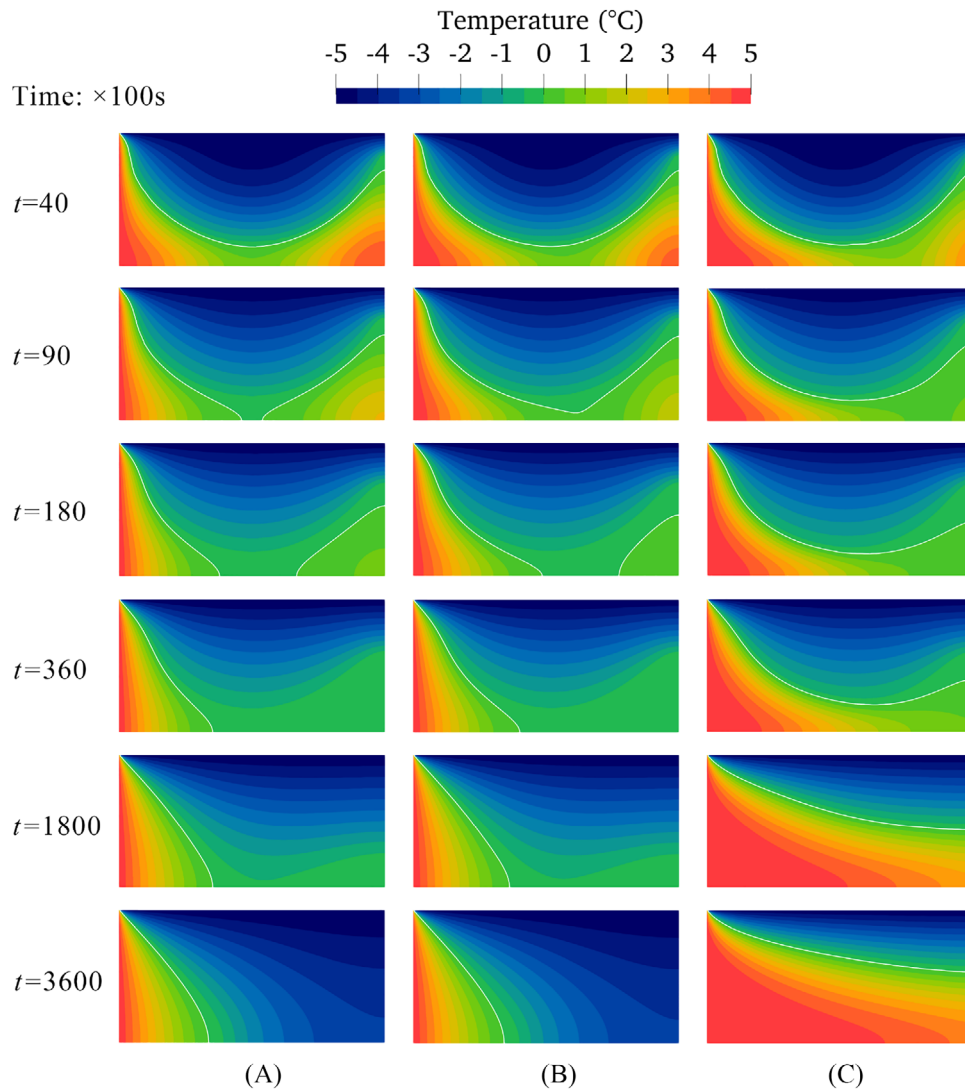


FIGURE 9 Contours of temperature in (A) Case 1 ($Vh = 0\%$), (B) Case 2 ($Vh = 3\%$), and (C) Case 3 ($Vh = 9\%$).

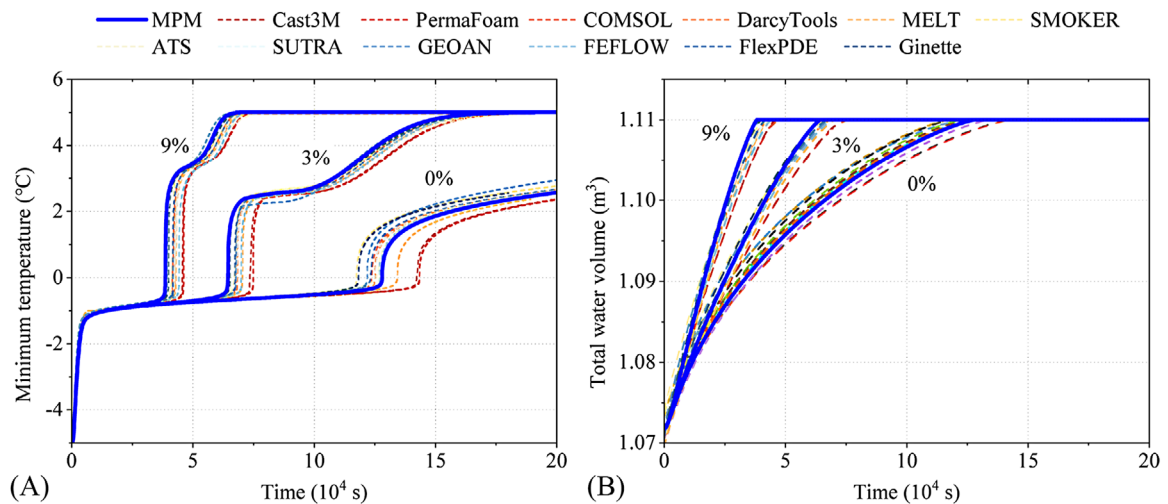


FIGURE 10 Performance measures for the frozen inclusion thaw example (A) Global minimum temperature and (B) total liquid water volume.

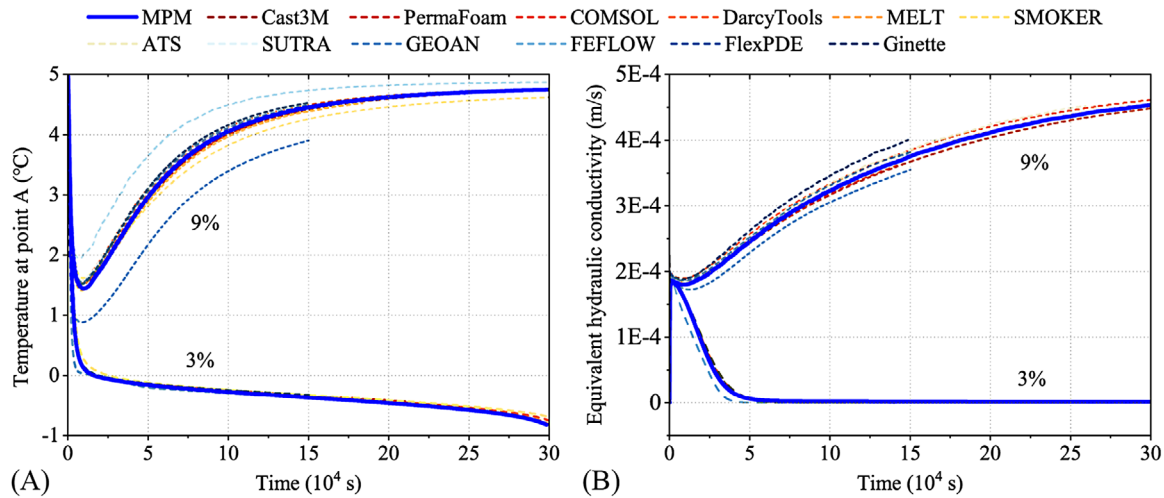


FIGURE 11 Performance measures for the Talik example. (A) Temperature at the center of the problem domain and (B) equivalent hydraulic conductivity for Case 2 ($\nabla h = 3\%$) and Case 3 ($\nabla h = 9\%$).

through conductive heat transfer from the unfrozen area. This period only maintains a very short period for all three cases. (II) When $-1^\circ\text{C} < T_{min} < 0^\circ\text{C}$, phase transition mainly happens in this stage. Due to the latent heat effect, the temperature in the frozen inclusion increases at a very low rate, especially for Case 1, which has no connective heat transfer. (III) When $T_{min} > 0^\circ\text{C}$, the residual cool temperature plume after the complete melting of the frozen inclusion is gradually transported downgradient until a uniform temperature is achieved. This figure clearly demonstrates the role of the latent heat effect during phase transition and further highlights the influence of convective heat transfer on temperature evolution.

- (2) For the Talik closure/opening example, another two global indexes, the temperature evolution at the central Point A (0.5 and 0.5 m), and the equivalent hydraulic conductivity k_{eq} are investigated. $k_{eq} = \int_{\partial\Omega_o} n_i v_i \cdot \mathbf{n} dS / \int_{\partial\Omega_o} n_i dS$ is defined as the integrated Darcy flux at the outlet boundary divided by the imposed head gradient, in which $\partial\Omega_{out}$ represents the outlet flow boundary, namely, the right boundary in this example. Figure 11 presents the two indexes alongside the results obtained from other 13 codes. Good agreements with the simulation results from other codes are found for both indexes. The obvious differences between the two presented cases clearly illustrate the characteristics of Talik closure or opening. Figure 11A shows that the center temperature in the low-gradient case rapidly falls below zero, whereas that in the high-gradient case initially decreases and then increases but always remains above the freezing point. The changing trend in the latter case signifies the transition of the heat transfer mechanism from conductive to convective dominance and the transformation of the porous system from a frozen state to a thawing state. Figure 11B shows that the equivalent hydraulic conductivity for the low-gradient case gradually decreases to zero, indicating that the seepage channel is blocked by ice. Conversely, the equivalent hydraulic conductivity for the high-gradient case displays an overall increasing trend, reflecting the opening or widening of the Talik.

The two examples suggest that the proposed method can effectively and accurately capture critical characteristics during freezing and thawing processes in a hydrological and thermal coupled porous system. It is worth mentioning that the CPU times are approximately 35 min for the frozen inclusion thaw example with 20,000 steps and 25 min for the Talik closure/opening example with 60,000 steps when using a desktop with an Intel Core™ i7-11700, indicating a relatively good run time performance. This provides a solid foundation for the subsequent thermal-hydro-mechanical analysis of porous media involving phase transition.

5.2 | Verification of THM-coupled MPM

5.2.1 | 1D thawing consolidation

Thaw settlement is a typical mechanical response of frozen soil subjected to temperature rise. In this example, we simulate the thawing consolidation of frozen ground, aiming to validate the performance of the THM-coupled MPM in dealing with

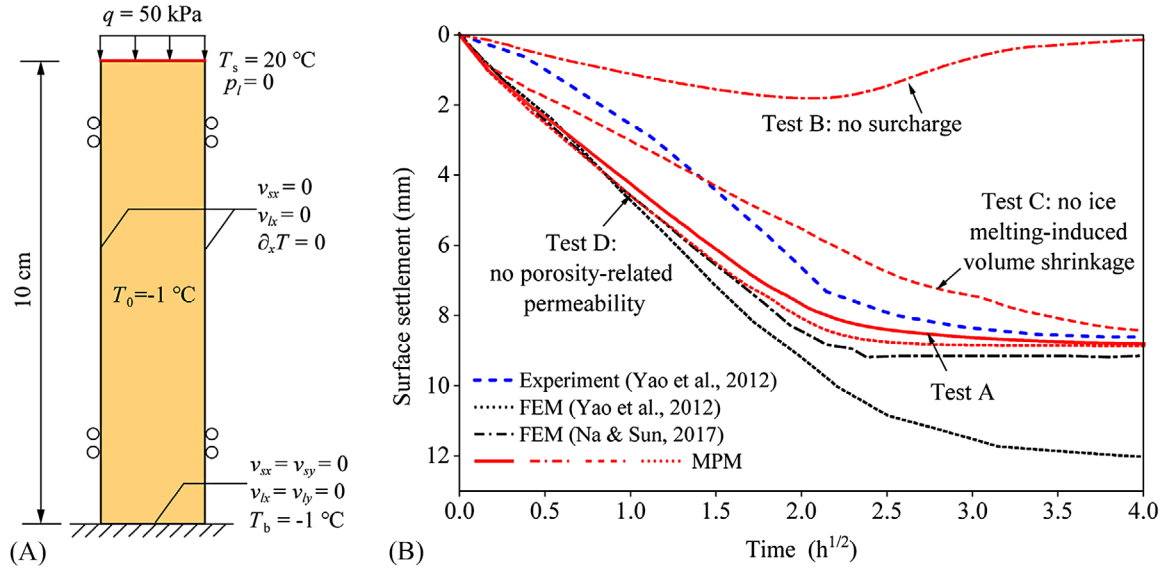


FIGURE 12 (A) Model setup for the thawing consolidation of a frozen ground and (B) surface settlement over time.

thermal-hydro-mechanical coupled problems. The soil sample is a 10 cm by 10 cm cylinder subjected to nonisothermal confined compression. The problem can be simplified as a 1D consolidation problem, with the geometry and test conditions illustrated in Figure 12A. To ensure 1D deformation, the bottom boundary is fixed, and the left and right boundaries allow vertical deformation only. The top surface is a zero-pressure boundary, while the other boundaries are zero-flux boundaries. The initial temperature of the soil sample is -1°C . During the simulation, the top surface is subjected to a constant temperature T_s of 20°C and a uniformly distributed surcharge q of 50 kPa simultaneously. The bottom is kept at -1°C , and the lateral sides are insulated. Following Yao et al.,¹³² the thaw settlement is assumed to be in the elastic range, and the thermal strain is neglected. The mechanical and thermal parameters are given as follows: $E = 400 \text{ kPa}$, $\nu = 0.3$, $\phi = 0.4$ (at -1°C), $\rho_s = 2750 \text{ kg/m}^3$, $c_s = 720 \text{ J/(kg} \cdot ^\circ\text{C)}$, $\kappa_s = 1.6 \text{ W/(m} \cdot ^\circ\text{C)}$, and $k_0 = 7 \times 10^{-9} \text{ m/s}$ (at 0°C). The material constants in the SFCC (Equation 25) and relative permeability model (Equation 27) are set as: $\lambda = 0.5$, $p_0 = 100 \text{ kPa}$, and $m = 0.5$. The initial domain is discretized into 50 cells with a cell size of 0.2 cm.

The reference case is labeled as Test A. Three additional cases are carried out to show the effect of different factors on the hydro-mechanical response during thaw consolidation. In Test B, the surface surcharge is removed while the surface temperature keeps unchanged. In Test C, the term $\zeta D_s n_c / Dt$ in the mass balance equation (see Equation 6), which represents the effect of phase transition on the volumetric change, is not activated. In Test D, the porosity-dependent permeability (Equation 27) is not considered. Figure 12B compares the ground settlement in this study and previous studies. Overall, the result of the reference case Test A is in good agreement with the experiment data. In this experiment, the accumulation of thaw settlement results from the combined effect of frozen soil melting and surface surcharge. For natural permafrost, even without surface surcharge, the soil may still subside during thawing. This behavior is successfully captured in Test B. To better explain the behavior of frozen soil during melting, we further plot the spatial distribution of pore water pressure for Tests A–C at different time instances in Figure 13A and the relationships between pore pressure, ice saturation, and permeability with regard to soil depth for Test A in Figure 13B.

In Tests A and C, the maximum pore pressures are about 50 kPa, equal to the surface surcharge. The pore pressure distribution curves show a noticeable turning point that almost coincides with the thaw front, as evidenced in Figure 13B. Above the turning point, the pore pressure dissipates much faster than that below because the permeability of the upper-layer melted soil is several-order higher than that of the unmelt soil. In test C, which involves temperature rise only, the excess pore pressure is negative with a peak shifting along with the thaw front. The negative pressure results from volume shrinkage (about 9%) due to ice melting, and it generates compression stress on the soil skeleton, leading to the settlement of the soil. Existing laboratory tests have also observed negative pore pressure during the thaw settlement of frozen soils.^{133,134} However, since the simulation employs an ideal elastic model, the soil returns to its original state as the pore pressure dissipates (an elastic–plastic model may reduce the recovery). Without accounting for the effect in Test C, the rate of pore pressure dissipation and settlement is underestimated compared to Test A. Additionally, by comparing Case 1 and Case 4, neglecting the porosity-dependent permeability changes may result in an overestimation of the settlement

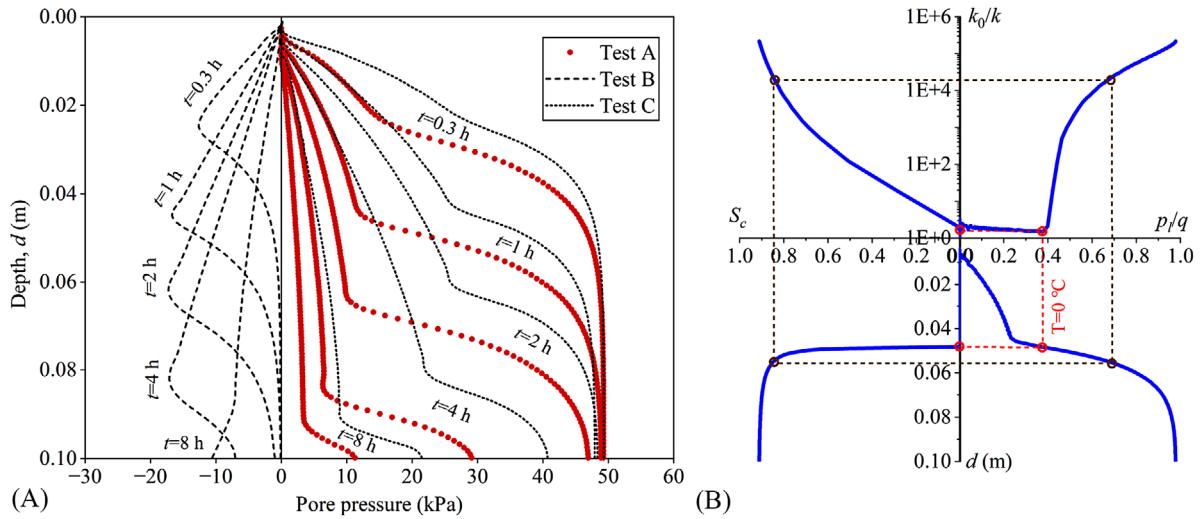
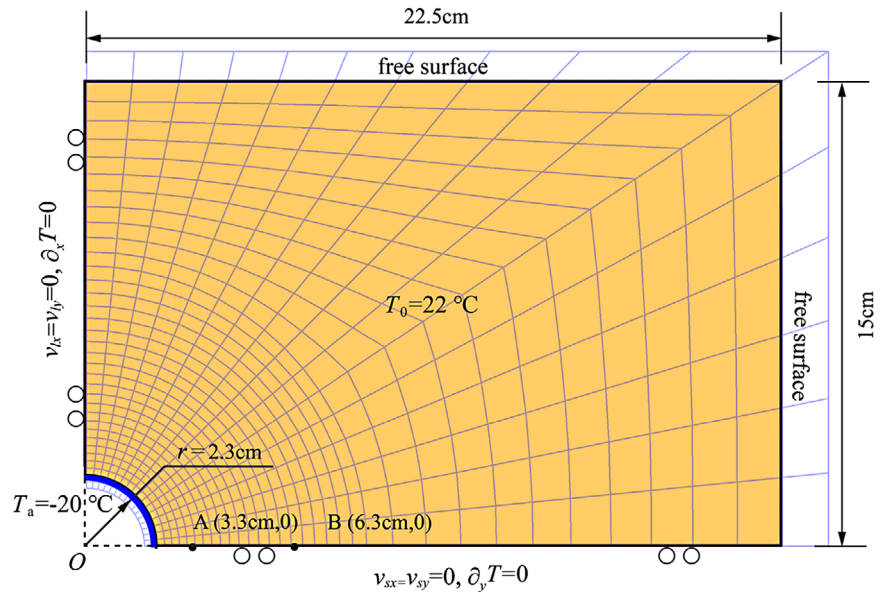


FIGURE 13 (A) Pore pressure distribution along with depth in Tests A–C. (B) Relationships of normalized pore pressure p_l/q , ice saturation S_c , reciprocal of normalized permeability k_0/k , and soil depth d at $t = 1$ h in Test A, in which the red dash lines indicate where the thaw front propagates to.

FIGURE 14 Model setup for the simulation of an initially unfrozen rock subjected to freezing from the hole surface.



rate. Thaw settlement is a rather complex phenomenon influenced by various factors, including material properties, temperature variations, ice contents, soil permeability, and external loads. The proposed framework can capture the major essential characteristics during soil melting with fairly good simulation results.

5.2.2 | 2D freezing problem

The experiment of rock freezing²⁵ is used as the benchmark. In this experiment, a saturated rock sample of $45 \times 30 \times 15$ cm ($L \times W \times H$) with a cylindrical hole of 4.6 cm at its center was tested. A brine circulation through the cylindrical hole with a constant temperature of -20°C was used as the cooling source. The sample was confined within a thermostat box to ensure the adiabatic condition. The temperature and axial strain were measured at points A and B, 1 and 4 m to the hole surface, respectively. Considering the geometric symmetry, we use one-fourth of the domain in the simulation and simplify the problem as a 2D plane strain problem. Figure 14 illustrates the model setup of the problem. The initial temperature of the rock sample is 22°C . The heat transfer coefficient between the hole surface and the cooling water

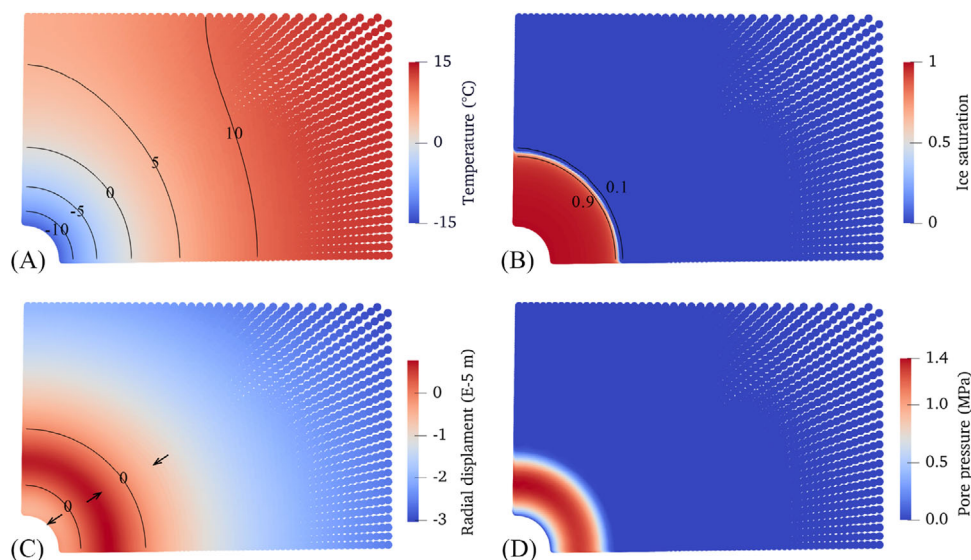


FIGURE 15 Contours of (A) temperature T , (B) ice saturation S_i , (C) radial displacement u_r , and (D) pore water pressure p_i at 10 h.

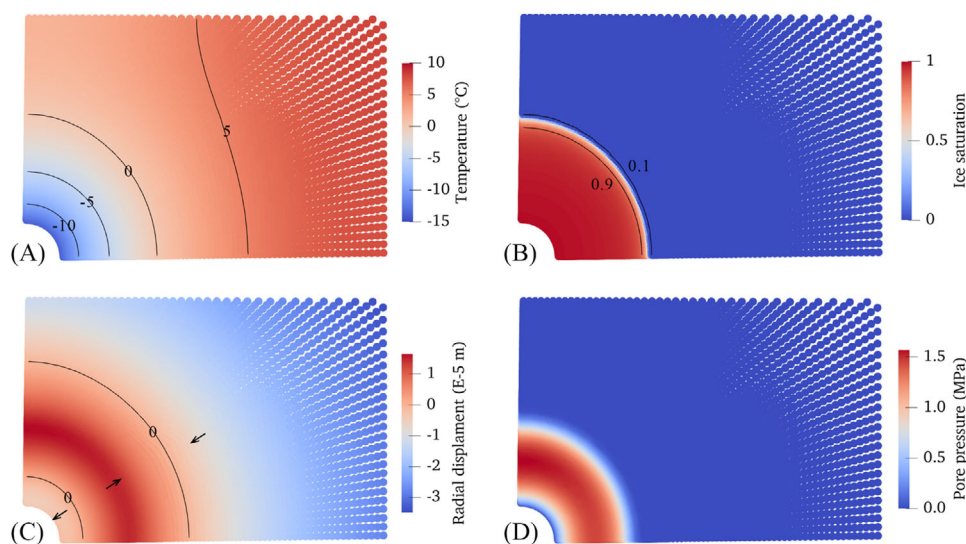


FIGURE 16 Contours of (A) temperature T , (B) ice saturation S_i , (C) radial displacement u_r , and (D) pore water pressure p_i at 15 h.

is $100 \text{ W}/(\text{m}^2 \cdot \text{C})$. The isoperimetric cell is adopted to improve the results when using unstructured cells.¹³⁵ The linear elastic model is used with mechanical and thermal parameters given as follows: $E = 1 \text{ GPa}$, $\nu = 0.25$, $\phi_0 = 0.224$ (at 22°C), $\rho_s = 1830 \text{ kg}/\text{m}^3$, $c_s = 816 \text{ J}/(\text{kg} \cdot ^\circ\text{C})$, $\beta_s = 2.7 \times 10^{-5}/^\circ\text{C}$, $\kappa_s = 1.046 \text{ W}/(\text{m} \cdot ^\circ\text{C})$, and $k_0 = 1 \times 10^{-7} \text{ m/s}$ (at 0°C). The parameters in the SFCC and the relative permeability model are set as: $\lambda = m = 0.5$ and $p_0 = 100 \text{ kPa}$.

Figures 15 and 16 show the contours of temperature, ice saturation, radial displacement, and pore pressure at $t = 10$ and 15 h , respectively. During cooling, the freezing front (0°C contour line) propagates to the far end, which is identified by a very narrow and clear mushy zone (i.e., liquid–ice mixed region) near the freezing front in the ice saturation contour. The narrow mushy zone is probably owing to the utilization of a steep SFCC. Figure 17A,B compares the simulated temperature and experimental results at Points A and B. Numerical results using FEM by Refs. 25, 78 are presented for comparison. It can be seen that our simulated temperature is in good agreement with the experimental one. A noteworthy phenomenon is that, due to the latent heat effect, the temperature drop slows down gradually when phase transition occurs below the freezing point. The radial displacement field (Figures 15C and 16C) shows how the rock sample deforms during freezing. The contour map is separated into three regions by two zero displacement lines, where the intermediate region undergoes

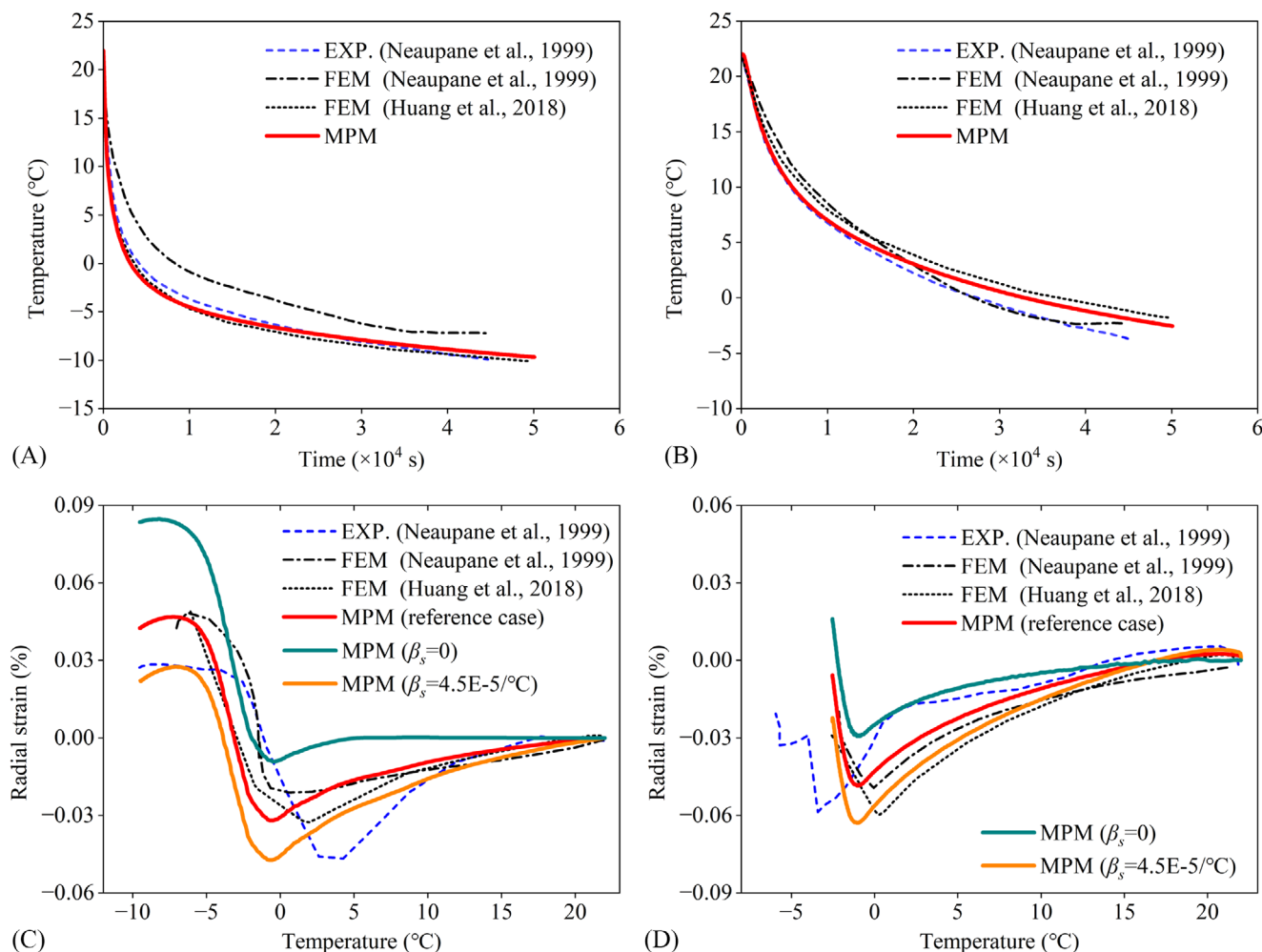


FIGURE 17 Comparison of results in these study and previous work: (A) temperatures at point A, (B) temperatures at point B, (C) radial strain at point A, and (D) radial strain at point B.

deformation away from the hole center while the remaining parts move toward the hole center. This is attributed to a combined effect of thermal contraction and frost heave.

Figure 17A,B plots the radial strain at Points A and B. A turning point is observed at around 0°C , above which the axial strain is negative and below which the axial strain turns in the opposite direction. The initial negative strain is attributed to dual factors: the thermal contraction due to temperature drop and the extrusion of already frozen material points. To illustrate the explanation, we simulate another two cases. The first one neglects the thermal contraction by setting $\beta_s = 0$, and the second one uses a larger thermal expansivity $\beta_s = 4.5 \times 10^{-5}/^\circ\text{C}$. The simulation results are plotted in Figure 17C,D for comparison. It is found that without considering thermal contraction, the rock still contracts at the initial stage, but the magnitude becomes smaller. By contrast, if a larger thermal expansivity is considered, the magnitude of thermal contraction increases. When the frozen front reaches the associated material point, the contraction-dominated deformation changes gradually to the frost-heave-dominated mode, and, therefore, the axial strain goes from the negative to the positive direction. The simulated heave strain is approximately the same amount as that of the experiment. Similar to the thaw settlement, the frost heave is also caused by the volumetric changes during the liquid–ice phase transition. The volumetric expansion generates a large pore pressure, as shown in Figures 15D and 16D, which further induces a tensile force on the solid phase, causing the heaving of rock.

Figure 18 plots the relations of pore pressure, liquid saturation, and permeability along the radial direction of the rock sample, to further explain how the positive pore pressure generates and impacts the rock deformation. When the temperature drops below 0°C , the liquid water content drops rapidly, and the rock permeability, which is almost linearly related to the liquid saturation in log–log space, also drops rapidly. Extremely low permeability makes the unfrozen water in the rock almost lose mobility, causing a buildup of pore water pressure and frost heave force. Besides, numerical tests show that the

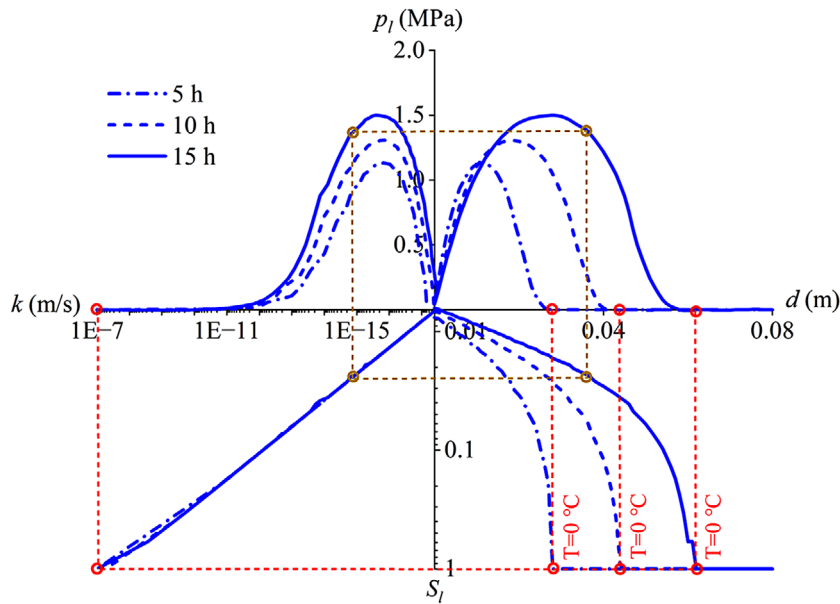


FIGURE 18 Relationship of pore pressure p_l , liquid saturation S_l , hydraulic conductivity k , and radial distance to the borehole surface d at three time instances: $d = 5, 10, 15$ h. The red dash lines from left to right represent where the thaw front (i.e., $T = 0^\circ\text{C}$) propagates to at the three time instances, respectively.

rate and accumulated magnitude of heave strain are, to some degree, related to the SFCC and permeability model. A more accurate SFCC and permeability model may help improve the fidelity of the simulation. In nature, frost heave is more complex and can be influenced by some other factors, such as the ice–liquid interface suction, premelting effect, capillarity, and underground water migration, which can be further implemented into the current framework in future studies. But, overall, the proposed framework can provide reasonable numerical results for freezing- and thawing-related problems.

5.3 | THM-coupled large deformation problems

5.3.1 | Thaw slump

With global warming, RTS occurs more frequently in permafrost when an ice-rich section thaws.¹³⁶ RTS develops quickly and can extend across several hectares, modifying landscapes significantly.¹¹ However, it is nontrivial to physically or numerically model the behavior of RTS. A noteworthy work by Harris et al.¹³⁴ investigated the periglacial slope stability in relation to soil properties by centrifuge tests. The experimental results of Test 6 in their work are employed to benchmark our proposed computational framework.

The geometric setup of the simulated slope is illustrated in Figure 19. The initial temperature of the slope is -10°C , while the ground temperature is maintained at 10°C during the thawing process. The base of the slope is fixed, and the two vertical side boundaries are rollers. Following the centrifuge test, the gravity is set as 10 g, that is, 98.1 m/s^2 . The material properties are selected as follows: $E = 20\text{ MPa}$, $\nu = 0.3$, $\phi_0 = 0.4$ (at 0°C), $\rho_s = 2650\text{ kg/m}^3$, $c_s = 837\text{ J/(kg}\cdot^\circ\text{C)}$, $\kappa_s = 1.0\text{ W/(m}\cdot^\circ\text{C)}$, and $k_0 = 1.5 \times 10^{-10}\text{ m/s}$ (at 0°C). The SFCC and relative permeability models are set as: $\lambda = m = 0.4$ and $P_0 = 100\text{ kPa}$. The thermal conductivity and permeability are scaled by 86,400 s/day. The strength parameters for unfrozen soil are set as: $c'_p = 2\text{ kPa}$ and $\phi'_p = 20^\circ$. The strain-softening behavior is not considered. The additional strength for frozen soil due to ice cementation is specified as follows: $\Delta c_{max} = 200\text{ kPa}$, $\Delta\phi_{max} = 15^\circ$, and $\eta_c = 0.05$. The maximum additional cohesion Δc_{max} is estimated based on the experimental data (see fig. 1 in Ref. 86 for cohesion values of frozen soil at different temperatures). The background mesh size is 0.035 m, and the timestep size is $5 \times 10^{-5}\text{ s}$. The initial stress field is generated by gravitational force.

Figures 20–22 present the simulated temperature, displacement, and deviatoric strain at $t = 20$ days. The failure configuration and the failure surface observed in the experiment conducted by Harris et al.¹³⁴ are also plotted in the corresponding figures for comparison. The thaw front and the failure surface locate approximately 0.1 m above the slope base, indicating that the reduced shear strength resulting from ice melting is the primary trigger for the slope failure. The displacement reveals that the melted soil exhibits fluid-like behavior as the thaw front continues to progress downward. Good agreements for the post-failure morphology and the sliding surface are observed between the predicted results by our computational framework and the experimental results. Note that due to the limited material parameters provided by

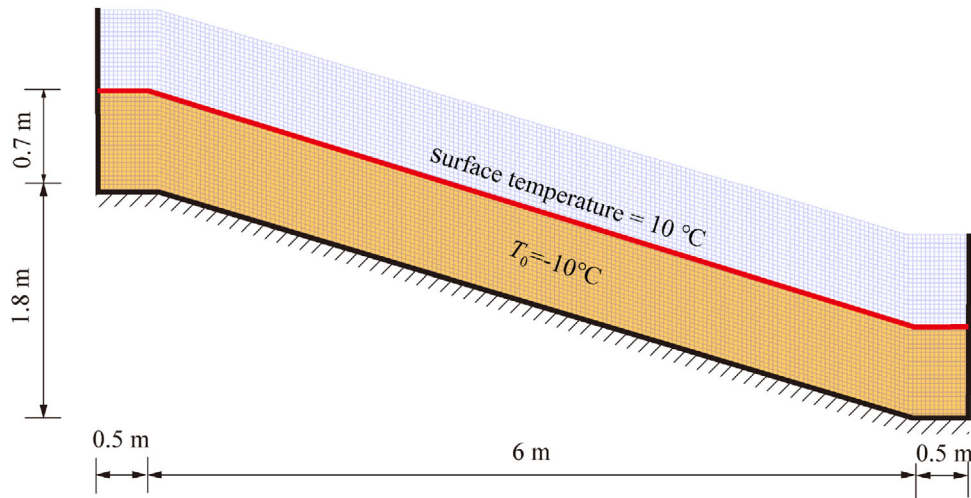


FIGURE 19 Model setup for the simulation of thawing slump.

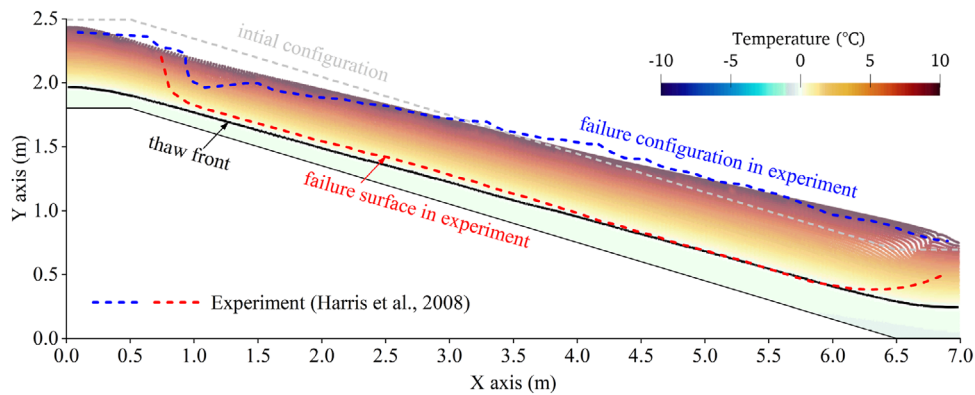


FIGURE 20 Contour of temperature field at the elapsed time of 20 days.

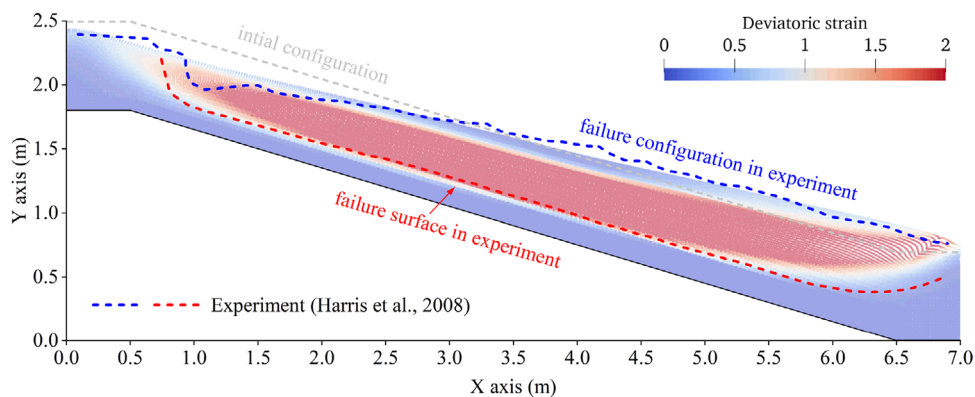


FIGURE 21 Contour of deviatoric strain at the elapsed time of 20 days.

the experiment, it is difficult to assess certain behaviors, such as the softening and dilation of soils, resulting in some discrepancies between the simulation and the experiment. For example, a narrower shear band and a longer mobilization distance of soil mass are observed in the experiment as compared to the simulation. However, overall, the proposed method can reasonably capture major behaviors of thawing slumps.

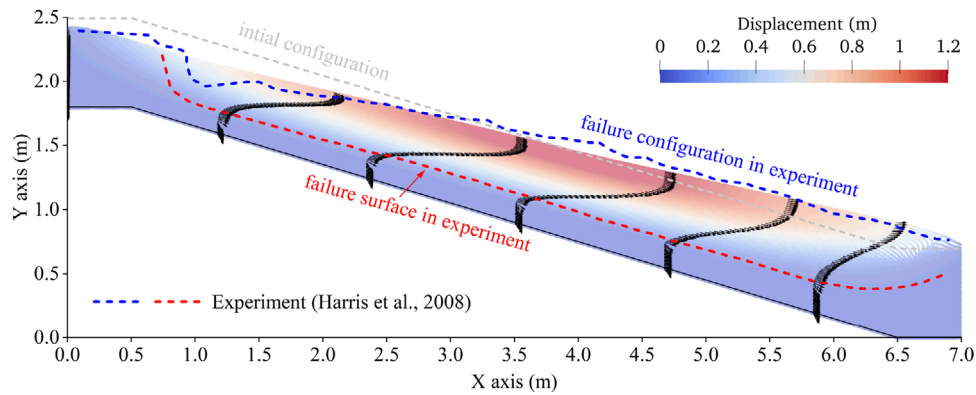


FIGURE 22 Contour of displacement field at the elapsed time of 20 days. The black arrows are displacement vectors of deformed material points that are initially parallel to the Y-axis.

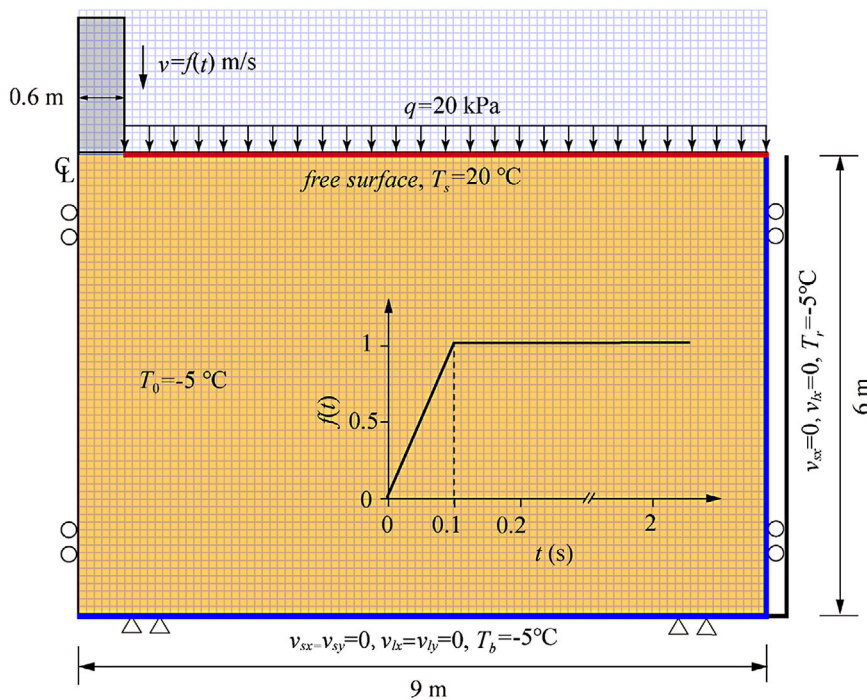


FIGURE 23 Model setup for the simulation of a strip footing resting on a thawing frozen ground and subjected to settlement.

5.3.2 | Mechanical response of a strip footing on thawing ground

The bearing capacity of frozen soil may decrease when the frozen soil is melting, leading to excessive or differential settlement of foundations. The settlement during permafrost thaw is related to not only the volumetric contraction during ice melting and meltwater drainage but also the strength reduction due to the loss of ice cementation. In this example, we simulate the THM response of a rigid strip footing resting on a thawing ground and subjected to settlement using the ice saturation-dependent Mohr–Coulomb model presented in Section 3.3.

The model configuration is depicted in Figure 23. The simulated soil domain has dimensions of 18 m in width and 6 m in depth. The bottom boundary is fixed, while the axial boundaries are constrained in the horizontal direction only. The initial temperature of the soil is -5°C . The strip footing, with a width (B) of 1.2 m, is placed at the center of the ground surface. The strip footing is assumed to be rigid and rough. The penetration velocity of the strip footing increases gradually from zero to a constant value. The remaining portion of the top surface is subjected to a surcharge load of 20 kPa and a uniform temperature rise of 20°C simultaneously. Other boundaries except the top surface are fixed at -5°C . As the primary focus of this example is on the coupled response resulting from the loss of cohesion in thawing soil, the effects of gravity and thermal expansivity are not considered. Due to geometric symmetry, only half of the domain is modeled.

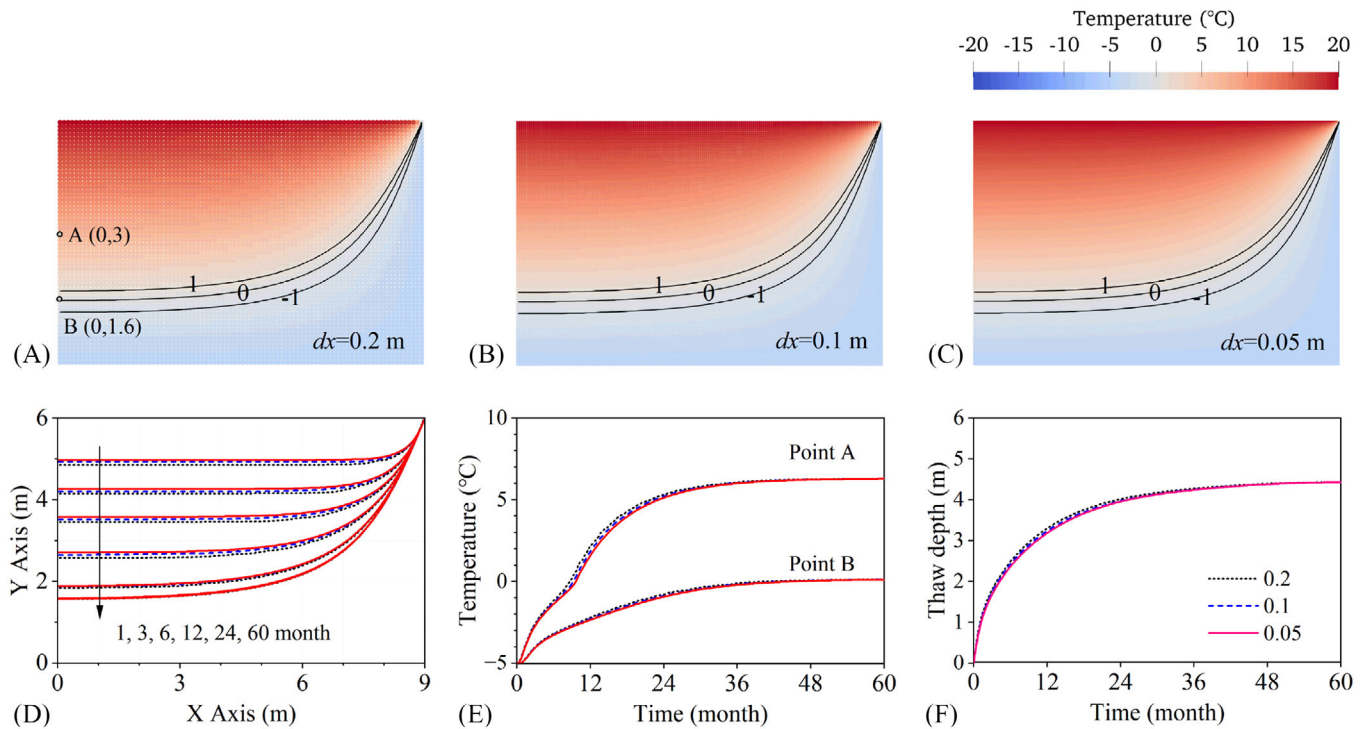


FIGURE 24 Temperature contour after 60 months for mesh size of (A) 0.2 m, (B) 0.1 m, and (C) 0.05 m; (D) thaw front line evolution; (E) temperature at point A (0 and 3 m) and B (0 and 1.6 m); and (F) thaw depth over time.

The material properties are set as follows: $E = 100$ MPa, $\nu = 0.3$, $\phi_0 = 0.4$ (at 0°C), $\rho_s = 2650$ kg/m³, $c_s = 837$ J/(kg \cdot $^\circ\text{C}$), $\kappa_s = 2.1$ W/(m \cdot $^\circ\text{C}$), and $k_0 = 1 \times 10^{-10}$ m/s (at 0°C). In addition, the parameters used in SFCC and relative permeability models are set as: $\lambda = m = 0.4$ and $p_0 = 100$ kPa. The strength parameters for unfrozen soil are set as: $c'_p = 20$ kPa, $c'_{res} = 10$ kPa, $\varphi'_p = 30^\circ$, $\varphi'_{res} = 30^\circ$, $\psi'_p = 0^\circ$, and $\eta_s = 5$. The additional strength for frozen soil due to ice cementation is specified as follows: $\Delta c_{max} = 200$ kPa, $\Delta\varphi_{max} = 0^\circ$, and $\eta_c = 0.05$.

The mesh sensitivity of heat transfer and the thawing rate are first assessed using three different mesh sizes of 0.05, 0.1, and 0.2 m, with each mesh cell initiated with four material points. In the preliminary test, all mechanical loads are removed, and the hydro-mechanical solver is not activated since the focus is simply on heat transfer. The timestep is set as 8640 s. Figure 24A–C shows the final steady-state temperature contours with the lines of -1 , 0 , and 1°C being highlighted. The temperature distributions among the three mesh fineness cases exhibit negligible discrepancies. Figure 24D–F compares the thawing front lines at different time intervals, the temperature evolution of Point A (0 and 3 m) and B (0 and 1.4 m), and the central thaw depth over time. The results for the three tests basically overlap with each other. The mesh size of 0.1 m can provide sufficient accuracy for heat transfer and is thus employed for subsequent THM-coupled analysis. Furthermore, it is important to note that the rate of heat transfer is rather low in soils. It may take several months or even years to reach a steady state. Although a larger timestep can be used for the heat transfer equation, a small timestep remains necessary for global THM coupling because the critical timestep for the momentum equation is small. To accelerate the simulation, the thermal and hydraulic conductivity are scaled by a factor of $250 \times 86,400$ s/day so that the simulation of 1 s represents 250 days in the real world. For THM analysis, the global timestep size is chosen as 1×10^{-4} s. The footing settlement speed is set as 1 m/s. The simulation is terminated until the settlement d equals the width of the footing, namely, $d/B = 1$.

For comparative analysis, we also simulate a case of strip footing on frozen ground without thawing. Figures 25 and 26 compare the THM response in the unthawed case (left) and the thawing case (right) with a normalized settlement (d/B) of 0.5 and 1, respectively. The temperature contour lines of 0 and -1°C are displayed on the contour figures for reference. The large deformation of the foundation causes changes to the distribution of the temperature field. A noticeable change is that the thaw front below the rigid footing moves downward. The subsidence of the footing causes shear failure of the surrounding soil, with the plastic regions extending to the ground surface, leading to surface heave near the footing.

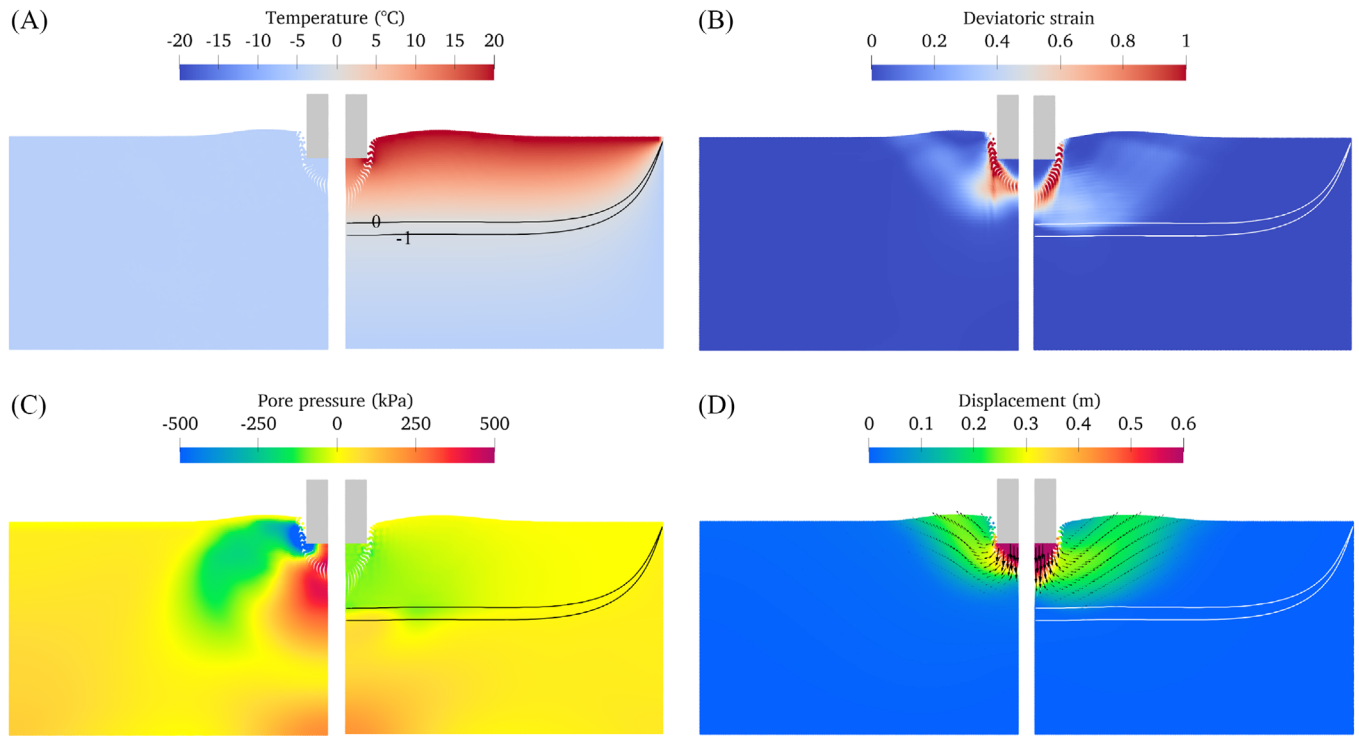


FIGURE 25 Contour results of (A) temperature, (B) deviatoric strain, (C) pore pressure, and (D) displacement for the unfrozen case (left) and the thawing case (right) when the normalized settlement $d/B = 0.5$.

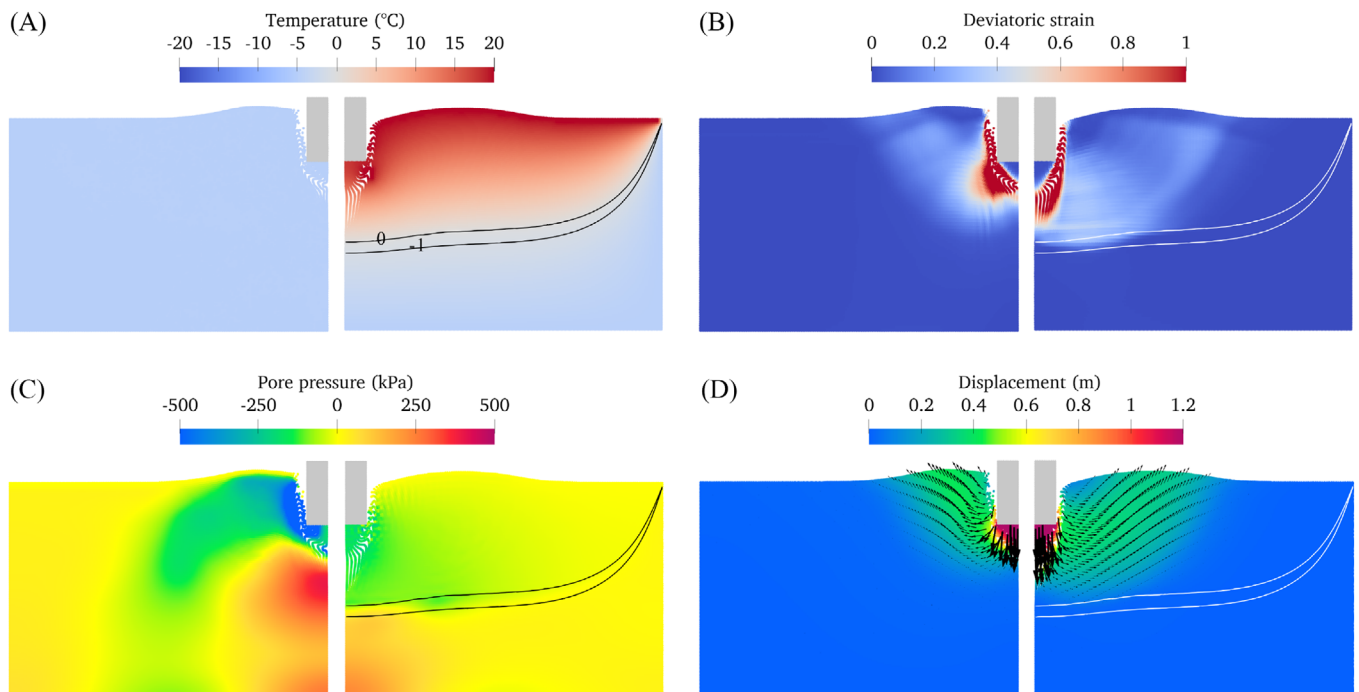


FIGURE 26 Contour results of (A) temperature, (B) deviatoric strain, (C) pore pressure, and (D) displacement for the unfrozen case (left) and the thawing case (right) when the normalized settlement $d/B = 1$.

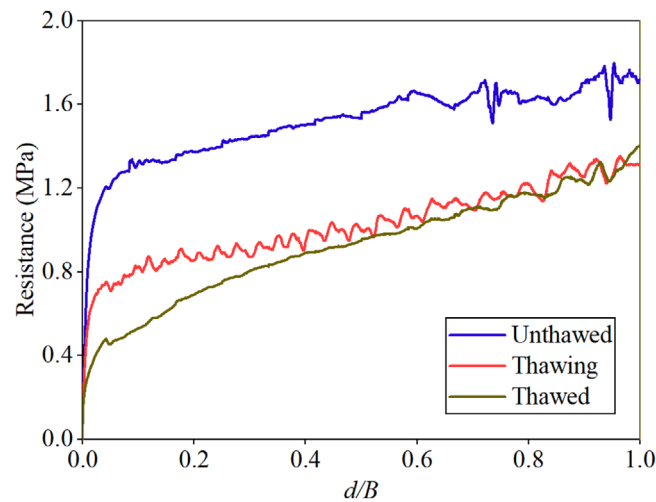


FIGURE 27 Resistance versus normalized settlement d/B .

However, it is observed that the plastic zone of the thawing foundation is larger and deeper than that of the unthawed foundation. The angle of the wedge beneath the footing in the thawing case is also larger than that of the unthawed one. In addition, the bottom of the plastic zone is located approximately along the thaw front (between the 0 and -1°C contour lines). This indicates that the loss of cohesion makes the whole thawed region more susceptible to shear failure, and the frozen–unfrozen interface tends to become the weak plane where the plastic strain accumulates. As a result of the loss of cohesion, the bearing capacity of the thawing foundation experiences a significant reduction compared to the unthawed foundation, as shown in Figure 27. We further conducted a test in which the strip footing is placed on a thawed foundation, namely, the initial temperature field of the foundation is as shown in Figure 24. The bearing capacity for the thawed foundation is even lower than the thawing case, as indicated by the green line in Figure 27, further indicating the significant influence of ice melting on the bearing capacity of the foundation. In addition, clear discrepancies are observed in the pore pressure distribution between both cases. In the unthawed case, the rapid soil settlement leads to high pore pressure. Since the permeability of frozen soil is extremely low, the excess pore pressure dissipates very slowly. However, in the thawing case, the magnitude of permeability of upper melted soil is several orders higher than the frozen soil; thus, the pore pressure for the upper dissipates very fast, while the beneath frozen soil shows similarity with the unthawed case. Additionally, the melting of ice generates a negative pore pressure, which neutralizes the positive pore pressure induced by footing settlement.

The shear failure pattern and the bearing capacity may be influenced by the consolidation rate and the thawing rate of the soil. Hence, we simulate four more cases with different settlement rates of 2, 1, 0.5, and 0.25 m/s, while the material parameters keep consistent. To observe the performance under extremely large deformation, we simulate all cases until the settlement reaches 1.5 times the width of the footing. Figure 28 shows the deviatoric strain at different settlements in all four tests. The temperature contour lines of 0°C (upper) and -1°C (lower) are also highlighted. It is observed that the bottom of the shear surface always overlaps with the thaw front line, regardless of the loading rate. With the thaw front moving, the shear failure zone moves downward along with the thaw front, forming fan-shaped shear bands. The shear failure occurs largely in the upper thawed region, while the lower unthawed soil is almost intact. For the fast loading rate case ($v = 2$ and 1 m/s), the thawing process has not reached the steady state when the simulation is terminated, while for the low loading rate case ($v = 0.5$ and 0.25 m/s), the footing is still moving downward when the thaw front stops moving. For the latter cases, shear strain is accumulated gradually along the final steady-state thaw front. Low loading rate cases tend to yield larger shear failure regions compared to the higher rate ones, while the surface heave of the former is less significant. These results show that the relative rate of loading and thawing can result in discrepancies in failure and soil movement patterns, whereas some similarities also exist. Note that the bearing capacity and the failure of a thawing foundation are influenced by many other factors, which are not fully considered in this model. Above all, this case demonstrates the good performance of the proposed method in simulating thawing-related large deformations.

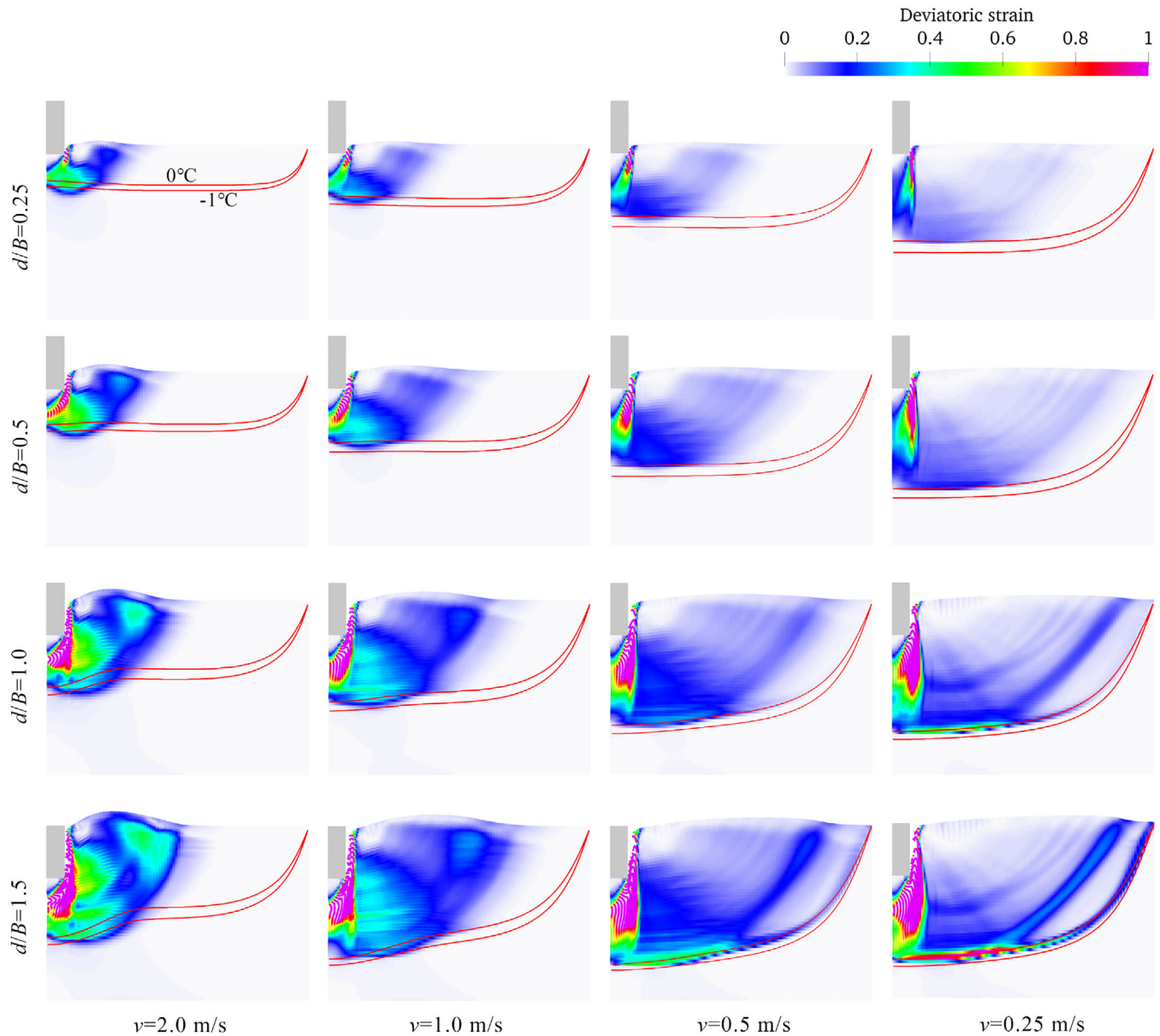


FIGURE 28 Deviatoric strain at different settlement depths in simulations with different loading rates. The red lines are temperature contour lines of 0°C (upper) and -1°C (lower).

6 | CLOSURE

We have presented a THM-coupled MPM framework for modeling phase transition and large deformation behaviors in ice-rich porous media. Major features of the proposed framework include: (a) a fully coupled $\mathbf{v}_s - \mathbf{v}_l - p - T$ governing equation to describe the interactions of heat transfer, pore-liquid flow, and solid deformation based on one-point three-phase MPM; (b) a SFCC and relative hydraulic conductivity model to describe the phase equilibrium and the influence of ice saturation on permeability; (c) a modified Mohr–Coulomb model to characterize the effect of ice cementation on soil strength; and (d) a fractional-step semi-implicit integration algorithm to solve the coupled formulations, which has been proven to achieve both satisfactory numerical stability and computational efficiency when dealing with nearly incompressible fluids and extremely low permeability conditions in frozen porous media. The presented framework is validated by two TH-coupled examples: frozen inclusion thaw and Talik closure/opening, and by two THM-coupled examples: thawing consolidation and rock freezing. These examples show that the framework can effectively simulate (i) the heat transfer due to conduction, convection, and latent heat of fusion, (ii) the volumetric changes due to liquid–ice

phase transition, thermal expansion/contraction, solid deformation, and liquid flow, and (iii) the permeability change due to porosity changes. Finally, we simulated thawing-induced slope failure and the large settlement of a strip footing placed on a thawing ground to showcase the significant influence of strength reduction during ice melting on the stability, bearing capacity, and failure pattern of frozen structures.

The proposed framework provides a promising framework for coupled THM and large deformation modeling of ice-rich soils in cold regions. It is suitable for modeling the large thaw settlement and frost heave of foundations, freeze–thaw cycles of clayey soils and sands, and RTS due to temperature rise. The framework can also be extended to include the gas phase to simulate unsaturated frozen soil and even gas hydrate-bearing sediments. Proper extensions to include fracture models, such as phase field model and peridynamics,^{137–140} can also expedite the framework for modeling thawing or heave-induced cracking in fractured rocks. Additionally, one can couple the proposed THM-coupled MPM with discrete element method (DEM) or molecular dynamics (MD) method to simulate temperature and stress path-dependent constitutive behaviors for these complicated geomaterials that involve phase transitions, thereby avoiding using phenomenological constitutive models.^{58,62,141,142} Future studies should also investigate different solution schemes (e.g., the sequence for solving different unknowns) and parallel schemes (e.g., GPU-based MPM solver) to further improve the numerical accuracy and computational efficiency.

ACKNOWLEDGMENTS

This work is financially supported by the National Natural Science Foundation of China (Project No. 11972030), Research Grants Council of Hong Kong (GRF #16207319, #16208720, #16211221, #16206322, F-HKUST601/19, CRF #C7082-22G, and TRS #T22-606/23-R), and Hetao Shenzhen-Hong Kong Science and Technology Innovation Cooperation Zone (Project #HZQBKCZYB2020083).

CONFLICT OF INTEREST STATEMENT

The authors declare no conflicts of interest or personal relationships that could have appeared to influence the work reported in this paper.

DATA AVAILABILITY STATEMENT

Data will be made available on request.

ORCID

Jidu Yu  <https://orcid.org/0000-0002-2311-0603>

Jidong Zhao  <https://orcid.org/0000-0002-6344-638X>

Shiwei Zhao  <https://orcid.org/0000-0002-3410-3935>

REFERENCES

- Evans SG, Ge S. Contrasting hydrogeologic responses to warming in permafrost and seasonally frozen ground hillslopes. *Geophys Res Lett.* 2017;44 (4):1803–1813. doi:10.1002/2016GL072009
- Lewkowicz AG, Way RG. Extremes of summer climate trigger thousands of thermokarst landslides in a high Arctic environment. *Nat Commun.* 2019;10 (1):1329. doi:10.1038/s41467-019-09314-7
- Luo J, Niu F, Lin Z, Liu M, Yin G, Gao Z. Inventory and frequency of retrogressive thaw slumps in permafrost region of the Qinghai–Tibet plateau. *Geophys Res Lett.* 2022;49 (23):e2022GL099829. doi:10.1029/2022GL099829
- Magnússon RÍ, Hamm A, Karsanaev SV, et al. Extremely wet summer events enhance permafrost thaw for multiple years in Siberian tundra. *Nat Commun.* 2022;13 (1):1556. doi:10.1038/s41467-022-29248-x
- Schuur EaG, McGuire AD, Schädel C, et al. Climate change and the permafrost carbon feedback. *Nature.* 2015;520 (7546):171–179. doi:10.1038/nature14338
- Wang T, Yang D, Yang Y, et al. Permafrost thawing puts the frozen carbon at risk over the Tibetan plateau. *Sci Adv.* 2020;6 (19):eaaz3513. doi:10.1126/sciadv.aaz3513
- Nitzbon J, Westermann S, Langer M, et al. Fast response of cold ice-rich permafrost in northeast Siberia to a warming climate. *Nat Commun.* 2020;11 (1):2201. doi:10.1038/s41467-020-15725-8
- Ting Z, Li D, East A, et al. Warming-driven erosion and sediment transport in cold regions. *Nat Rev Earth Environ.* 2022;3. doi:10.1038/s43017-022-00362-0
- Li D, Lu X, Walling DE, et al. High mountain asia hydropower systems threatened by climate-driven landscape instability. *Nat Geosci.* 2022;15 (7):520–530. doi:10.1038/s41561-022-00953-y
- Lantuit H, Pollard WH. Fifty years of coastal erosion and retrogressive thaw slump activity on Herschel Island, Southern Beaufort Sea, Yukon Territory, Canada. *Geomorphology.* 2008;95 (1):84–102. doi:10.1016/j.geomorph.2006.07.040

11. Ramage JL, Irrgang AM, Herzs Schuh U, Morgenstern A, Couture N, Lantuit H. Terrain controls on the occurrence of coastal retrogressive thaw slumps along the Yukon Coast, Canada. *J Geophys Res Earth Surf.* 2017;122 (9):1619-1634. doi:10.1002/2017JF004231
12. Wang B, Paudel B, Li H. Behaviour of retrogressive thaw slumps in Northern Canada— three-year monitoring results from 18 sites. *Landslides.* 2016;13 (1):1-8. doi:10.1007/s10346-014-0549-y
13. Costard F, Dupeyrat L, Séjourné A, Bouchard F, Fedorov A, Saint-Bézar B. Retrogressive thaw slumps on ice-rich permafrost under degradation: results from a large-scale laboratory simulation. *Geophys Res Lett.* 2021;48 (1):e2020GL091070. doi:10.1029/2020GL091070
14. Luo J, Niu F, Lin Z, Liu M, Yin G. Recent acceleration of thaw slumping in permafrost terrain of Qinghai-Tibet plateau: an example from the Beiluhe region. *Geomorphology.* 2019;341:79-85. doi:10.1016/j.geomorph.2019.05.020
15. Yang D, Qiu H, Ye B, Liu Y, Zhang J, Zhu Y. Distribution and recurrence of warming-induced retrogressive thaw slumps on the central Qinghai-Tibet plateau. *J Geophys Res Earth Surf.* 2023;128 (8):e2022JF007047. doi:10.1029/2022JF007047
16. Niu F, Luo J, Lin Z, Fang J, Liu M. Thaw-induced slope failures and stability analyses in permafrost regions of the Qinghai-Tibet plateau, China. *Landslides.* 2016;13 (1):55-65. doi:10.1007/s10346-014-0545-2
17. Nicu IC, Lombardo L, Rubensdotter L. Preliminary assessment of thaw slump hazard to Arctic cultural heritage in Nordenskiöld Land, Svalbard. *Landslides.* 2021;18 (8):2935-2947. doi:10.1007/s10346-021-01684-8
18. Painter SL, Moulton JD, Wilson CJ. Modeling challenges for predicting hydrologic response to degrading permafrost. *Hydrogeol J.* 2013;21 (1):221-224. doi:10.1007/s10040-012-0917-4
19. Sun F, Wang G, Zhang L, et al. Multiphysics coupling material point method for modelling frost heave of rock slope. *Comput Geotech.* 2022;148:104793. doi:10.1016/j.compgeo.2022.104793
20. Lewis RW, Schrefler BA. *The Finite Element Method in the Static and Dynamic Deformation and Consolidation of Porous Media.* John Wiley & Sons; 1998.
21. Lai Y, Pei W, Zhang M, Zhou J. Study on theory model of hydro-thermal– mechanical interaction process in saturated freezing silty soil. *Int J Heat Mass Transf.* 2014;78:805-819. doi:10.1016/j.ijheatmasstransfer.2014.07.035
22. Li S, Zhang M, Pei W, Lai Y. Experimental and numerical simulations on heat-water-mechanics interaction mechanism in a freezing soil. *Appl Therm Eng.* 2018;132:209-220. doi:10.1016/j.applthermaleng.2017.12.061
23. Nishimura S, Gens A, Olivella S, Jardine RJ. THM-coupled finite element analysis of frozen soil: formulation and application. *Géotechnique.* 2009;59 (3):159-171. doi:10.1680/geot.2009.59.3.159
24. Zhang Y, Michalowski RL. Thermal-hydro-mechanical analysis of frost heave and thaw settlement. *J Geotech Geoenviron Eng.* 2015;141 (7):04015027. doi:10.1061/(ASCE)GT.1943-5606.0001305
25. Neaupane KM, Yamabe T, Yoshinaka R. Simulation of a fully coupled thermo– hydro– mechanical system in freezing and thawing rock. *Int J Rock Mech Min Sci.* 1999;36 (5):563-580. doi:10.1016/S0148-9062(99)00026-1
26. Kay BD, Groenevelt PH. On the interaction of water and heat transport in frozen and unfrozen soils: I. basic theory; the vapor phase. *Soil Sci Soc Am J.* 1974;38 (3):395-400. doi:10.2136/sssaj1974.03615995003800030011x
27. Kurylyk BL, Watanabe K. The mathematical representation of freezing and thawing processes in variably-saturated, non-deformable soils. *Adv Water Resour.* 2013;60:160-177. doi:10.1016/j.advwatres.2013.07.016
28. Ma W, Zhang L, Yang C. Discussion of the applicability of the generalized Clausius–Clapeyron equation and the frozen fringe process. *Earth Sci Rev.* 2015;142:47-59. doi:10.1016/j.earscirev.2015.01.003
29. McKenzie JM, Voss CI, Siegel DI. Groundwater flow with energy transport and water–ice phase change: numerical simulations, benchmarks, and application to freezing in peat bogs. *Adv Water Resour.* 2007;30 (4):966-983. doi:10.1016/j.advwatres.2006.08.008
30. Ge S, McKenzie J, Voss C, Wu Q. Exchange of groundwater and surface-water mediated by permafrost response to seasonal and long term air temperature variation. *Geophys Res Lett.* 2011;38(14). doi:10.1029/2011GL047911
31. Painter SL. Three-phase numerical model of water migration in partially frozen geological media: model formulation, validation, and applications. *Comput Geosci.* 2011;15 (1):69-85. doi:10.1007/s10596-010-9197-z
32. Grenier C, Régner D, Mouche E, Benabderrahmane H, Costard F, Davy P. Impact of Permafrost development on groundwater flow patterns: a numerical study considering freezing cycles on a two-dimensional vertical cut through a generic river-plain system. *Hydrogeol J.* 2013;21 (1):257. doi:10.1007/s10040-012-0909-4
33. Kurylyk BL, MacQuarrie KTB, McKenzie JM. Climate change impacts on groundwater and soil temperatures in cold and temperate regions: implications, mathematical theory, and emerging simulation tools. *Earth Sci Rev.* 2014;138:313-334. doi:10.1016/j.earscirev.2014.06.006
34. Painter SL, Coon ET, Atchley AL, et al. Integrated surface/subsurface permafrost thermal hydrology: model formulation and proof-of-concept simulations. *Water Resour Res.* 2016;52 (8):6062-6077. doi:10.1002/2015WR018427
35. Sjöberg Y, Coon E, Sannel ABK, et al. Thermal effects of groundwater flow through subarctic fens: a case study based on field observations and numerical modeling. *Water Resour Res.* 2016;52 (3):1591-1606. doi:10.1002/2015WR017571
36. Grenier C, Anbergen H, Bense V, et al. Groundwater flow and heat transport for systems undergoing freeze-thaw: intercomparison of numerical simulators for 2D test cases. *Adv Water Resour.* 2018;114:196-218. doi:10.1016/j.advwatres.2018.02.001
37. Liu Y, Li KQ, Li DQ, Tang XS, Gu SX. Coupled thermal–hydraulic modeling of artificial ground freezing with uncertainties in pipe inclination and thermal conductivity. *Acta Geotechnica.* 2022;17 (1):257-274. doi:10.1007/s11440-021-01221-w
38. Na S, Sun W. Computational thermo-hydro-mechanics for multiphase freezing and thawing porous media in the finite deformation range. *Comput Methods Appl Mech Eng.* 2017;318:667-700. doi:10.1016/j.cma.2017.01.028

39. Sulsky D, Chen Z, Schreyer HL. A particle method for history-dependent materials. *Comput Methods Appl Mech Eng.* 1994;118 (1):179-196. doi:10.1016/0045-7825(94)90112-0
40. Yang Y, Lai Y, Chang X. Laboratory and theoretical investigations on the deformation and strength behaviors of artificial frozen soil. *Cold Reg Sci Technol.* 2010;64 (1):39-45. doi:10.1016/j.coldregions.2010.07.003
41. Li S, Lai Y, Zhang S, Liu D. An improved statistical damage constitutive model for warm frozen clay based on Mohr–Coulomb criterion. *Cold Reg Sci Technol.* 2009;57 (2):154-159. doi:10.1016/j.coldregions.2009.02.010
42. Shastri A, Sánchez M, Gai X, Lee MY, Dewers T. Mechanical behavior of frozen soils: experimental investigation and numerical modeling. *Comput Geotech.* 2021;138:104361. doi:10.1016/j.compgeo.2021.104361
43. Arzanfudi MM, Al-Khoury R. Freezing-thawing of porous media: an extended finite element approach for soil freezing and thawing. *Adv Water Resour.* 2018;119:210-226. doi:10.1016/j.advwatres.2018.07.013
44. Liu H, Maghoul P, Shalaby A, Bahari A. Thermo-hydro-mechanical modeling of frost heave using the theory of poroelasticity for frost-susceptible soils in double-barrel culvert sites. *Transp Geotech.* 2019;20:100251. doi:10.1016/j.trgeo.2019.100251
45. Zhang HW, Wang KP, Chen Z. Material point method for dynamic analysis of saturated porous media under external contact/impact of solid bodies. *Comput Methods Appl Mech Eng.* 2009;198 (17):1456-1472. doi:10.1016/j.cma.2008.12.006
46. Jassim I, Stolle D, Vermeer P. Two-phase dynamic analysis by material point method. *Int J Numer Anal Methods Geomech.* 2013;37 (15):2502-2522. doi:10.1002/nag.2146
47. Yerro A, Alonso E, Pinyol N. Run-out of landslides in brittle soils. *Comput Geotech.* 2016;80:427-439. doi:10.1016/j.compgeo.2016.03.001
48. Bandara S, Soga K. Coupling of soil deformation and pore fluid flow using material point method. *Comput Geotech.* 2015;63:199-214. doi:10.1016/j.compgeo.2014.09.009
49. Ceccato F, Beuth L, Vermeer PA, Simonini P. Two-phase material point method applied to the study of cone penetration. *Comput Geotech.* 2016;80:440-452. doi:10.1016/j.compgeo.2016.03.003
50. Soga K, Alonso E, Yerro A, Kumar K, Bandara S. Trends in large-deformation analysis of landslide mass movements with particular emphasis on the material point method. *Géotechnique.* 2016;66 (3):248-273. doi:10.1680/jgeot.15.LM.005
51. Chen ZP, Zhang X, Sze KY, Kan L, Qiu XM. v-p material point method for weakly compressible problems. *Comput Fluids.* 2018;176:170-181. doi:10.1016/j.compfluid.2018.09.005
52. Zhao Y, Choo J. Stabilized material point methods for coupled large deformation and fluid flow in porous materials. *Comput Methods Appl Mech Eng.* 2020;362:112742. doi:10.1016/j.cma.2019.112742
53. Lei X, He S, Abed A, Chen X, Yang Z, Wu Y. A generalized interpolation material point method for modelling coupled thermo-hydro-mechanical problems. *Comput Methods Appl Mech Eng.* 2021;386:114080. doi:10.1016/j.cma.2021.114080
54. Kularathna S, Liang W, Zhao T, Chandra B, Zhao J, Soga K. A semi-implicit material point method based on fractional-step method for saturated soil. *Int J Numer Anal Methods Geomech.* 2021;45 (10):1405-1436. doi:10.1002/nag.3207
55. Feng K, Wang G, Huang D, Jin F. Material point method for large-deformation modeling of coseismic landslide and liquefaction-induced dam failure. *Int J Soil Dyn Earthq Eng.* 2021;150:106907. doi:10.1016/j.soildyn.2021.106907
56. Zheng X, Pisanò F, Vardon PJ, Hicks MA. An explicit stabilised material point method for coupled hydromechanical problems in two-phase porous media. *Comput Geotech.* 2021;135:104112. doi:10.1016/j.compgeo.2021.104112
57. Zheng X, Pisanò F, Vardon PJ, Hicks MA. Fully implicit, stabilised MPM simulation of large-deformation problems in two-phase elastoplastic geomaterials. *Comput Geotech.* 2022;147:104771. doi:10.1016/j.compgeo.2022.104771
58. Liang W, Zhao J, Wu H, Soga K. Multiscale, multiphysics modeling of saturated granular materials in large deformation. *Comput Methods Appl Mech Eng.* 2023;405:115871. doi:10.1016/j.cma.2022.115871
59. Pinyol NM, Alvarado M, Alonso EE, Zabala F. Thermal effects in landslide mobility. *Géotechnique.* 2018;68 (6):528-545. doi:10.1680/jgeot.17.P.054
60. Yu J, Zhao J, Zhao S, Liang W. An explicit-implicit THM-coupled MPM for saturated porous media. In: *Proceeding of the 26th Annual Conference of HKSTAM 2023.* 2023:30.
61. Yu J, Zhao J, Liang W, Zhao S. A semi-implicit material point method for coupled thermo-hydro-mechanical simulation of saturated porous media in large deformation. *Comput Methods Appl Mech Eng.* 2024;418:116462. doi:10.1016/j.cma.2023.116462
62. Zhao S, Zhao J, Liang W, Niu F. Multiscale modeling of coupled thermo-mechanical behavior of granular media in large deformation and flow. *Comput Geotech.* 2022;149:104855. doi:10.1016/j.compgeo.2022.104855
63. Dumais S, Konrad JM. One-dimensional large-strain thaw consolidation using nonlinear effective stress – void ratio – hydraulic conductivity relationships. *Can Geotech J.* 2018;55 (3):414-426. doi:10.1139/cgj-2017-0221
64. Stuurrop JC, van der Zee SEATM, Voss CI, French HK. Simulating water and heat transport with freezing and cryosuction in unsaturated soil: comparing an empirical, semi-empirical and physically-based approach. *Adv Water Resour.* 2021;149:103846. doi:10.1016/j.advwatres.2021.103846
65. Zienkiewicz OC, Chang CT, Bettess P. Drained, undrained, consolidating and dynamic behaviour assumptions in soils. *Géotechnique.* 1980;30 (4):385-395. doi:10.1680/geot.1980.30.4.385
66. Huang X, Rudolph DL. Coupled model for water, vapour, heat, stress and strain fields in variably saturated freezing soils. *Adv Water Resour.* 2021;154:103945. doi:10.1016/j.advwatres.2021.103945
67. Xu X, Lai Y, Dong Y, Qi J. Laboratory investigation on strength and deformation characteristics of ice-saturated frozen sandy soil. *Cold Reg Sci Technol.* 2011;69 (1):98-104. doi:10.1016/j.coldregions.2011.07.005

68. Zhou Z, Ma W, Zhang S, Mu Y, Li G. Effect of freeze-thaw cycles in mechanical behaviors of frozen loess. *Cold Reg Sci Technol*. 2018;146:9-18. doi:10.1016/j.coldregions.2017.11.011
69. Xu X, Wang B, Fan C, Zhang W. Strength and deformation characteristics of silty clay under frozen and unfrozen states. *Cold Reg Sci Technol*. 2020;172:102982. doi:10.1016/j.coldregions.2019.102982
70. Zhu T, Chen J, Huang D, Luo Y, Li Y, Xu L. A DEM-based approach for modeling the damage of rock under freeze-thaw cycles. *Rock Mech Rock Eng*. 2021;54 (6):2843-2858. doi:10.1007/s00603-021-02465-4
71. Chang D, Yan Y, Liu J, Xu A, Feng L, Zhang M. Micro-macroscopic mechanical behavior of frozen sand based on a large-scale direct shear test. *Comput Geotech*. 2023;159:105484. doi:10.1016/j.compgeo.2023.105484
72. Sun R, Liu R, Zhang H, Liu C, Li C. DEM investigation of the mechanical behavior of frozen soil along various stress paths. *Bull Eng Geol Environ*. 2023;82 (9):351. doi:10.1007/s10064-023-03367-1
73. van Genuchten MTh. A Closed-form equation for predicting the hydraulic conductivity of unsaturated soils. *Soil Sci Soc Am J*. 1980;44 (5):892-898. doi:10.2136/sssaj1980.03615995004400050002x
74. Chapuis RP, Aubertin M. On the use of the Kozeny Carman equation to predict the hydraulic conductivity of soils. *Can Geotech J*. 2003;40 (3):616-628. doi:10.1139/t03-013
75. Kumar K, Salmond J, Kularathna S, et al. Scalable and modular material point method for large-scale simulations. arXiv:1909.13380 [physics]. 2019.
76. Ehlers W. Foundations of multiphase and porous materials. In: Ehlers W, Bluhm J, eds. *Porous Media: Theory, Experiments and Numerical Applications*. Springer; 2002:3-86
77. Sweidan AH, Heider Y, Markert B. A unified water/ice kinematics approach for phase-field thermo-hydro-mechanical modeling of frost action in porous media. *Comput Methods Appl Mech Eng*. 2020;372:113358. doi:10.1016/j.cma.2020.113358
78. Huang S, Liu Q, Cheng A, Liu Y, Liu G. A fully coupled thermo-hydro-mechanical model including the determination of coupling parameters for freezing rock. *Int J Rock Mech Min Sci*. 2018;103:205-214. doi:10.1016/j.ijrmms.2018.01.029
79. Tan X, Chen W, Tian H, Cao J. Water flow and heat transport including ice/water phase change in porous media: numerical simulation and application. *Cold Reg Sci Technol*. 2011;68 (1):74-84. doi:10.1016/j.coldregions.2011.04.004
80. Van Genuchten MT. A closed-form equation for predicting the hydraulic conductivity of unsaturated soils. *Soil Sci Soc Am J*. 1980;44 (5):892-898. doi:10.2136/sssaj1980.03615995004400050002x
81. De Vaucorbeil A, Nguyen VP, Sinaie S, Wu JY. Material point method after 25 years: theory, implementation, and applications. In: *Advances in Applied Mechanics*. Vol 53. Elsevier; 2020:185-398.
82. Coombs WM, Augarde CE, Brennan AJ, et al. On Lagrangian mechanics and the implicit material point method for large deformation elasto-plasticity. *Comput Methods Appl Mech Eng*. 2020;358:112622. doi:10.1016/j.cma.2019.112622
83. Coombs WM, Charlton TJ, Cortis M, Augarde CE. Overcoming volumetric locking in material point methods. *Comput Methods Appl Mech Eng*. 2018;333:1-21. doi:10.1016/j.cma.2018.01.010
84. Lian Y, Bui HH, Nguyen GD, Zhao S, Haque A. A Computationally efficient SPH framework for unsaturated soils and its application to predicting the entire rainfall-induced slope failure process. *Géotechnique*. 2022;1-19. doi:10.1680/jgeot.21.00349
85. Yerro A, Alonso E, Pinyol N. The material point method for unsaturated soils. *Géotechnique*. 2015;65 (3):201-217. doi:10.1680/geot.14.P.163
86. Lai Y, Xu X, Dong Y, Li S. Present situation and prospect of mechanical research on frozen soils in China. *Cold Reg Sci Technol*. 2013;87:6-18. doi:10.1016/j.coldregions.2012.12.001
87. Guermond J, Minev P, Shen J. An overview of projection methods for incompressible flows. *Comput Methods Appl Mech Eng*. 2006;195 (44-47):6011-6045. doi:10.1016/j.cma.2005.10.010
88. White JA, Borja RI. Stabilized low-order finite elements for coupled solid-deformation/fluid-diffusion and their application to fault zone transients. *Comput Methods Appl Mech Eng*. 2008;197 (49):4353-4366. doi:10.1016/j.cma.2008.05.015
89. Sun W, Ostien JT, Salinger AG. A stabilized assumed deformation gradient finite element formulation for strongly coupled poromechanical simulations at finite strain. *Int J Numer Anal Methods Geomech*. 2013;37 (16):2755-2788. doi:10.1002/nag.2161
90. Sun W. A stabilized finite element formulation for monolithic thermo-hydro-mechanical simulations at finite strain. *Int J Numer Methods Eng*. 2015;103 (11):798-839. doi:10.1002/nme.4910
91. Choo J. Stabilized mixed continuous/enriched Galerkin formulations for locally mass conservative poromechanics. *Comput Methods Appl Mech Eng*. 2019;357:112568. doi:10.1016/j.cma.2019.112568
92. Mieremet M, Stolle D, Ceccato F, Vuik C. Numerical stability for modelling of dynamic two-phase interaction. *Int J Numer Anal Methods Geomech*. 2016;40 (9):1284-1294. doi:10.1002/nag.2483
93. Markert B, Heider Y, Ehlers W. Comparison of monolithic and splitting solution schemes for dynamic porous media problems. *Int J Numer Methods Eng*. 2010;82 (11):1341-1383. doi:10.1002/nme.2789
94. Gee B, Gracie R. Comparison of fully-coupled and sequential solution methodologies for enhanced geothermal systems. *Comput Methods Appl Mech Eng*. 2021;373:113554. doi:10.1016/j.cma.2020.113554
95. Chorin A. Numerical solution of the Navier-Stokes equations. *Math Comput*. 1968;22 (104):745-762.
96. Codina R, Blasco J. A finite element formulation for the Stokes problem allowing equal velocity-pressure interpolation. *Comput Methods Appl Mech Eng*. 1997;143 (3):373-391. doi:10.1016/S0045-7825(96)01154-1
97. Guermond JL, Quartapelle L. On stability and convergence of projection methods based on pressure Poisson equation. *Int J Numer Methods Fluids*. 1998;26 (9):1039-1053. doi:10.1002/(SICI)1097-0363(19980515)26:9<1039::AID-FLD675>3.0.CO;2-U

98. Pastor M, Li T, Liu X, Zienkiewicz OC. Stabilized low-order finite elements for failure and localization problems in undrained soils and foundations. *Comput Methods Appl Mech Eng*. 1999;174 (1):219-234. doi:10.1016/S0045-7825(98)00316-8
99. Guermond JL, Quartapelle L. A projection FEM for variable density incompressible flows. *J Comput Phys*. 2000;165 (1):167-188. doi:10.1006/jcph.2000.6609
100. Mineev PD. A stabilized incremental projection scheme for the incompressible Navier–Stokes equations. *Int J Numer Methods Fluids*. 2001;36 (4):441-464. doi:10.1002/flid.139
101. Codina R. Pressure stability in fractional step finite element methods for incompressible flows. *J Comput Phys*. 2001;170 (1):112-140. doi:10.1006/jcph.2001.6725
102. Xu R, Stansby P, Laurence D. Accuracy and stability in incompressible SPH (ISPH) based on the projection method and a new approach. *J Comput Phys*. 2009;228 (18):6703-6725. doi:10.1016/j.jcp.2009.05.032
103. Huang M, Wu S, Zienkiewicz OC. Incompressible or nearly incompressible soil dynamic behaviour—a new staggered algorithm to circumvent restrictions of mixed formulation. *Int J Soil Dyn Earthq Eng*. 2001;21 (2):169-179. doi:10.1016/S0267-7261(00)00105-6
104. Li X, Han X, Pastor M. An iterative stabilized fractional step algorithm for finite element analysis in saturated soil dynamics. *Comput Methods Appl Mech Eng*. 2003;192 (35):3845-3859. doi:10.1016/S0045-7825(03)00378-5
105. Huang M, Yue ZQ, Tham LG, Zienkiewicz OC. On the stable finite element procedures for dynamic problems of saturated porous media. *Int J Numer Methods Eng*. 2004;61 (9):1421-1450. doi:10.1002/nme.1115
106. Yu J, Zhao J, Zhao S, Liang W. Multiphysics simulation of freezing and thawing granular media using material point method. *IOP Conf Ser: Earth Environ Sci*. 2024;1330 (1):012035. doi:10.1088/1755-1315/1330/1/012035
107. Codina R, Badia S. On some pressure segregation methods of fractional-step type for the finite element approximation of incompressible flow problems. *Comput Methods Appl Mech Eng*. 2006;195 (23):2900-2918. doi:10.1016/j.cma.2004.06.048
108. Badia S, Codina R. Convergence analysis of the FEM approximation of the first order projection method for incompressible flows with and without the inf-sup condition. *Numer Math*. 2007;107 (4):533-557. doi:10.1007/s00211-007-0099-5
109. Yuan WH, Zheng H, Zheng X, Wang B, Zhang W. An improved semi-implicit material point method for simulating large deformation problems in saturated geomaterials. *Comput Geotech*. 2023;161:105614. doi:10.1016/j.compgeo.2023.105614
110. Nairn JA, Guilkey JE. Axisymmetric form of the generalized interpolation material point method. *Int J Numer Methods Eng*. 2015;101 (2):127-147. doi:10.1002/nme.4792
111. Tao J, Zhang H, Zheng Y, Chen Z. Development of generalized interpolation material point method for simulating fully coupled thermomechanical failure evolution. *Comput Methods Appl Mech Eng*. 2018;332:325-342. doi:10.1016/j.cma.2017.12.014
112. Zhao S, Chen H, Zhao J. Multiscale modeling of freeze-thaw behavior in granular media. *Acta Mech Sin*. 2022;39 (1):722195. doi:10.1007/s10409-022-22195-x
113. Marrone S, Colagrossi A, Le Touzé D, Graziani G. Fast free-surface detection and level-set function definition in SPH solvers. *J Comput Phys*. 2010;229 (10):3652-3663. doi:10.1016/j.jcp.2010.01.019
114. Wang PP, Meng ZF, Zhang AM, Ming FR, Sun PN. Improved particle shifting technology and optimized free-surface detection method for free-surface flows in smoothed particle hydrodynamics. *Comput Methods Appl Mech Eng*. 2019;357:112580. doi:10.1016/j.cma.2019.112580
115. Lu K, Augarde CE, Coombs WM, Hu Z. Weak impositions of Dirichlet boundary conditions in solid mechanics: a critique of current approaches and extension to partially prescribed boundaries. *Comput Methods Appl Mech Eng*. 2019;348:632-659. doi:10.1016/j.cma.2019.01.035
116. Liang Y, Given J, Soga K. The imposition of nonconforming Neumann boundary condition in the material point method without boundary representation. *Comput Methods Appl Mech Eng*. 2023;404:115785. doi:10.1016/j.cma.2022.115785
117. Coombs WM. Ghost stabilisation of the material point method for stable quasi-static and dynamic analysis of large deformation problems. *Int J Numer Methods Eng*. 2023;124 (21):4841-4875. doi:10.1002/nme.7332
118. Yamaguchi Y, Moriguchi S, Terada K. Extended B-spline-based implicit material point method. *Int J Numer Methods Eng*. 2021;122 (7):1746-1769. doi:10.1002/nme.6598
119. Cortis M, Coombs W, Augarde C, Brown M, Brennan A, Robinson S. Imposition of essential boundary conditions in the material point method. *Int J Numer Methods Eng*. 2018;113 (1):130-152. doi:10.1002/nme.5606
120. Bing Y, Cortis M, Charlton TJ, Coombs WM, Augarde CE. B-spline based boundary conditions in the material point method. *Comput Struct*. 2019;212:257-274. doi:10.1016/j.compstruc.2018.11.003
121. Sulsky D, Zhou SJ, Schreyer HL. Application of a particle-in-cell method to solid mechanics. *Comput Phys Commun*. 1995;87 (1):236-252. doi:10.1016/0010-4655(94)00170-7
122. Bardenhagen SG, Kober EM. The generalized interpolation material point method. *Comput Model Eng Sci*. 2004;5 (6):477-496.
123. Steffen M, Kirby RM, Berzins M. Analysis and reduction of quadrature errors in the material point method (MPM). *Int J Numer Methods Eng*. 2008;76 (6):922-948. doi:10.1002/nme.2360
124. Brackbill JU. The ringing instability in particle-in-cell calculations of low-speed flow. *J Comput Phys*. 1988;75 (2):469-492. doi:10.1016/0021-9991(88)90123-4
125. Mast CM, Mackenzie-Helnwein P, Arduino P, Miller GR, Shin W. Mitigating kinematic locking in the material point method. *J Comput Phys*. 2012;231 (16):5351-5373. doi:10.1016/j.jcp.2012.04.032
126. Hammerquist CC, Nairn JA. A new method for material point method particle updates that reduces noise and enhances stability. *Comput Methods Appl Mech Eng*. 2017;318:724-738. doi:10.1016/j.cma.2017.01.035

127. Jiang C, Schroeder C, Selle A, Teran J, Stomakhin A. The affine particle-in-cell method. *ACM Trans Graph*. 2015;34(4):51:1-51:10. doi:10.1145/2766996
128. Jiang C, Schroeder C, Teran J. An angular momentum conserving affine-particle-in-cell method. *J Comput Phys*. 2017;338:137-164. doi:10.1016/j.jcp.2017.02.050
129. He KY, Liang W, Yin ZY, Jin YF. An efficient material point method framework based on the affine matrix. *Comput Geotech*. 2023;163:105712. doi:10.1016/j.compgeo.2023.105712
130. Zhao Y, Jiang C, Choo J. Circumventing volumetric locking in explicit material point methods: a simple, efficient, and general approach. *Int J Numer Methods Eng*. 2023;124 (23):5334-5355. doi:10.1002/nme.7347
131. Li W, Wei C. Stabilized low-order finite elements for strongly coupled poromechanical problems. *Int J Numer Methods Eng*. 2018;115 (5):531-548. doi:10.1002/nme.5815
132. Yao X, Qi J, Wu W. Three dimensional analysis of large strain thaw consolidation in permafrost. *Acta Geotech*. 2012;7 (3):193-202. doi:10.1007/s11440-012-0162-y
133. Harris C, Kern-Luetsch M, Murton J, Font M, Davies M, Smith F. Solifluction processes on permafrost and non-permafrost slopes: results of a large-scale laboratory simulation. *Permafrost Periglacial Process*. 2008;19 (4):359-378. doi:10.1002/ppp.630
134. Harris C, Smith JS, Davies MCR, Rea B. An investigation of periglacial slope stability in relation to soil properties based on physical modelling in the geotechnical centrifuge. *Geomorphology*. 2008;93 (3):437-459. doi:10.1016/j.geomorph.2007.03.009
135. Setiasabda EY. *Material Point Method for Large Deformation Modeling in Geomechanics Using Isoparametric Elements*. PhD thesis. UC Berkeley; 2020.
136. Armstrong L, Lacelle D, Fraser RH, Kokelj S, Knudby A. Thaw slump activity measured using stationary cameras in time-lapse and structure-from-motion photogrammetry. *Antarct Sci*. 2018;4 (4):827-845. doi:10.1139/as-2018-0016
137. Kakouris EG, Triantafyllou SP. Phase-field material point method for brittle fracture. *Int J Numer Methods Eng*. 2017;112 (12):1750-1776. doi:10.1002/nme.5580
138. Kakouris EG, Triantafyllou SP. Phase-field material point method for dynamic brittle fracture with isotropic and anisotropic surface energy. *Comput Methods Appl Mech Eng*. 2019;357:112503. doi:10.1016/j.cma.2019.06.014
139. Hu Z, Zhang H, Zheng Y, Ye H. Phase-field implicit material point method with the convected particle domain interpolation for brittle-ductile failure transition in geomaterials involving finite deformation. *Comput Methods Appl Mech Eng*. 2022;390:114420. doi:10.1016/j.cma.2021.114420
140. Yang C, Zhu F, Zhao J. Coupled total- and semi-Lagrangian peridynamics for modelling fluid-driven fracturing in solids. *Comput Methods Appl Mech Eng*. 2024;419:116580. doi:10.1016/j.cma.2023.116580
141. Yu J, Zhao J, Liang W, Zhao S. Multiscale modeling of coupled thermo-hydro-mechanical behavior in ice-bonded granular media subject to freeze-thaw cycles. *Comput Geotech*. 2024;171:106349. doi:10.1016/j.compgeo.2024.106349
142. Wu H, Wu W, Liang W, Dai F, Liu H, Xiao Y. 3D DEM modeling of biocemented sand with fines as cementing agents. *Int J Numer Anal Methods Geomech*. 2023;47 (2):212-240. doi:10.1002/nag.3466

How to cite this article: Yu J, Zhao J, Zhao S, Liang W. Thermo-hydro-mechanical coupled material point method for modeling freezing and thawing of porous media. *Int J Numer Anal Methods Geomech*. 2024;48:3308–3349. <https://doi.org/10.1002/nag.3794>

APPENDIX A: MATRICES IN DISCRETIZED EQUATIONS

$$\mathcal{M}_{11} = \int_{\Omega} \mathbf{s}^T (n_s \rho_s + n_c \rho_c) \mathbf{s} dV, \quad (\text{A1})$$

$$\mathcal{M}_{12} = \mathcal{M}_{22} = \int_{\Omega} \mathbf{s}^T n_l \rho_l \mathbf{s} dV, \quad (\text{A2})$$

$$\mathcal{M}_{33} = \int_{\Omega} \mathbf{s}^T \frac{n_l}{K_l} \mathbf{s} dV, \quad (\text{A3})$$

$$\mathcal{M}_{34} = \int_{\Omega} \mathbf{s}^T \left(\zeta \phi \frac{\partial S_l}{\partial T} - \beta_m \right) \mathbf{s} dV, \quad (\text{A4})$$

$$\mathcal{M}_{44} = \int_{\Omega} \mathbf{s}^T \left(C_m + \rho_c L_f \phi \frac{\partial S_l}{\partial T} \right) \mathbf{s} dV, \quad (\text{A5})$$

$$\mathcal{K}_{13} = \int_{\Omega} \mathbf{S}^T \xi_s (n_s + n_c) \nabla \mathbf{S} dV, \quad (\text{A6})$$

$$\mathcal{K}_{22} = -\mathcal{K}_{21} = \int_{\Omega} \mathbf{S}^T n_l^2 \frac{\rho_l g}{k_a k_r} \mathbf{S} dV, \quad (\text{A7})$$

$$\mathcal{K}_{23} = \int_{\Omega} \mathbf{S}^T \xi_l n_l \nabla \mathbf{S} dV, \quad (\text{A8})$$

$$\mathcal{K}_{31} = \int_{\Omega} \mathbf{S}^T (1 - \zeta n_c) \nabla \mathbf{S} d\Omega + \int_{\Omega} \nabla \mathbf{S}^T n_l \mathbf{S} dV, \quad (\text{A9})$$

$$\mathcal{K}_{32} = - \int_{\Omega} \nabla \mathbf{S}^T n_l \mathbf{S} dV, \quad (\text{A10})$$

$$\mathcal{K}_{33} = \int_{\Omega} \nabla \mathbf{S}^T \Delta t \left(\xi_l \frac{n_l}{\rho_l} + \xi_s (n_s + n_c - \zeta n_c) \frac{n_s + n_c}{n_s \rho_s + n_c \rho_c} \right) \nabla \mathbf{S} dV, \quad (\text{A11})$$

$$\mathbf{f}_1 = \int_{\partial\Omega} \mathbf{S}^T \hat{\mathbf{t}} dS - \int_{\Omega} \nabla \mathbf{S}^T : \boldsymbol{\sigma}^k dV + \int_{\Omega} \mathbf{S}^T \rho_m \mathbf{b} dS, \quad (\text{A12})$$

$$\mathbf{f}_2 = \int_{\partial\Omega} \mathbf{S}^T \hat{\mathbf{t}}_l dS - \int_{\Omega} \nabla \mathbf{S}^T : (-n_l p_l^k \mathbf{I}) dV + \int_{\Omega} \mathbf{S}^T n_l \rho_l \mathbf{b} dV, \quad (\text{A13})$$

$$\mathbf{f}_3 = - \int_{\partial\Omega} \mathbf{S}^T \hat{\mathbf{q}}_l^{k+1} dS \quad (\text{A14})$$

$$\mathbf{f}_4 = - \int_{\Omega} \mathbf{S}^T n_l \rho_l c_l (\mathbf{v}_l^k - \mathbf{v}_s^k) \nabla T dV + \int_{\partial\Omega} \mathbf{S}^T \hat{\mathbf{q}}_T dS - \int_{\Omega} \nabla \mathbf{S}^T \kappa_m \nabla T dV + \int_{\Omega} \mathbf{S}^T Q dS, \quad (\text{A15})$$

APPENDIX B: SUPPLEMENTAL MATERIALS FOR EXAMPLE 1

B.1 | SFCC and relative permeability model

The example employs an exponential-shaped soil freezing characteristic curve

$$S_l = S_l^{res} + (1 - S_l^{res}) \exp \left[- \left(\frac{T - T_0}{M} \right)^2 \right] \quad (\text{B1})$$

where S_l^{res} is the residual saturation, T_0 is the freezing point, M is a material constant, and k_0 is the intrinsic permeability. The following saturation-dependent relative hydraulic conductivity is adopted:

$$k_r = \max \left\{ 10^{-\phi \lambda (1 - S_l)}, 10^{-6} \right\} \quad (\text{B2})$$

TABLE B1 Tests for convergence study.

Test ID	Cell size	Total cells	Particle size	Total particles
0.04m-9ppc	0.04 m	1875	0.0133 m	16,875
0.04m-16ppc			0.01 m	30,000
0.04m-25ppc			0.008 m	46,875
0.02m-4ppc	0.02 m	7500	0.01 m	30,000
0.02m-9ppc			0.0667 m	67,500
0.02m-16ppc			0.005 m	120,000
0.02m-25ppc			0.004 m	187,500
0.01m-4ppc	0.01 m	30,000	0.005 m	120,000
0.01m-9ppc			0.00333 m	270,000

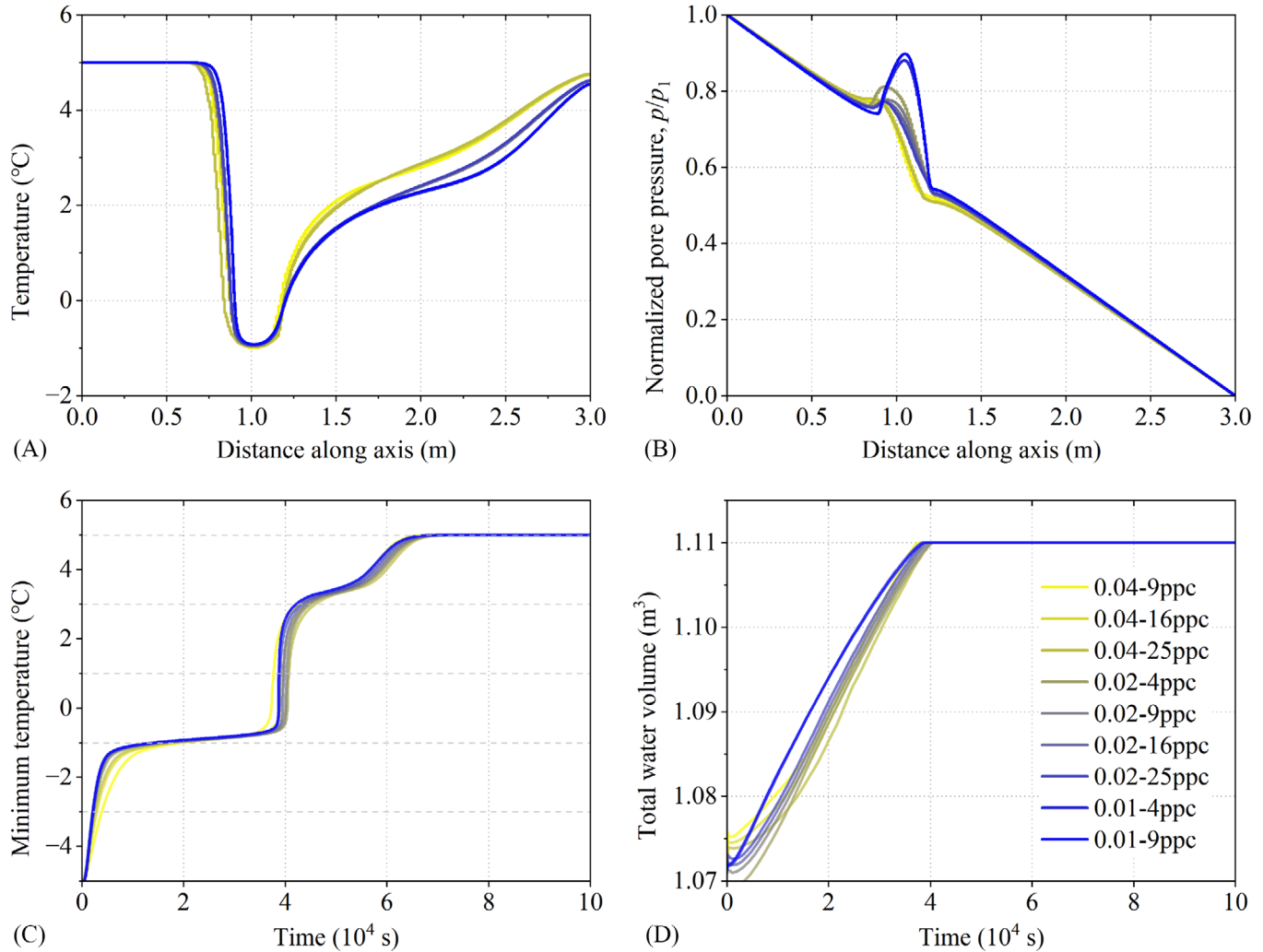


FIGURE B1 Convergence test to show the influence of mesh size and particle density on the simulation results.

where ϕ is the porosity and λ is a shape parameter. In this example, the model parameters are taken as follows: $S_l^{res} = 0.05$, $T_0 = 0^\circ\text{C}$, $M = 0.5^\circ\text{C}$, and $\lambda = 50$. The freezing curve varies over a range of approximately 1°C between the start of freezing at 0°C and the end at about -1°C (leaving a residual saturation of liquid water).

B.2 | Convergence test

The spatial sensitivity analyses are first conducted to check the convergence of the numerical scheme and show how the discretization parameters, for example, the mesh size and the particle density (characterized by the number particle per cell, ppc), influence the numerical results. Uniform quadrilateral cell is used, with cell size varying from 0.1 to 0.5 m, and the number of PPC varying from 1 to 25. All test cases are listed in Table B1. Figure B1 shows simulation results in Case 3.

APPENDIX C: STABILIZATION ISSUE

Figure C1 compares the stabilization preformation with different stabilization parameters in the rock freezing case. As can be seen, if there is no stabilization term ($\tau = 0$) or the stabilization parameter is not large enough ($\tau = 0.1$), the pressure may encounter checkerboard pressure oscillation near the boundary. While given a proper value of stabilization parameter (e.g., $\tau = 0.5$ and $\tau = 1.0$), the result can be well smoothed. More details on the choice of the stabilization parameter can be found in Ref. 52.

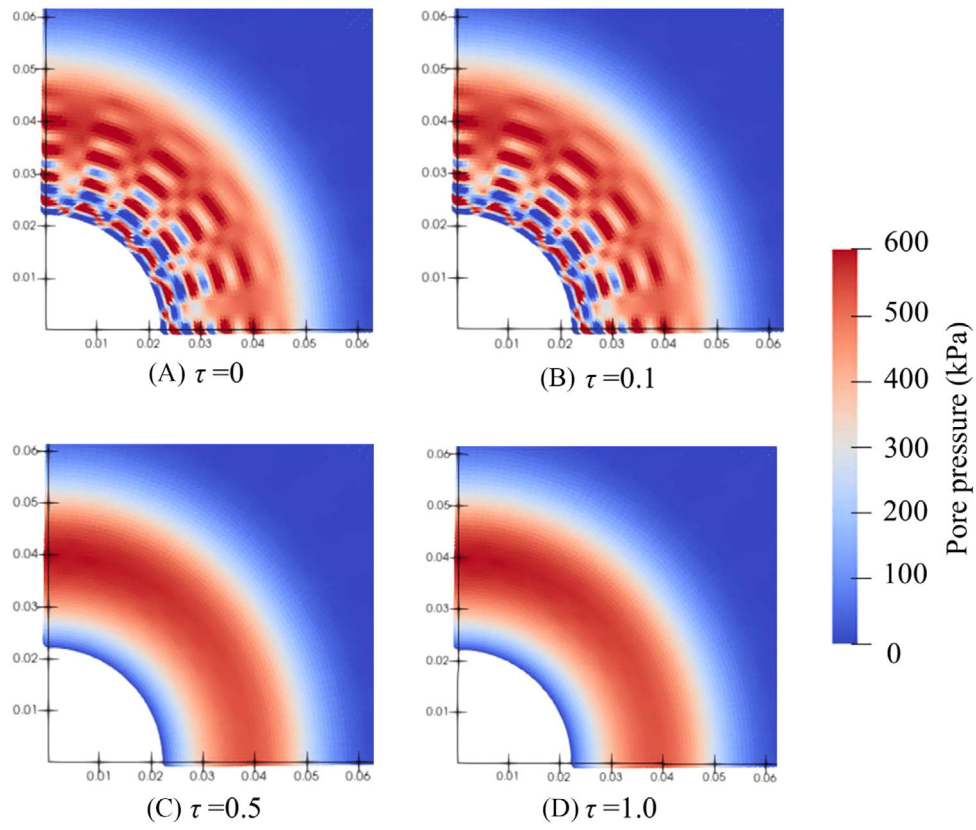


FIGURE C1 Stabilization effect with different stabilization parameter τ in the rock freezing case.